KAUNAS UNIVERSITY OF TECHNOLOGY

ALGIRDAS LAZAUSKAS

SURFACE MORPHOLOGY, COHESIVE AND ADHESIVE PROPERTIES OF PHYSICAL VAPOR DEPOSITED CHROMIUM AND CHROMIUM COMPOSITE THIN FILMS

Doctoral dissertation
Technological Sciences, Materials Engineering (08T)

2014, Kaunas

Doctoral dissertation was prepared during 2010 – 2014 year period at Kaunas University of Technology, Institute of Materials Science and supported by State Studies Foundation, Research Council of Lithuania and Agency for Science, Innovation and Technology.

Scientific supervisor

Dr. Viktoras Grigaliūnas (Kaunas University of Technology, Technological Sciences, Materials Engineering – 08T)

KAUNO TECHNOLOGIJOS UNIVERSITETAS

ALGIRDAS LAZAUSKAS

FIZIKINIAIS METODAIS NUSODINTŲ PLONŲ CHROMO IR CHROMO KOMPOZICINIŲ PLĖVELIŲ PAVIRŠIAUS MORFOLOGIJA, KOHEZINĖS IR ADHEZINĖS SAVYBĖS

Daktaro disertacija
Technologijos mokslai, Medžiagų inžinerija (08T)

2014, Kaunas

Disertacija rengta 2010 – 2014 metais Kauno technologijos universitete, Medžiagų mokslo institute, remiant Valstybiniam studijų fondui, Lietuvos mokslo tarybai ir Mokslo, inovacijų ir technologijų agentūrai.

Mokslinis vadovas

Dr. Viktoras Grigaliūnas (Kauno technologijos universitetas, technologijos mokslai, medžiagų inžinerija – 08T)

Dedicated to

my Family

Reziume

Disertacijoje nagrinėjama plonų chromo ir chromo kompozicinių plėvelių paviršiaus morfologija, kohezinės ir adhezinės savybės, koncentruojantis į struktūros-savybių sąryšį. Plonos chromo plėvelės buvo nusodinamos, naudojant terminio garinimo ir magnetroninio dulkinimo metodus. Chromo kompozicinės plėvelės buvo formuojamos, kombinuojant terminį garinimą ir apdorojimą deguonies jonų plazmoje. Kitos kompozicinės plėvelės buvo formuojamos, kombinuojant deimanto tipo anglies ir deimanto tipo anglies-polimero plėveles su chromo plėvele padengtu stiklo pagrindu. Amorfinės hidrogenizuotos anglies (a-C:H), SiO_x turinčios a-C:H (a-C:H/SiO_x) ir azotu legiruotos a-C:H/SiO_x (a-C:H:N/SiO_x) plonos plėvelės buvo nusodinamos ant chromo plėvele padengtų (ar polivinilpirolidono-chromo plėvele) stiklo pagrindų. Plėvelių nusodinimui naudotas šalto katodo jonų šaltinis ir skirtingos nešančiųjų dujų ir pirmtako kombinacijos. Atlikta sisteminė studija, kurioje buvo ištirtas silikatinio plukdytojo stiklo pagrindo paviršiaus paruošimo metodų efektyvumas plonos chromo plėvelės su pagrindu adhezijai pagerinti. Brėžimo testais ir vilgymo kampo matavimais nustatyti efektyviausi paviršiaus paruošimo metodai, kurie pagerino plonos chromo plėvelės su pagrindu adheziją. Atominių jėgų mikroskopu nustatyta, kad termiškai garintos plonos chromo plėvelės paviršius susideda iš nanometrinių struktūrų. Šios struktūros linkę jungtis į mikrometrinio pločio saleles, kai chromo plėvelė yra formuojama magnetroninio dulkinimo metodu. Plėvelių nanostruktūrinių skirtumų atsiradimas siejamas su skirtingu chromo kondensacijos mechanizmu. Sukurtos dviem žingsniais termiškai garintos plonos chomo plėvelės, kurios pasižymėjo geresnėmis kohezinėmis savybėmis ir adhezija su stiklo pagrindu. Taip pat šios plėvelės pasižymėjo geresnėmis optinėmis savybėmis (atspindžiu), nei įprastinės chromo plėvelės. Rentgeno struktūrinė analizė parodė, kad dviem žingsniais termiškai garintos plonos chromo plėvelės yra polikristalinės, difraktogramoje registruota pati intensyviausia smailė - (110). Kambario temperatūroje šių plėvelių dilimo greitis buvo sąlyginai mažas. Tik pusė chromo plonos plėvelės buvo nudilinta po ~18 m sauso slydimo (kambario temperatūroje). Dviem žingsniais termiškai garintos plonos chromo plėvelės yra tinkamos litografinių kaukių, precizinių optinių liniuočių ir limbų gamybai. a-C:H/SiO_x ir a-C:H:N/SiO_x plėvelės pasižymėjo geresnėmis mechaninėmis savybėmis, lyginant su a-C:H plėvelėmis. Furjė transformacijos infraraudonųjų spindulių spektrometru nustatyta, kad polivinilpirolidono paviršiaus sąveika su tiesioginiu jonų pluošteliu sąlygoja pokyčius polimero karbonilų grupėje, kurie priklauso nuo nešančiųjų dujų ir pirmtako, naudojamų deimanto tipo anglies plėvelių nusodinimui.

Acknowledgements

It is a pleasure to thank those who made this dissertation possible. I owe my deepest gratitude to my supervisor dr. Viktoras Grigaliūnas. I have always benefited from his expertise supervision, brilliant ideas, continuous enthusiasm, rigorous attitude to science, valuable advices and extensive knowledge.

I am also most grateful to dr. Jonas Baltrušaitis from University of Twente for scientific insight and valuable detailed comments and suggestions which have greatly helped to improve my scientific writing and interpretation of results.

I am grateful to all staff of Institute of Materials Science for their kind help. I sincerely thank prof. dr. Sigitas Tamulevičius for believing in me and for his valuable critics which made me much confident and improved my scientific skills. I especially would like to thank dr. Asta Guobienė who patiently taught me how to use atomic force microscope, and dr. Igoris Prosyčevas for many valuable technical discussions and brainstorming sessions. I am grateful to dr. Mindaugas Andrulevičius for the first insight into X-ray photoelectron spectroscopy. I thank dr. Dalius Jucius and dr. Rimantas Gudaitis for the first look at this work, their comments and suggestions.

I wish also to thank Fanny Ecarla from CSM Instruments SA for scratch testing, and dr. Tomas Polcar from Czech Technical University for tribological testing of my samples.

I sincerely thank the official reviewers of the dissertation, prof. dr. Juozas Vidas Gražulevičius and prof. dr. Arvaidas Galdikas, for their time, careful work and valuable comments on the work.

I devote my deepest gratitude to my family for their unlimited love and support. They have encouraged me throughout the years of this dissertation.

CONTENTS

LIST OF FIGURES

Fig. 41. Normalized height distribution histograms and bearing ratio curves: (a) one-step thermally deposited chromium film surface and (b) two-step thermally deposited chromium surface. Dashed line indicates the height at which surface structures are connected to each other. The middle line indicates the mean height.
Fig. 42. Scratch test data for (a) one-step and (b) two-step (b) thermal deposited chromium thin films. Friction coefficient (1), normal force (2), penetration depth (3) and residual depth (4) characteristic resulting curves as a function of the scratch length are shown. First vertical axis (from right to left) corresponds to the friction coefficient and the second axis to normal force. Vertical lines indicate the critical loads. Arrows indicate the penetration depth and residual depth at the critical loads.
Fig. 43. Optical micrographs and 3D surface plots of critical failure points along a progressive load scratch performed on two-step (a) and (b), and one-step (c) and (d) thermally deposited chromium thin films. The first failure, L_{c1} (a) and (c), corresponds to initial cracking (indicated by ellipse markers), the second failure, L_{c2} (b) and (d) to the full delamination of the chromium film. Scratch direction is from left to right. The same fracture can be observed on the other samples.
Fig. 44. Summary of critical loads results of one-step and two-step thermal deposited chromium films. L_{c1} corresponds to the first failure where the initial cracking is present and L_{c2} the second failure of the full delamination of thin films.
Fig. 45. X-ray diffraction pattern of the two-step thermally deposited chromium film.
Fig. 46. High resolution Cr 2p and O 1s region XPS spectra of as-deposited chromium films and after the first etching cycle.
Fig. 47. Typical friction trace obtained with (a) 100Cr6 (b) and 440C bearing steel balls at room temperature on two-step thermally deposited chromium films. The detachment of Cr_xO_y takes place (1) at the top of Cr_xO_y surface, (2) within the thin Cr_xO_y layer, (3) at the Cr_xO_y/Cr interface and (4) in the Cr film during running-in period.
Fig. 48. Characteristic wear track section topographical images with normalized Z, nm scale for sliding against (a) 100Cr6 and (b) 400C bearing steel balls at room temperature with corresponding normalized height distribution histograms and bearing ratio curves at (a1) and (b1), respectively. Dashed line indicates the height at which surface structures are connected to each other. The middle line indicates the mean height.
Fig. 49. SEM micrographs (scale bar of 100μm) of the wear track sections for sliding against (a) 100Cr6 and (b) 400C bearing steel balls at room temperature with EDS point analysis performed at (1), (2) and (3), corresponding to the trace of elemental composition shown (bottom).
Fig. 50. Typical friction trace obtained with the 440C bearing steel balls at (a) 100 and (b) 200 ºC on two-step thermally deposited chromium films.
Fig. 51. Characteristic wear track section topographical images (middle) with normalized Z, nm scale for sliding against 400C bearing steel balls at (a) 100 and (b) 200 ºC with the corresponding normalized height distribution histograms and bearing ratio curves at (left), respectively. Dashed line indicates the height at which surface structures are connected to each other. The middle line indicates the mean height. Magnified 1st and 2nd level characteristic regions are shown at (right).

Fig. 52. SEM micrographs (scale bar of 100μm) of the wear track sections for sliding against 400C bearing steel balls at (a) 100 and (b) 200 ºC with the EDS point analysis performed at (1), (2) (3) and (4), corresponding to the trace elemental composition shown at a_3 and b_3, respectively. EDS mapping of (Cr–Kα) shown at (a_1) and (b_1), (O–Kα) (a_2) and (b_2).

Fig. 53. Characteristic reflection spectrum of one-step and two-step thermal deposited chromium thin films.

Fig. 54. (top) Characteristic 4 μm × 4 μm AFM 3D topographical images with normalized z axis in nm as well as (bottom) normalized height distribution histograms and bearing ratio curves of (a) a-C:H:N/SiO_x film surface, (b) a-C:H film surface and (c) a-C:H/SiO_x film surface. Dashed horizontal line in height distribution histogram indicates the height at which surface structures are connected to each other. The solid horizontal line indicates the mean height.

Fig. 55. Scratch test data for (a) a-C:H:N/SiO_x, (b) a-C:H and (c) a-C:H/SiO_x films. Friction coefficient (1), frictional force (2), normal force (3), penetration depth (4) and residual depth (5) characteristic resulting curves as a function of the scratch length are shown. First vertical axis (from right to left) corresponds to the friction coefficient and the second axis to frictional force and normal force. Arrows indicate the penetration depth and residual depth at the critical loads. Dotted horizontal lines indicate values of critical loads.

Fig. 56. (top) Optical micrographs of the scratched (a) a-C:H:N/SiO_x, (b) a-C:H and (c) a-C:H/SiO_x films. (bottom) Zoom in into the full delamination area of the film for each sample. Scratch direction is from left to right.

Fig. 57. Plotted summary of the critical load results of (a) a-C:H:N/SiO_x, (b) a-C:H and (c) a-C:H/SiO_x films. L_{c1} corresponds to the first failure where the initial cracking was present and L_{c2} - to the second failure at the point of the full delamination of thin films.

Fig. 58. Characteristic 12 μm × 12 μm AFM 3D topographical images with a normalized z scale in nm of critical loading sections along the progressive load scratch performed on of (a) a-C:H:N/SiO_x, (b) a-C:H and (c) a-C:H/SiO_x films. Length profile images of scratch track nanostructure along the diagonal lines in AFM topographical images are also shown. The first failure Lc1 corresponds to the initial cracking (indicated by ellipsoid markers on the topography image) while the second failure L_{c2} corresponds to the full delamination of the film (also indicated by ellipse markers). Scratch direction is indicated by a black arrow.

Fig. 59. High resolution C1s XPS spectra of (a) a-C:H:N/SiO_x, (b) a-C:H and (c) a-C:H/SiO_x films. Dashed lines are actual data and solid lines are Gaussian/Lorentzian product with 30% Lorentzian and 70% Gaussian character.

Fig. 60. Reflectance spectra of undoped DLC-PVP (a) and nitrogen-doped DLC-PVP (b) composite films. Number marks (1), (2) and (3) indicate the PVP5%, PVP10% and PVP20%, respectively.

Fig. 61. AFM characteristic topographical images (12 μm × 12 μm scan size) with normalized Z, nm scale of PVP5% (a), PVP10% (b) and PVP20% (c) films and a-C:H/SiO_x/PVP5% (d), a-C:H/SiO_x/PVP10% (e), a-C:H/SiO_x/PVP20% (f), a-

C:H:N/SiO_x/PVP5% (g), a-C:H:N/SiO_x/PVP10% (h) and a-C:H:N/SiO_x/PVP20% (i) composite films.

Fig. 62. Normalized height distribution histograms and bearing ratio curves of a-C:H/SiO_x/PVP5% (a), a-C:H/SiO_x/PVP10% (b), a-C:H/SiO_x/PVP20% (c), a-C:H:N/SiO_x/PVP5% (d), a-C:H:N/SiO_x/PVP10% (e) and a-C:H:N/SiO_x/PVP20% (f) composite films.

Fig. 63. Adhesion mapping images constructed by displaying the adhesion force values in spectrum look up table scheme on 12 μm × 12 μm scan size AFM topographical images with Fad, nN scale of a-C:H/SiO_x/PVP5% (a), a-C:H/SiO_x/PVP10% (b), a-C:H/SiO_x/PVP20% (c), a-C:H:N/SiO_x/PVP5% (d), a-C:H:N/SiO_x/PVP10% (e) and a-C:H:N/SiO_x/PVP20% (f) composite films. The circle marks separated by mesh indicate the points where AFM force-distance curve measurements were performed.

Fig. 64. FTIR spectra of a-C:H/SiO_x/PVP20% (a) and a-C:H:N/SiO_x/PVP20% (b) composite films. Assigned peaks (1) at 1672.6 cm-1 and (2) at 1644.0 cm^{-1} for (a); and (1) at 1674.1 cm^{-1} for (b).Fig. 64. Panoramic FTIR spectra of PVP5% (a), PVP10% (b) and PVP20% (c) films and a-C:H/SiO_x/PVP5% (d), a-C:H/SiO_x/PVP10% (e), a-C:H/SiO_x/PVP20% (f), a-C:H:N/SiO_x/PVP5% (g), a-C:H:N/SiO_x/PVP10% (h) and a-C:H:N/SiO_x/PVP20% (i) composite films.

Fig. 65. Panoramic FTIR spectra of PVP5% (a), PVP10% (b) and PVP20% (c) films and a-C:H/SiO_x/PVP5% (d), a-C:H/SiO_x/PVP10% (e), a-C:H/SiO_x/PVP20% (f), a-C:H:N/SiO_x/PVP5% (g), a-C:H:N/SiO_x/PVP10% (h) and a-C:H:N/SiO_x/PVP20% (i) composite films.

Fig. 66. The prototype incremental optical scale fabricated from the two-step thermally deposited chromium thin film on glass substrate.

LIST OF TABLES

LIST OF ABBREVIATIONS

100Cr6	- steel grade
440C	- steel grade
AFM	- atomic force microscopy
a-C:H	- amorphous hydrogenated carbon
a-C:H/SiO$_x$	- SiO_x containing amorphous hydrogenated carbon
a-C:H:N/SiO$_x$	- nitrogen doped SiO_x containing amorphous hydrogenated carbon
a-C:H:F	- fluorine doped amorphous hydrogenated carbon
a-C:H:Cl	- chlorine doped amorphous hydrogenated carbon
d	- the spacing between diffracting planes (in X-ray diffractometry) or film thickness
DLC	- diamond-like carbon
DC	- direct current
DIB	- direct ion beam
DI	- deionized water
e-beam	- electron beam
EDS	- energy dispersive X-ray spectroscopy
FTIR	- Fourier transform infrared spectroscopy
HMDSO	- hexamethyldisiloxane
hv	- energy of X-ray beam
I	- intensity of light passing through the sample or intensity of light reflected from the sample
I_0	- intensity of light before it passes through the sample or intensity of light reflected from the material
IB	- ion beam
IR	- infrared
l	- liquid
L_{c1}	- critical load at which first crack or failure appears
L_{c2}	- critical load at which full delamination of the film occurs
n	- integer number
P	- power
PVD	- physical vapor deposition
PDMS	- polydimethylsiloxane
PVP	- polyvinylpyrrolidone
PTFE	- polytetrafuoroethylene
PECVD	- plasma enhanced chemical vapor deposition
p	- component oscillating parallel to the sample surface
R	- reflectance
R_q	- root mean square roughness, the average of the measured height deviations taken within the evaluation area and measured from the mean linear surface
R_{sk}	- skewness, negative skewness indicates predominance of valley while a positive value indicates a surface dominated by peaks

R_{ku}	- kurtosis, measure of the height randomness and sharpness of a surface
R_{pk}	- reduced peak height
R_k	- core-roughness
R_{vk}	- reduced valley depth
RCA-1	- wet chemical cleaning method with a base-peroxide mixture
RCA-2	- wet chemical cleaning method with a acid-peroxide mixture
RIBE	- reactive ion beam etching
RF	- radio frequency
s	- component oscillating perpendicular to the plane of incidence and parallel to the sample surface or solid
SEM	- scanning electron microscopy
sp^2	- three of four valence electrons of carbon assigned to a trigonally directed sp^2 hybrid orbital
sp^3	- four valence electrons of carbon assigned to a tetrahedrally directed sp^3 hybrid orbital
s	- solid
T	- transmittance
T	- temperature
T_M	- melting point of the material
T/T_M	- renormalized film temperature
ta-C:H	- hydrogenated tetrahedral amorphous carbon
XRD	- X-ray diffractometry
XPS	- X-ray photoelectron spectrometry
θ	- the angle between the incident atomic flux and the substrate surface normal (in deposition process); angle measured through the liquid, where a liquid/gas interface meets a solid surface (in contact angle measurements); angle of incidence
γ	- excess free energy per unit area;
λ	- wavelength
η	- refractive index of the film material

ABSTRACT

This dissertation explores a surface morphology, cohesive and adhesive properties of chromium and chromium composite films with a focus on structure-property relationship. Chromium (Cr) thin films were prepared on glass substrates via thermal evaporation and magnetron sputtering techniques. Chromium composite films were prepared via combination of thermal evaporation and O_2 plasma treatment. Other composite films were prepared by combining diamond-like carbon (DLC) and DLC-polymer films on chromium thin film coated glass. Specifically, amorphous hydrogenated carbon (a-C:H), SiO_x containing a-C:H (a-C:H/SiO_x) and nitrogen doped a-C:H/SiO_x (a-C:H:N/SiO_x) thin films were deposited on Cr/glass and polyvinylpyrrolidone (PVP)/Cr/glass samples using a closed drift ion beam source from different precursor/gas. The systematic investigation of the influence of soda-lime-silica float glass substrate surface preparation on the adhesion strength of chromium thin film to substrate was performed. Suitable substrate surface preparation methods which improved the adhesion were identified via contact angle measurements and scratch testing. As determined from atomic force microscopy, chromium thin films prepared using thermal evaporation technique consisted of isolated surface mounds while in magnetron sputtered samples, these mounds combined to form larger islands. Nanostructural differences between chromium thin films deposited using thermal evaporation and magnetron sputtering techniques were attributed to the different chromium film condensation and growth mechanisms resulting in structural and chemical changes as confirmed by X-ray diffractometry (XRD) and X-ray photoelectron spectrometry (XPS). Two-step thermally deposited chromium films were developed. They exhibited favorable surface morphology against scratch tests performed using the progressive loading. The two-step thermal deposition of chromium thin films followed by O_2 plasma treatment after the first deposition resulted in better mechanical strengths as compared with conventional deposition process. Importantly, the required optical characteristics of these films to be applicable as the main component for production of lithographic masks, scale gratings or reticles were not negatively affected. The X-ray diffraction pattern of the two-step thermally deposited chromium film showed the presence of well-defined body-centered cubic Cr metal structure with a (110) plane observable. Two-step thermally deposited chromium films exhibited low wear rates at room temperature. Only the first half of the metallic chromium film was worn out after ~18 m of dry sliding at room temperature. The a-C:H/SiO_x and a-C:H:N/SiO_x thin films showed better mechanical strength as compared to the conventional a-C:H films. The XPS was used to determine the chemical composition of these films. It showed increased amounts of silicon and absence of terminal oxygenated carbon bonds in a-C:H:N/SiO_x which was attributed to its improved mechanical properties. DLC-polymer films exhibited different morphologies with characteristic surface textures. It was determined that interfacial interactions of PVP with the direct ion beam induced changes in the carbonyl group of the PVP and were dependent on the carrier gas used for the synthesis of the DLC films.

INTRODUCTION

Physical vapor deposition (PVD) techniques, routinely used for thin film deposition on different substrates to enhance certain functionality features are currently very pervasive in various applications, both in research and industry. Deposition of thin chromium films on various substrates attracted considerable attention due to chromium being prone towards high melting point carbide formation, as well as to its specific magnetic, mechanical and optical properties. Chromium thin film left standing in air is passivated by oxygen and forms a thin oxide surface layer which provides high corrosion resistance. Chromium oxide layers, in particular, chromium alpha phase (i.e. Cr_2O_3) are also highly valued for high hardness, chemical inertness, mechanical strength and stability. Specifically, chromium thin film on glass substrate is the backbone of lithographic mask production as well as in the manufacturing of precision scale gratings and reticles. The lithographic masks, precision scale gratings and reticles, which are widely used in metrology instruments, motion systems and high precision machining tools ranging from digital calipers to coordinate measuring machines, typically consist of the patterned chromium film on the top of the glass substrate. In proportion to the development of such systems and devices, as a rule, high quality is requested altering the requirements for chromium thin films. Specifically, lithographic masks, scale gratings and reticles require smooth chromium film surface. Rough surface can induce diffuse reflectance which leads to throughput loss, reduced image contrast and interference effects. Reduction of surface roughness can be achieved by proper selection of PVD technique and control of deposition parameters. Typically, chromium thin films are deposited via thermal evaporation, magnetron sputtering or cathodic arc evaporation techniques. Another key requirement of lithographic masks, scale gratings and reticles is scratch/wear resistance related to the long-term usage of such systems and devices. For instance, in the case of the scale gratings and reticles, which are used in optical encoders, even the smallest scratch can modify the optoelectronic signals of the device. As a result, errors in the position estimation can occur and could lead to catastrophic failure (e.g. in car manufacturing facilities, where robotic arms perform the assembly). Scratch/wear resistance is a contact-related property which is in conjunction with film to substrate adhesive bonding strength, cohesive properties and surface morphology of the film. A clean, dry substrate is a necessary prerequisite for adhesive bonding. Rarely can a structural adhesive penetrate through surface contaminants to provide an optimum bond on an unclean surface. There exist a numerous approaches to prepare high-quality glass surface - free of contaminants. However, there is no consensus on effectiveness on surface preparation methods as glass composition varies depending on the product and in turn the surface preparation method effectiveness can differ. Therefore, each time a systematic study is required to check the effectiveness of surface preparation methods for particular type of glass. Further, wear resistance can be improved by applying a protective film. In case of lithographic masks, grating scales and reticles, the solution for improvement of wear resistance of chromium thin films via application of protective coating is highly sophisticated. The protective film should

not negatively affect the optical characteristics of glass and chromium. It should exhibit higher wear resistance, lower roughness and better adhesion to chromium film as well as to glass. Up to now, there are no commercial lithographic masks, grating scales or reticles with protective film applied on chromium/glass system. A possible candidate could be diamond-like carbon films. These films are known to possess high hardness, low wear resistance and friction coefficient, and controllable refractive index. Specifically, diamond-like carbon is a metastable form of amorphous carbon having a high fraction of carbon atoms which are bonded by sp^3 type bonds (i.e. like in diamond). Generally, they consist of the carbon atoms which are bonded by sp^2 type bonds (i.e. like in graphite) embedded into the sp^3 bonded carbon matrix. The mechanical and optical properties of DLC films depend on the amount of sp^2 and sp^3 bonds as well as hydrogen content. These properties are in turn related to selection of deposition method, deposition parameters, and precursor/gas used for synthesis of DLC. Furthermore, properties of DLC films can be tuned via doping with additional elements (e.g. N, Si, SiO_x etc.). The DLC films can be prepared via filtered cathodic arc, plasma enhanced chemical vapor deposition and direct ion beam techniques. A first step towards accomplishment of this approach is to explore surface morphology, cohesive and adhesive properties of different DLC films deposited on top of chromium thin film. A more complex but logic and feasible approach would be to use an additional polymeric interlayer between the DLC and chromium/glass composite system, which would compensate the mismatch in thermal expansion coefficient of chromium/glass composite system. It would provide protection against uneven distribution of stress in DLC film and unwanted early delamination. DLC-polymer films are relatively new field compared to DLC or chromium thin films. However, they are rapidly gaining scientific interest as several novel applications for the DLC-polymer composites were proposed and commercialized. Preferably, water soluble polymeric interlayer could be used between DLC and chromium film as it would give more flexibility on manipulation and integration to technological process. A first step towards accomplishment of this approach is to explore how depositions of different DLC films affect the surface morphology and structural properties of water soluble polymer. Alternatively to protective film application, multifunctional improvement can be achieved by creating new chromium composite films. In this dissertation, this is achieved through combination of PVD process and oxygen plasma treatment of thin film. The later approach is radical new since no solutions were published or patented at the beginning of this doctoral dissertation, which would be applicable in the present context. To sum up, this dissertation aims to develop thin films with low surface roughness and improved scratch/wear resistance as compared to conventional chromium thin films. It covers – the systematic study of substrate surface preparation methods for improved chromium thin film adhesion to substrate; properties of chromium thin films deposited on glass using different PVD techniques; first step approaches of different DLC films and DLC-polymer composites on chromium thin films; and development of novel chromium composite films for lithography masks, glass scales and reticles.

Motivation

Chromium thin film on glass plays an important role in lithographic mask production as well as in precision scale gratings and reticles for photoelectric measurement systems. With the need for development of new, more accurate positioning and displacement measurement devices, high resolution and high accuracy are needed with stringent requirements for chromium thin films. A significant problem in photomasking is film roughness-induced, diffuse reflectance which leads to throughput loss, reduced image contrast and interference effects. Selection of vacuum deposition technique and control of deposition parameters, including temperature, pressure and bias voltage plays an important role in producing controlled surface roughness of chromium thin films on substrates. Roughness aside, another key parameter of scale gratings, lithographic masks and reticles is wear resistance, which is related to their long-term usage sustainability. The continuous improvement of the wear resistance should not negatively affect the optical properties of the chromium/glass composite system. The need for the functional, wear resistant chromium films has pushed the research toward new conceptual design of the films, as well as the development of the new technological approaches and deposition methods.

Research objective

The aim of this work – development of the novel chromium composite films for production of the advanced lithographic masks, glass scales and reticles.

Tasks of the dissertation

1. To investigate the influence of substrate surface preparation on the adhesion strength of chromium thin film to glass substrate.
2. To determine the surface morphology and structural properties of chromium thin films on glass substrates prepared using thermal evaporation and magnetron sputtering techniques.
3. To comparatively evaluate surface morphology, cohesive and adhesive properties of one-step and two-step thermally deposited chromium thin films on glass substrates.
4. To explore the tribological behaviour of two-step thermally deposited chromium thin films on glass substrates.
5. To comparatively evaluate surface morphology, cohesive and adhesive properties of DLC films on chromium thin film coated glass and to study the blend behavior of PVP upon DLC deposition via direct ion beam.

Scientific novelty of the work

1. Nanostructural differences of chromium thin films deposited on soda–lime–silica float glass substrates via thermal evaporation and magnetron sputtering techniques were revealed for the first time.
2. Novel chromium composite films (in this work denoted as two-step thermally deposited chromium films) were developed. They exhibited better mechanical strength and optical properties as compared with conventional chromium films.
3. Wear mechanisms of a-C:H, a-C:H/SiO_x and a-C:H:N/SiO_x films were revealed via combination of scratch test and atomic force microscopy.
4. For the first time, PVP surface modification was achieved using Hall-type closed drift ion beam source to deposit a-C:H/SiO_x and a-C:H:N/SiO_x thin films.

The key statements of the dissertation

1. Soda–lime–silica float glass substrate surface activation and contamination removal by O_2 plasma treatment process and RCA-1 (6 parts of deionized H_2O, 4 parts 27 % NH_4OH, 1 part 30 % H_2O_2) surface preparation method can effectively improve chromium thin film adhesive bonding to the substrate; when used in combination with thermal pretreatment (100 °C) in the vacuum chamber before chromium thin film deposition process even better adhesion can be obtained.
2. Chromium thin films consisting of nano-scale isolated surface mounds can be produced via thermal evaporation technique while in magnetron sputtered chromium thin films, these mounds tend to combine to form larger micrometer-scale islands.
3. Two-step thermal deposition of chromium thin films on glass substrates followed by O_2 plasma treatment after the first deposition improves chromium composite film adhesion to substrate and film cohesion as compared with conventional deposition process.
4. The friction coefficient of the two-step thermally deposited chromium films in dry sliding conditions is relatively high and stable at room temperature; wear of the film is governed by abrasion and fracture mechanisms; films exhibit low wear rates at room temperature.
5. The a-C:H/SiO_x and a-C:H:N/SiO_x films deposited on chromium coated glass show better mechanical strength as compared to conventional a-C:H films; interfacial interactions of PVP with the direct ion beam induce changes in the carbonyl group of the PVP and are dependent on the carrier gas used for the synthesis of the DLC films.

Dissertation structure

This dissertation is organized as follows. In Chapter 1, the literature review is presented. It covers main aspects of surface morphology and factors contributing to the formation and growth of the thin films; chromium thin films are reviewed with a focus on applications, structural properties, deposition techniques, film formation mechanism, surface morphology and adhesive properties; diamond-like carbon films are reviewed, in particular amorphous hydrogenated carbon films, covering their classification, applications, deposition techniques and methods, surface morphology and other properties; diamond-like carbon-polymer composites are introduced listing examples of different composite combinations with specific functional properties; soda-lime-silica float glass as a substrate is reviewed, introducing with properties, fabrication technology, typical chemical composition, structure and its surface preparation approaches. Chapter 2 covers materials, experimental techniques and methods used in this study; main specifications of technological and analytical equipment are provided. In Chapter 3, results and discussion are provided. Chapter 4 states the main conclusions about the findings of the investigation. It is followed by the extensive list of references containing 187 items.
This dissertation consists of 110 pages. Count of equations, figures and tables in all chapters is given in Table 1.

Table 1. Count of equations, figures and tables in all chapters.

Chapter No.	Numbered equations	Figures	Tables
Introduction	0	0	1
Chapter 1	0	15	0
Chapter 2	3	13	12
Chapter 3	0	38	8
Conclusions	0	0	0
Total count	3	66	21

Personal input of the author

Most of the results presented in the dissertation were obtained at Kaunas University of Technology. The author has independently planned experiments, performed technological processes and analytical measurements. Glass for experiments was supplied from the JSC “Precizika Metrology” which was a partner of Kaunas University of Technology in a Project of High technologies development programme of Agency for Science, Innovation and Technology “Nanostructured diamond-like carbon films for advanced optical metrology components (NanoDLC)”, where author participated as Project researcher. Vitoldas Kopustinskas has contributed to the soda-lime-silica float glass processing, DLC formation and ellipsometry measurements. Fanny Ecarla from CSM Instruments SA performed scratch testing. Dr. Tomas Polcar from Czech Technical University performed

tribological testing. Dr. Jonas Baltrusaitis at the University of Iowa performed X-ray photoelectron spectroscopy (XPS) and energy-dispersive X-ray spectroscopy measurements. Dr. Mindaugas Andrulevičius from Kaunas University of Technology performed XPS measurements. Dr. Arūnas Baltušnikas from Kaunas University of Thechnology performed X-ray diffractometry measurements. Dr. Judita Puišo, from Kaunas University of Technology, consulted on selection of water soluble polymer. Dr. Asta Guobienė from Kaunas University of Technology helped the author to perform highly sophisticated atomic force microscopy measurements at the scratch track critical loading sections. The analysis and interpretation of results was performed entirely by the author. The interpretation was discussed with scientific supervisor dr. Viktoras Grigaliūnas and dr. Igoris Prosyčevas from the Kaunas University of Technology. The co-authors of the publications have either participated in the experiments or contributed with their ideas and advices. Dr. Jonas Baltrušaitis from University of Twente has contributed with editing of several manuscripts. All the publications related to the dissertation were prepared by the author.

Approbation of the research results

The original scientific results of this dissertation were presented in (3) international conferences and published (6 items) mainly in high impact research journals indexed by the Institute for Scientific Information.

List of publications related to the dissertation

1. Lazauskas, Algirdas; Grigaliūnas, Viktoras. Float glass surface preparation methods for improved chromium film ahesive bonding // Materials science = Medžiagotyra / Kaunas University of Technology, Academy of Sciences of Lithuania. Kaunas : KTU. ISSN 1392-1320. 2012, Vol. 18, no. 2, p. 181-186. [Science Citation Index Expanded (Web of Science); INSPEC]. [IF: 0.522, AIF: 3.264 (E, 2012)].
2. Lazauskas, Algirdas; Grigaliūnas, Viktoras; Guobienė, Asta; Andrulevičius, Mindaugas; Baltrušaitis, Jonas. Atomic force microscopy and X-ray photoelectron spectroscopy evaluation of adhesion and nanostructure of thin Cr films// Thin Solid Films. Lausanne : Elsevier Science. ISSN 0040-6090. 2012, Vol. 520, iss. 19, p. 6328-6333. [Science Citation Index Expanded (Web of Science); Science Direct]. [IF: 1.604, AIF: 2.807 (E, 2012)].
3. Lazauskas, Algirdas; Grigaliūnas, Viktoras; Ecarla, F.; Caunii, M. A comparative evaluation of surface morphology, cohesive and adhesive properties of one-step and two-step thermal deposited chromium thin films on glass substrates // Applied Surface Science. Amsterdam : Elsevier. ISSN 0169-4332. 2012, Vol. 258, iss. 19, p. 7633-7638. [Science Citation Index Expanded (Web of Science); COMPENDEX; INSPEC; Science Direct]. [IF: 2.112, AIF: 2.994 (E, 2012)].

4. Lazauskas, Algirdas; Baltrušaitis, Jonas; Grigaliūnas, Viktoras; Baltušnikas, Arūnas; Abakevičienė, Brigita; Polcar, T. Tribological properties of the two-step thermally deposited chromium films // Applied Surface Science. Amsterdam : Elsevier. ISSN 0169-4332. 2013, Vol. 283, p. 1089-1095. [Science Citation Index Expanded (Web of Science); COMPENDEX; INSPEC; Science Direct]. [IF: 2.112, AIF: 2.994 (E, 2012)].
5. Lazauskas, Algirdas; Grigaliūnas, Viktoras; Meškinis, Šarūnas; Ecarla, F.; Baltrušaitis, Jonas. Surface morphology, cohesive and adhesive properties of amorphous hydrogenated carbon nanocomposite films // Applied Surface Science. Amsterdam : Elsevier. ISSN 0169-4332. 2013, Vol. 276, p. 543-549. [Science Citation Index Expanded (Web of Science); COMPENDEX; INSPEC; Science Direct]. [IF: 2.112, AIF: 2.994 (E, 2012)].
6. Lazauskas, Algirdas; Grigaliūnas, Viktoras; Guobienė, Asta; Puišo, Judita; Prosyčevas, Igoris; Baltrušaitis, Jonas. Polyvinylpyrrolidone surface modification with SiO_x containing amorphous hydrogenated carbon (a-C:H/SiO_x) and nitrogen-doped a-C:H/SiO_x films using Hall-type closed drift ion beam source // Thin Solid Films. Lausanne : Elsevier Science. ISSN 0040-6090. 2013, Vol. 538, p. 25-31. [Science Citation Index Expanded (Web of Science); Science Direct]. [IF: 1.604, AIF: 2.807 (E, 2012)].

List of conference contributions related to the dissertation

1. Advanced materials and technologies: 14-th international conference-school, August 27-31, 2012, Palanga, Lithuania. Poster presentation.
2. Spring Meeting of the European Materials Research Society (E-MRS), May 14-18, 2012, Strasbourg, France. Poster presentation.
3. Materials engineering 2011: 20th international conference, October 27-28, 2011, Kaunas, Lithuania. Poster presentation.

Publications not included in the dissertation

1. Lazauskas, Algirdas; Baltrušaitis, Jonas; Grigaliūnas, Viktoras; Jucius, Dalius; Guobienė, Asta; Prosyčevas, Igoris; Narmontas, Pranas. Characterization of plasma polymerized hexamethyldisiloxane films prepared by arc discharge // Plasma Chemistry and Plasma Processing. New York : Springer. ISSN 0272-4324. 2014, Vol. 34, iss. 2, p. 271-285. [Science Citation Index Expanded (Web of Science)]. [IF: 1.728, AIF: 2.344 (E, 2012)].
2. Jucius, Dalius; Grybas, Ignas; Grigaliūnas, Viktoras; Mikolajūnas, Marius; Lazauskas, Algirdas. UV imprint fabrication of polymeric scales for optical rotary encoders // Optics and Laser Technology. Oxford : Elsevier. ISSN 0030-3992. 2014, Vol. 56, p. 107-113. [Science Citation Index Expanded (Web of Science)]. [IF: 1,365, AIF: 2,518 (E, 2012)].
3. Lazauskas, Algirdas; Guobienė, Asta; Prosyčevas, Igoris; Baltrušaitis, Valentinas; Grigaliūnas, Viktoras; Narmontas, Pranas; Baltrušaitis, Jonas. Water droplet behavior on superhydrophobic SiO_2 nanocomposite films during icing/deicing cycles // Materials Characterization. New York : Elsevier. ISSN 1044-5803. 2013, Vol. 82, p. 9-16. [Science Citation Index Expanded (Web of Science); Science Direct]. [IF: 1.880, AIF: 0.822 (E, 2012)].
4. Pudlauskaitė, Jovita; Jankauskaitė, Virginija; Lazauskas, Algirdas; Prosyčevas, Igoris; Narmontas, Pranas. Ag/DNQ-novolac-based nanocomposite films for controllable UV lithography morphological patterning // Colloid and Polymer Science. New York : Springer. ISSN 0303-402X. 2013, Vol. 291, iss. 8, p. 1787-1793. [Science Citation Index Expanded (Web of Science)]. [IF: 2.161, AIF: 3.344 (E, 2012)].
5. Bansevičius, Ramutis Petras; Grybas, Ignas; Janušas, Giedrius; Lazauskas, Algirdas; Malinauskas, Karolis. Application of incremental polymeric scales for high precision piezoelectric angular positioning system // Journal of Vibroengineering / Vibromechanika, Lithuanian Academy of Sciences, Kaunas University of Technology, Vilnius Gediminas Technical University. Vilnius : Vibromechanika. ISSN 1392-8716. 2012, Vol. 14, iss. 3, p. 1215-1219. [Science Citation Index Expanded (Web of Science); Academic Search Complete; Central & Eastern European Academic Source (CEEAS); Computers & Applied Sciences Complete; Current Abstracts; Inspec; TOC Premier]. [IF: 0.452, AIF: 2.083 (E, 2012)].
6. Jucius, Dalius; Grigaliūnas, Viktoras; Kopustinskas, Vitoldas; Lazauskas, Algirdas; Guobienė, Asta. Wettability and optical properties of O_2 and CF_4 plasma treated biaxially oriented semicrystalline poly(ethylene terephthalate) films // Applied Surface Science. Amsterdam : Elsevier. ISSN 0169-4332. 2012, Vol. 263, p. 722-729. [Science Citation Index Expanded (Web of Science); COMPENDEX; INSPEC; Science Direct]. [IF: 2.112, AIF: 2.994 (E, 2012)].

1. LITERATURE REVIEW

1.1 Surface morphology and growth of thin films

Surface morphology is a broad term used to describe various surface components, such as roughness, topography, height/depth distribution of features, lateral periodicity of features, or lateral sizes of features. Surface morphology of thin films directly controls their functional properties. For instance, high surface area is desirable for applications in energy storage and energy conversion [1]. Surface inhomogeneities of thin films strongly influence the electrical conductivity because of additional charge scattering [2]. Surface morphology has a significant influence on the magnetic hysteresis of a magnetic film [3], and controls optical losses in optical waveguides [4]. Furthermore, it has a pronounced influence on adhesion [5]. As a rule, the resultant surface morphology of thin film is highly dependent on the deposition technique and selection of deposition parameters. There exist a number of deposition techniques for fabrication of thin films, including thermal evaporation, sputter deposition, chemical vapor deposition, ion beam deposition, and electrochemical deposition.

The growth of thin films using mentioned deposition techniques in many cases occurs under highly non-equilibrium conditions, which leads to a specific surface morphology and a complex temporal evolution [6]. For example, Fig. 1 shows an atomic force microscopy (AFM) image of a 100 nm thick indium tin oxide film grown by thermal evaporation technique at room temperature [7]. It can be seen that the surface contains mountains and valleys over a 1 μm × 1 μm scale. Obviously, surface morphology is complex and it cannot be predicted deterministically.

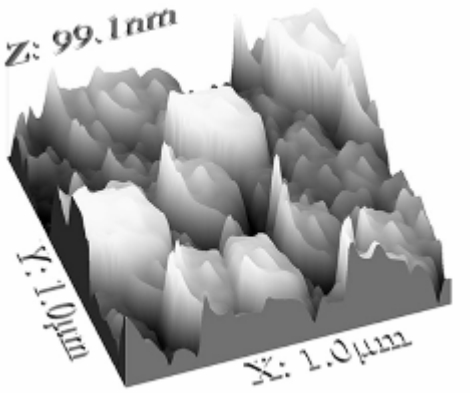

Fig. 1. An atomic force microscopy image of the surface morphology of a 100 m thick indium tin oxide film grown by thermal evaporation [7].

Many factors contribute to the formation and growth of such a complex surface morphology of a film. There is always random fluctuation, or noise, that exists

naturally during the deposition process as atoms do not arrive at the surface uniformly. Additionally, surface diffusion contributes to complex surface morphology if the experiment is performed at either a sufficiently low temperature and/or at a high deposition rate [6]. Geometrical shadowing, which is a result of deposition by a non-normal incident flux is also responsible for final surface morphology of the film [8]. In some cases, the particles can also be reemitted from the surface upon impact. A schematic of common film growth effects which may affect final surface morphology is illustrated in Fig. 2.

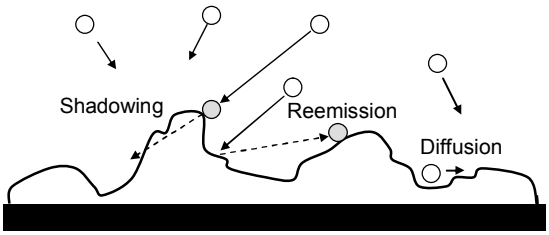

Fig. 2. Schematic of thin film growth effects that may affect final surface morphology. The incident particle flux may arrive at the surface with a wide angular distribution depending on the deposition methods and parameters.

Importantly, depending on the thin film deposition technique used, atoms arrive at the surface with characteristic trajectories. Fig. 3 shows schematic of geometries for several commonly employed deposition techniques, where the angle θ is defined as the angle between the incident atomic flux and the substrate surface normal [9].

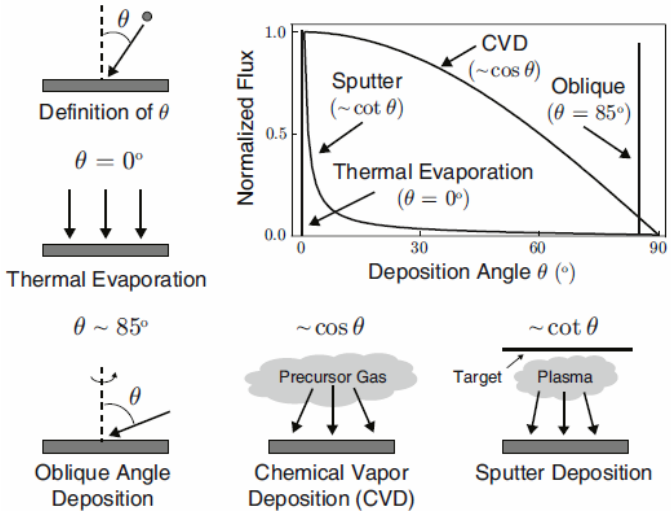

Fig. 3. Schematic of geometries for several commonly employed deposition techniques. The graph is a plot of the incident flux distribution of atoms [9].

For thermal evaporation the flux usually arrives at substrate surface with normal incidence ($\theta \approx 0°$). If the substrate is tilted with respect to the particle flux in

evaporation, the oblique angle deposition can be achieved with angles as large as 85º [10]. For chemical vapor deposition, the substrate undergoes a molecular flux coming from a wide range of angles and can be represented by a cosine distribution. For sputter deposition, the distribution is narrower and can be represented by a cotangent function [6]. Therefore, selection of deposition technique and control of deposition parameters is paramount to producing the specific film surface morphology for different applications.

Since the 1960s a significant efforts has been made to construct a classification of the surface morphology of a film depending on the deposition parameters. As a result the structure zone model emerged. A recent version of structure zone model shown in Fig. 4 indicates the distinct film surface morphologies obtained as a function of the renormalized film temperature T/T_M, where T_M is the melting point of the material being deposited, and of the ion energy, which is inversely related to the argon gas pressure in the sputter deposition technique used in that research [10-12]. The different surface morphologies shown in the structure zone model are mainly a consequence of the competition between the spatially disordered deposition of particles on the growing film surface and the ordering effect of activated particle mobility processes [11].

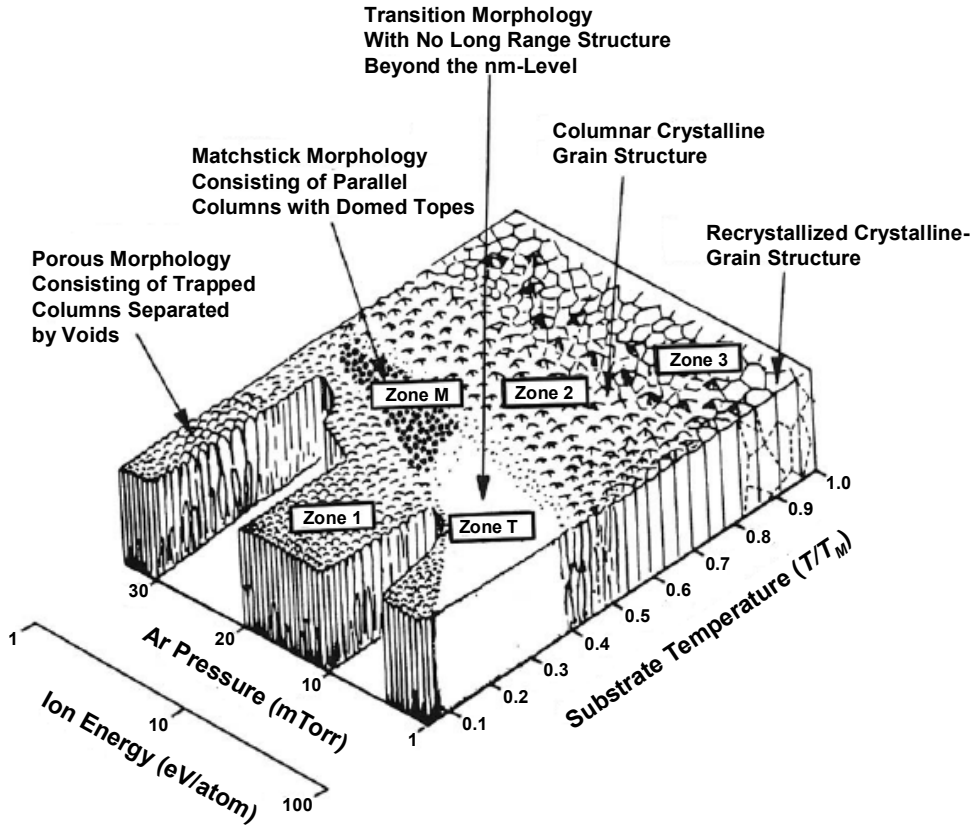

Fig. 4. A recent version of the structure zone model of film deposition [11].

The particle mobility (i.e. gas-induced mobility) can be driven by substrate surface temperature and by bombardment of molecules from the vapor [10]. This structure zone model describes well the trends seen in experiments with ceramics, semiconductors, and metals [11].

Currently, transport of atoms, shadowing effect, surface diffusion and materials in physical vapor deposition (PVD) processes can be simulated by Monte Carlo calculus with an improved prediction of the surface morphology, growth and some physical properties (e.g. density) of thin films. For instance, in Ref. [13] a Monte Carlo simulation method has been used to simulate the growth of inclined columnar chromium films. The comparison to simulated films with equivalent structure deposited by sputtering gave a good concordance, as shown in Fig. 5. However, Monte Carlo simulations are sophisticated and unacceptably time consuming. Thus, experimentally driven PVD practice and characterization of thin films using analytical techniques is still a priority.

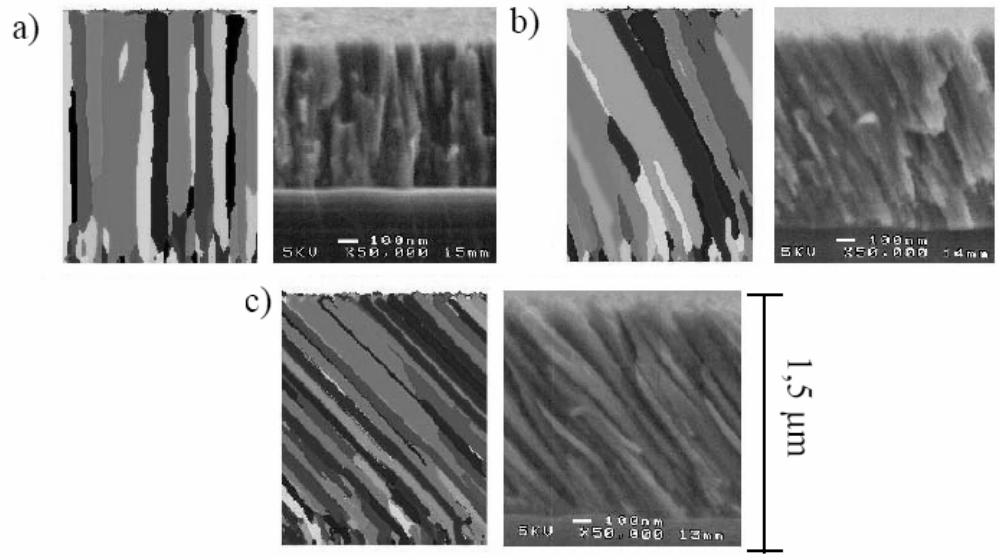

Fig. 5. Simulated and scanning electron microscope (SEM) micrographs of cross-section of oriented chromium thin films. The angle between the flux trajectory and the normal of the substrate a) 0º, b) 40º and c) 60º [13].

1.2 Chromium thin films

The chromium films have been one of the most popular coatings because of their high corrosion resistance, better stability at high temperature, high wear resistance and having a bright and non-tarnishing appearance [14]. Due to these properties, chromium thin films found their use in the field of automotive, aerospace and decorative industries for many years [15]. Chromium thin films are also highly valued for its specific magnetic and optical properties. The latter plays an important role in photomask production for ultraviolet (UV) lithography applications as well

as in precision scale gratings and reticles for photoelectric measurement systems. Photomasks are the backbone of microfabrication and semiconductor industries. Precision scale gratings and reticles are the main parts of optical encoders, which are operated in many technical systems such as robots, machine tools, rotary tables, laser trackers and telescopes [16]. In both cases, patterned chromium film performs a function to block a light transmission through the glass or quartz.

The traditional hard chromium film deposition method is chromium plating, a wet electrolytic method. However, chromium plating baths contain hexavalent chromium Cr(VI), which is a genotoxic carcinogen. Chronic inhalation of Cr(VI) compounds increases the risk of lung cancer [17]. Therefore, there is increasing pressure for shift towards the health and environmental friendly deposition methods, for instance a physical vapor deposition (PVD) method. Thermally evaporated, sputtered or cathodic arc evaporated Cr, CrN, and CrC, but also chromium free coatings like diamond-like carbon (DLC), are considered as possible substitutes for electroplated hard chromium films in the large scale industrial applications [18].

At room temperature, chromium has a body-centered cubic (bcc) lattice with lattice constant having a value of 2.88 Å. Most common crystallographic plane orientations of chromium are bcc (110) or bcc (200) (see Fig. 6) or both. In PVD process of chromium thin film deposition the crystallographic plane orientation can be tuned by changing technological parameters and deposition conditions.

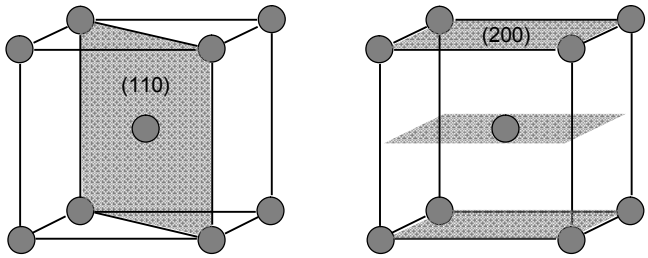

Fig. 6. Most common crystallographic plane orientations of chromium.

Previous X-ray diffraction (XRD) studies [19-21] of chromium thin films deposited on the glass substrates have demonstrated that with no substrate heating (or with substrate heating at the temperatures lower than 100°C), the body-centered cubic (110) plane of chromium metal crystal lattice is observable, while with the substrate heating temperatures in the range of 250-350 °C the body-centered cubic (200) plane of chromium metal crystal lattice structure is observable. In a study conducted by. P. Kim et. al, chromium thin films were deposited using a thermal evaporation technique [22]. Glass was used as a substrate. The substrate temperature was fixed at 250°C and the chromium film thickness was changed from 27 to 200 nm. Fig. 7 shows XRD diffraction patterns of chromium thin films with various thicknesses. It was found that (200) plane orientation develops drastically with the chromium film thickness, whereas, the (110) plane orientation does not change significantly. At about 100nm, the two common orientations were comparable. Also, the grain size of the chromium film was found to increase with film thickness.

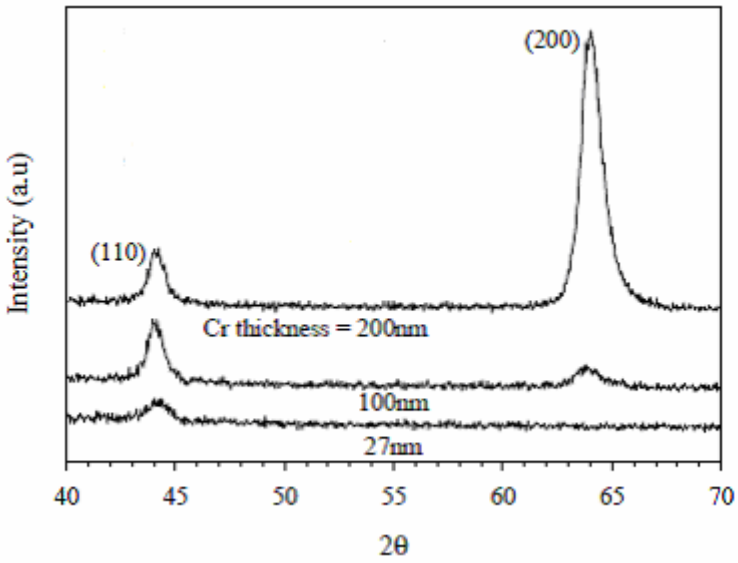

Fig. 7. XRD diffraction patterns of chromium films with various thicknesses. The (110) and (200) plane orientations appear at 44.1° and 64°, respectively [22].

In another experiment, substrate temperature was fixed at 250°C and the thickness was kept at 100nm while Ar pressure was varied from 2×10^{-2} to 4×10^{-2} mbar. It was found that Ar pressure equally affected the (110) and (200) plane orientations. In a study conducted by C. Gautier, chromium thin films were deposited by vacuum arc evaporation [19]. It was found that bias voltage had a strong influence on crystallographic plane orientations. The increase in bias voltage (in absolute value) enhanced the (110) plane orientation. It was also found that the crystallographic plane orientations of the chromium films were sensitive to the presence of impurities.

Control of the preferred crystallographic plane orientation of chromium is important for different applications e.g. (200) plane of chromium metal crystal lattice structure is desirable when the chromium thin film is used as an under-layer for cobalt-based magnetic film in magnetic recording applications [23].

Under normal atmospheric conditions chromium forms a very dense thin passivating oxide layer. Thin oxide layer provides corrosion resistance by blocking the diffusion of oxygen into the underlying material. It is also stable against acids. Among the various chromium oxides, Cr_2O_3 (i.e. alpha phase) is the most stable under ambient conditions. The stable phases also include: CrO, Cr_2O, CrO_2 and Cr_3O_4 [24]. Chromium oxides (Cr_xO_y) are important in high-temperature resistant materials, liquid crystal displays, catalysts [25], wear and corrosion resistant films, optically selective surfaces of solar collectors etc. Specifically, chromium alpha phase has a corundum structure, which is a hexagonal lattice. It can be shown as A-B-A-B-... close-packed [26] layers of oxygen atoms with a hexagonal arrangement of chromium atoms on each side of the oxygen layer. The lattice constants have a value of 4.95 Å and 13.58 Å [27]. The latter corresponds to six oxygen packing

planes. It was shown in [28] that oxidation of 1 nm thick chromium film with (110) plane orientation observable results in formation of 2.02 nm thick Cr_2O_3(0001) structure. From a crystallographic point of view, the close-packed oxygen sublattice of Cr_2O_3(0001) matches well to the Cr(110) film surface. The oxygen-oxygen nearest-neighbor distance is 2.86 Å; whereas, the chromium-chromium next-nearest-neighbor distance is 2.88 Å. Thus, the lattice mismatch is only -0.7% in the [100] direction [29].

Chromium thin film formation mechanism was investigated in [30] employing X-ray photoelectron spectroscopy (XPS). Chromium thin films were deposited using thermal evaporation technique. The base pressure in the system was 0.027 Pa. Approximately 50 mg of chromium granules (1 to 4 mm in diameter, 95% purity) were placed in the tungsten holder, which was located 170 mm below the probe. The tungsten holder was heated up to 1573 K using an electric current. It was found that metallic chromium film condensation starts when the thin Cr_2O_3 layer is built on the substrate surface. Fig. 8 shows XPS Cr 2p region analysis. The Cr_2O_3 can be detected from the peak at 576.6 eV. At the intermediate stages of the deposition, metallic chromium starts to build up on top of Cr_2O_3 layer, which can be detected by the appearance of a new peak at 574.1 eV, which is assigned to chromium metal [30]. Thus, conventional chromium thin film prepared by PVD method can be interpreted as Cr_xO_y/Cr/Cr_xO_y composite system. The top and bottom layers of the film are Cr_xO_y and the middle layer is metallic chromium.

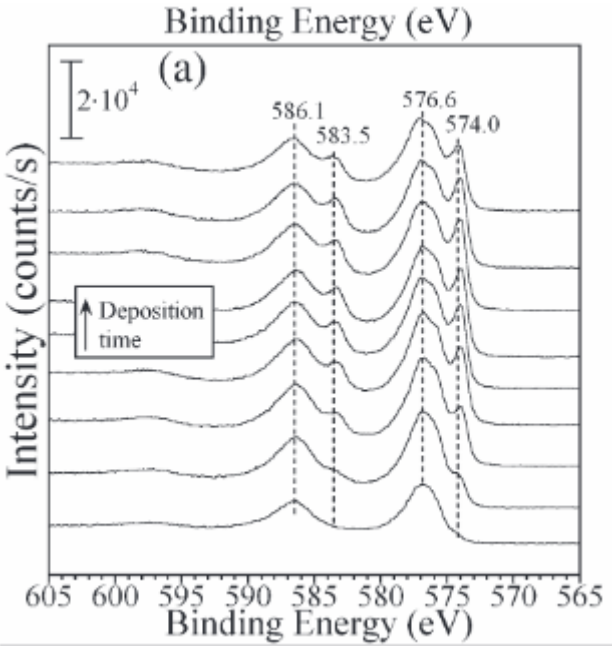

Fig. 8. High resolution XPS spectra of 2p Cr at every deposition step. The evolution of Cr_2O_3 and chromium metal can be seen from the spectra [30].

Surface morphology of chromium thin films is highly dependent on deposition technique and deposition parameters. Further, several cases from previous studies are presented as supporting information. In Ref. [31] chromium films were sputter deposited from a chromium target (purity 99.6 %) with an argon pressure of 0.6 Pa, and at room temperature on Si(100) substrates. The base pressure was lower than 10^{-5} Pa before introduction of argon. Fig. 9 (left) and (right) shows AFM and SEM images of chromium film (thickness ≥ 1 μm) sputter deposited on Si(100) substrate at normal incidence, respectively.

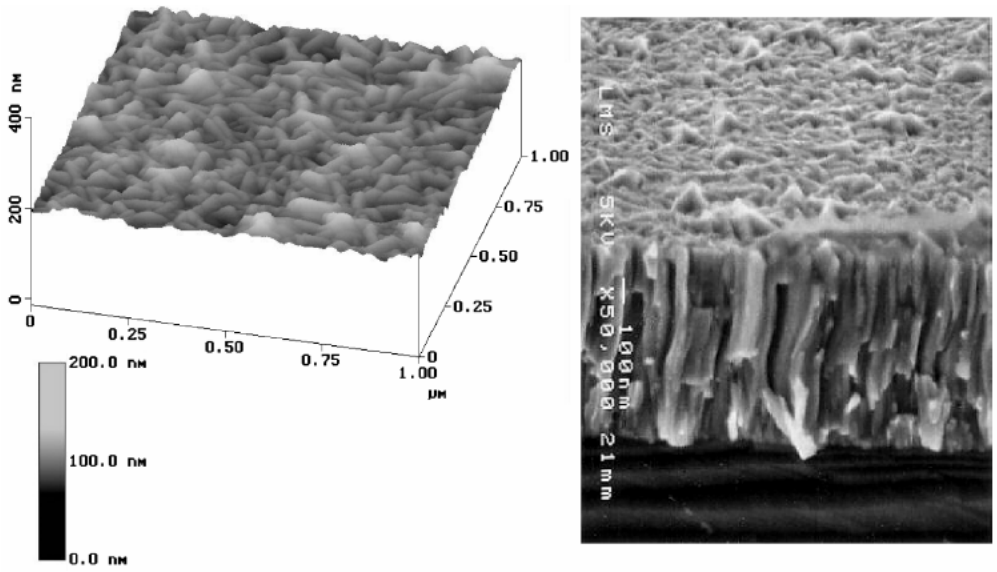

Fig. 9. (left) AFM and (right) SEM images of chromium film sputter deposited on Si(100) substrate [31].

Authors indicated that as deposited chromium films were composed of thin columns separated by voids, in good agreement with structure zone model (corresponding to Zone 1 indicated in Fig. 4). Chromium films had a root mean square roughness of 8.7 ± 1.8 nm (measured by AFM). In a study conducted by S. Agarwal, chromium thin film was deposited on Si(100) substrate using electron beam (e-beam) evaporation technique [32]. The deposition process was carried out under the vacuum of 2×10^{-8} Torr. Thickness of the film was 25 nm. Fig. 10 shows AFM topography image of chromium film. In contrast to sputter deposition, e-beam deposition produced a smoother chromium film having a root mean square roughness of 0.817 nm. Note that in both cases the AFM scan size was 1 μm × 1 μm as indicated in Fig. 9(left) and Fig. 10.

It was demonstrated in [33], that selection of PVD technique can significantly alter the properties of chromium thin film required for the specific application. J. Wang et al. studied the etching effect of chromium film through a surface reaction induced by an electron beam and enhanced with XeF_2 gas. Specifically, this dry etching technique is used for removal of a chromium thin film for the direct fabrication of microstructures on the film and for the repair of defects on

photolithography masks. It was found that e-beam deposited chromium films can be etched when exposed to XeF_2 and irradiated with an electron beam. The etch rate made by an e-beam of 20 keV was five times higher compared to that made by e-beam of 10 keV. In contrast, the authors concluded that sputter deposited chromium thin films cannot be etched under the same conditions as e-beam deposited chromium films. The sputtered films contained small amounts of iron impurities (more likely sputtered from the ground shield of sputter gun), which had a significant effect on the etch process.

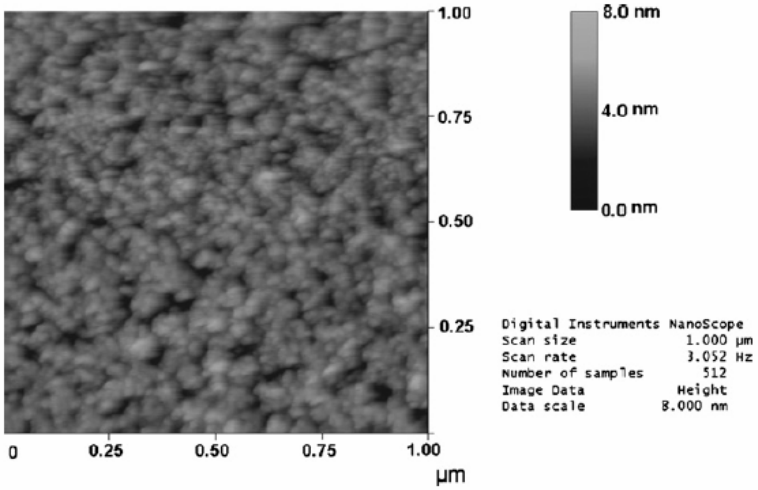

Fig. 10. AFM image of e-beam evaporated chromium film on Si(100) substrate [32].

Thin chromium films are frequently used as intermediate (also called adhesive layers or interlayers) layers to ensure good adhesion between thin films of gold, aluminum, copper, and diamond-like carbon and the substrate material (e.g. glass, silicon) in a number of different applications [34-36]. In Ref. [34], the influence of the chromium intermediate layer between various diamond-like carbon films and steel substrate on tribological performance of diamond-like carbon films was investigated. They concluded that the intermediate layer is necessary to improve the interface between the diamond-like carbon film and the substrate. Otherwise, the diamond-like carbon film deteriorates faster under tribological testing. In another study conducted by G. Wei et al., the tribological behaviour of DC magnetron sputtered Cr, Cr_2N and CrN thin films on Si(100) substrates has been studied using scratch techniques [37]. Specifically, Chromium nitride (Cr–N)-based coatings are also used for tribological applications as chromium films. The loads greater than 5 mN were needed to delaminate the 500 nm thick Cr, Cr_2N and CrN thin films from Si(100) substrate. When tested for adhesion to Si(100) substrate, Cr films performed the best, followed by CrN and Cr_2N.

The need for high quality chromium thin films constantly rises. So they are today, they are expected to be used in a variety of fields in the future.

1.3 Diamond-like carbon films

Diamond-like carbon (DLC) belongs to a metastable phase of carbon, which has a random network of covalently bonded carbon in sp^3 and sp^2 local coordination, with some of the bonds terminated by H [38]. DLC films can be divided into two broad categories based on their structure: amorphous carbon and amorphous hydrogenated carbon (a-C:H) both having a high fraction of metastable sp^3 carbon bonds which determine the "diamond-like" structure of the DLC films [39]. Specifically, amorphous hydrogenated carbon films can be classified into four types [40]:

1. a-C:H films with the highest H content (40-60 atomic %). These films have up to 70% sp^3. Most of sp3 bonds are hydrogen terminated. The films of this type are soft and have low density. This type is sometimes called polymer-like a-C:H.
2. a-C:H films with intermediate H content (20-40 atomic %). These films have better mechanical properties than the 1 type because they have more C-C sp^3 bonds. This type is sometimes called diamond-like a-C:H.
3. Hydrogenated tetrahedral amorphous carbon (ta-C:H) films. In ta-C:H films CC sp^3 content can be increased while keeping a fixed H content. These films can have highest sp^3 content (~70%) and 25-30 atomic % H. ta-C:H films have higher density (up to 2.4 g/cm^3) and Young's modulus (up to 300 GPa).
4. a-C:H films with low H content (less than 20 atomic %). They have a high sp^3 content and sp^2 clustering. This type is sometimes called graphite-like a-C:H.

The amorphous nature of DLC opens up the possibility of incorporating other elements such as Si, F, P, Ag and N [41-44] which can result in a new or improved functionality of the material. Depending on the sp^3 (diamond-like) and sp^2 (graphite-like) bond content, hydrogen and other incorporated element concentration, DLC physical properties could be altered to obtain friction and wear reduction [45, 46], biocompatibility, hemocompatibility, prevention of metal ion release [47-49], exceptional optical transmission and antireflection [50, 51] functionality of the materials. Commonly used DLC deposition techniques include filtered cathodic arc, plasma enhanced chemical vapor deposition (PECVD), direct ion beam, electron cyclotron resonance plasma chemical vapor deposition and DC/RF sputtering [52-55]. Direct ion beam deposition in particular has some advantages over the other methods of hydrogenated amorphous carbon film synthesis. Parameters of the film growth process such as ion beam energy, plasma power, substrate temperature, system pressure, gas composition can be precisely controlled over a wide range of conditions. DLC films can be deposited onto electrically conductive and insulating materials providing flexibility that one needs in designing and developing multifunctional films [56, 57]. However, DLC films exhibit some undesirable properties such as high compressive residual stress, which arise due to the energetic deposition processes of these films. The residual stress may cause mechanical instability of the DLC resulting in adhesion failures and delamination of the films

from the substrate surface. The elimination and release of residual stress may also be the cause of the undesirable morphological and microstructural changes of the films [58]. As a result, there is considerable interest in developing synthesis and surface treatment approaches oriented towards enhancing the adhesive performance of DLC films. A common practice is to use a metallic interlayer deposited between the substrate surface and the DLC film; for instance chromium, titanium, tungsten, or silicon [59]. Other methods include plasmochemical treatment of the substrate surface, doping of DLC itself or a combination [60] of these.

Further, it will be shown, how the surface morphology of DLC films could be altered by changing the precursors/gases used for deposition. In a study conducted by R.G. Turri et al., PECVD technique was employed to produce different DLC films [61]. The films were all based on amorphous hydrogenated carbon, a-C:H, but, in addition, fluorine, chlorine, and silicon and oxygen, were incorporated to produce a-C:H:F, a-C:H:Cl and SiOx containing a-C:H (a-C:H/SiO_x) films, respectively. The precursors/gases were, respectively, benzene/argon, benzene/sulfur hexafluoride, acetylene/chloroform, hexamethyldisiloxane/argon. Deposition times of 15–25 min were used. Fig. 11 shows AFM topography images of different DLC films produced using PECVD technique. It is clear, that the DLC films exhibit different surface morphology. The films had a root mean square roughness of 0.535 nm (a-C:H), 0.484 nm (a-C:H:F), 0.844 nm (a-C:H:Cl) and 0.801 nm (a-C:H/SiO_x).

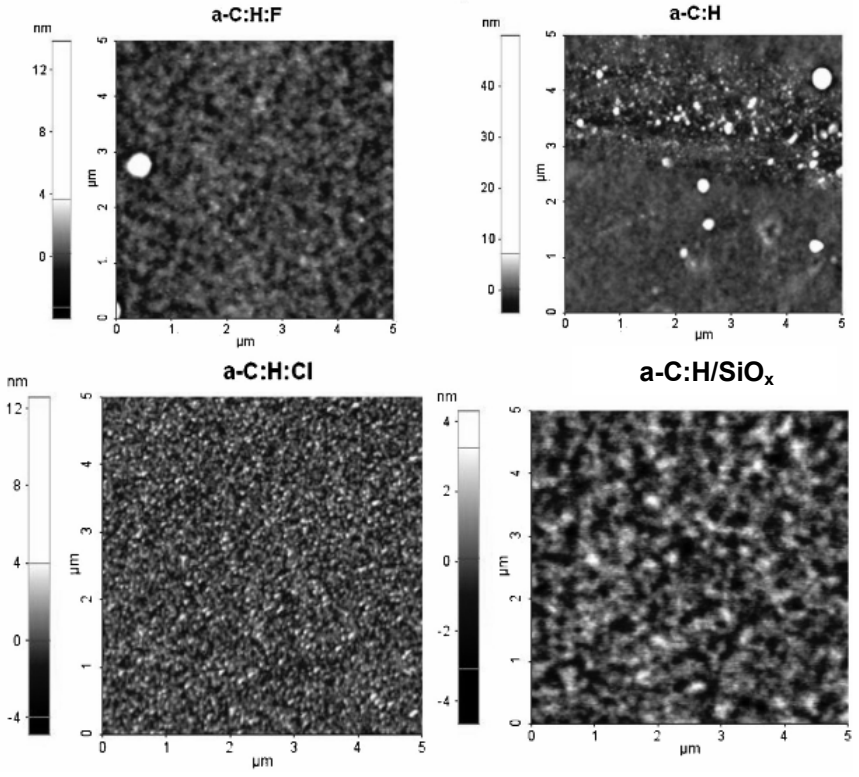

Fig. 11. AFM images of different DLC films produced using PECVD technique [61].

In a study conducted D.P. Liu, a-C:H films were deposited on silicon substrates from low-pressure dielectric barrier discharge plasmas of CH_4 and their properties depending on CH_4 gas pressure were investigated [62]. Fig. 12 shows AFM topography images of a-C:H films produced at different CH_4 pressures. It was found that the surface of the a-C:H film produced at the pressure of 100 Pa was relatively smooth while these films produced at pressures of 400 Pa had rougher surfaces. The a-C:H films prepared at CH_4 pressure of 70 Pa exhibited lower friction coefficient (0.107) which was associated with its graphite-like surface structure (i.e. type 4 a-C:H). The variation of friction coefficient with the CH_4 pressure in the range of 100–500 Pa was explained by the changes in surface morphology (specifically, increase in root mean square roughness) with increase of CH_4 pressure.

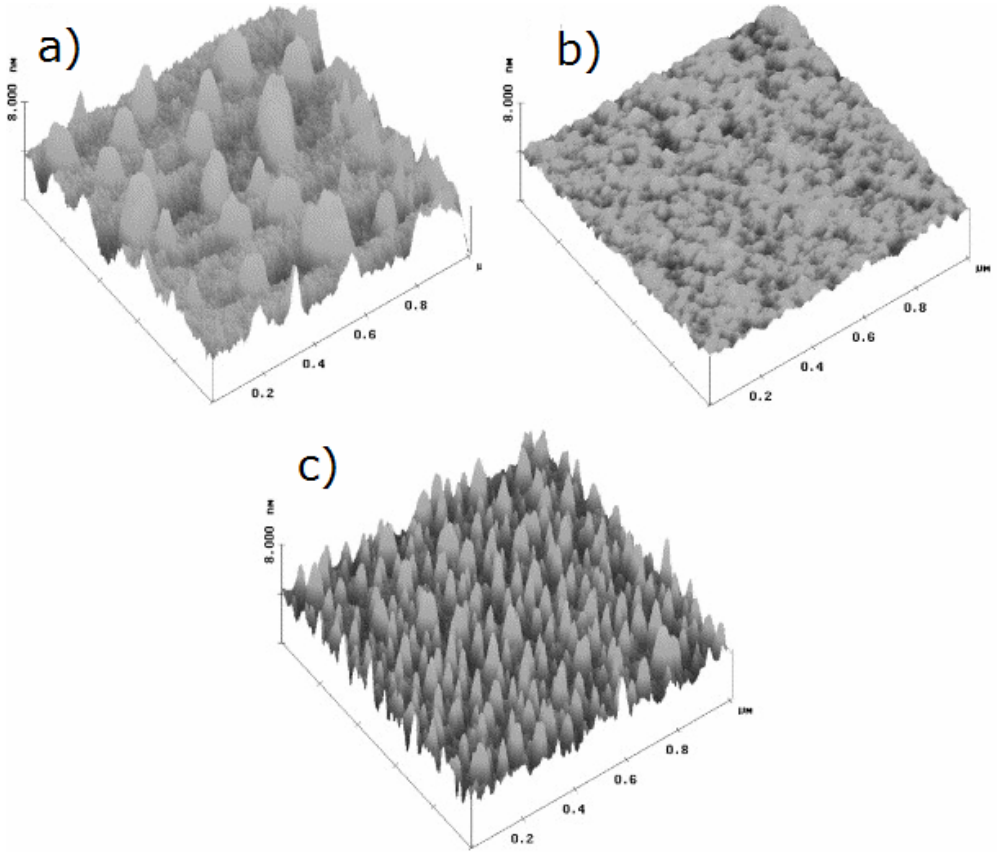

Fig. 12. AFM topography images of a-C:H films produced at CH_4 pressures of (a) 70 Pa, (b) 100 Pa and (c) 400 Pa [62].

A lot is already done in the area of DLC films. They were proven to be applicable, and are already used in practical applications. It is expected that more and more commercial products with incorporated DLC film functionality will come in the future.

1.4 Diamond-like carbon-polymer composites

The nature of the surface of polymeric materials determines its success in almost every industry. In order to enhance the versatility and usefulness of a polymeric material, the surface can be modified to achieve a variety of goals, including increasing adhesion, improving wettability, adding biocompatible features, reducing friction, reducing susceptibility to harsh chemicals or environmental agents, and increasing dye absorption. Surface modification approaches range from wet chemical surface modification to processes such as vacuum deposition, plasmochemical treatment, laser, ion, electron and microwave irradiation [63]. Exposing the surface of polymers to an ion beam results in the formation of various structures such as wrinkles, dots and ripples [63-66]. These surface features (denoted as self-assembly structure) can be controlled by the ion beam parameters, including the ion beam energy, plasma power, substrate temperature, system pressure, and gas composition. The myriad of variable parameters enables the design and fabrication of functional surface topographies.

Recently, R. Asakawa et al. introduced an attractive strategy of polymeric surface modification [67]. R. Asakawa et al. attempted to combine diamond-like carbon (DLC) with polymers that could enhance the original properties of the materials. Depending on the sp^3 (graphite-like) and sp^2 (diamond-like) bonds, hydrogen content and the concentration of elemental impurities, DLC physical properties could be modified to reduce friction, metal ion release, wear and tear on the material as well as enhancing biocompatibility, haemocompatibility, optical transmission and antireflection functionality. The combination of the outstanding physical properties of DLC with those of polymer coatings have attracted much scientific interest resulting in a number of novel applications for the DLC-polymer composites [68, 69]. For instance, high gas barrier polyethylene terephthalate bottles coated by a-C:H films have been commercially available in the market. Blocking the passage of gas molecules through polyethylene terephthalate wall (Fig. 13) using thin gas barrier films minimizes the negative impact on the recycling process due to very low level contamination by different materials [69]. In a study conducted by A. Anttila et al. non-stick and hard DLC-polymer hybrids were prepared using filtered pulsed arc discharge technique from a graphite polymer cathode [70]. Polydimethylsiloxane (PDMS) and polytetrafluoroethylene (PTFE) were used as sample polymers. The best measured water contact angles and droplet sliding angles were 112º and 3º, respectively. The peeling force in the 180º back peel test was over 100 times lower for DLC-polymer (in case of PDMS) than for bulk PTFE. S. Nagashima et al. have shown the fabrication of ordered, wrinkled DLC film on grooved surfaces of PDMS substrates [71]. The grooved surfaces of the PDMS specimens were treated with Ar plasma, followed by deposition of DLC film with a radio frequency (RF) PECVD apparatus (frequency of 13.56 MHz). The Ar plasma treatment duration was varied in the range of 1-7 min. The DLC film was subsequently deposited onto the surface from acetylene (C_2H_2) gas with a pressure of 13.3 Pa. The film thickness was ~40 nm. Fig. 14 shows the SEM images of the

DLC-coated grooved PDMS substrates pre-treated with Ar plasma for varying durations.

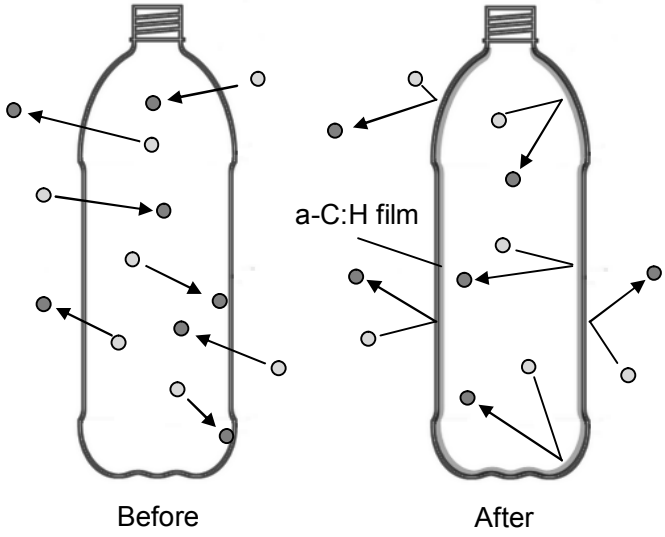

Fig. 13. Schematic of gas barrier mechanism of a-C:H film on polyethylene terephthalate bottle. (left) Gas molecules can pass through polyethylene terephthalate bottle walls. (right) a-C:H film blocks the passage of gas molecules.

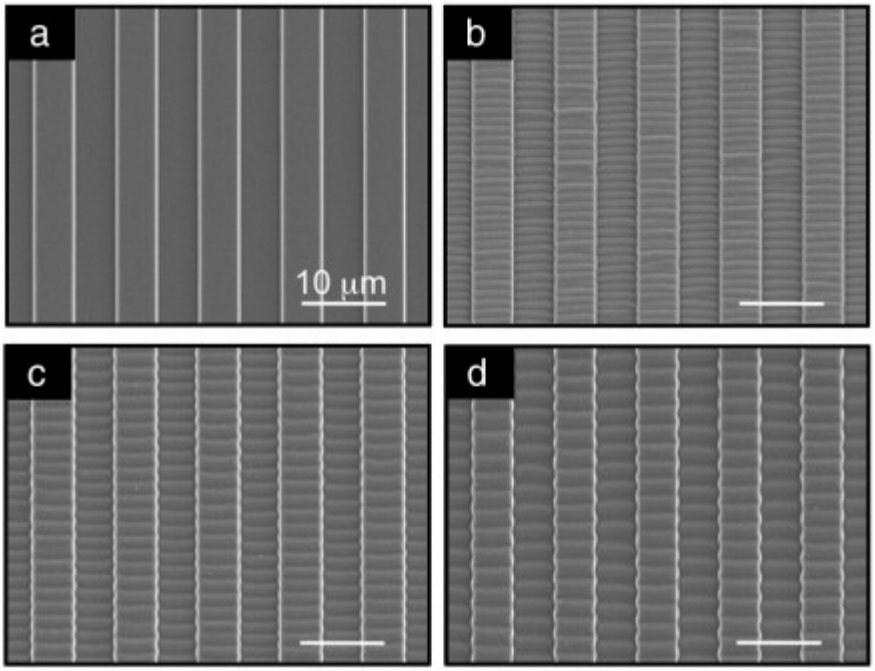

Fig. 14. SEM images of DLC-coated grooved PDMS substrates pre-treated with Ar plasma for varying durations: (a) Untreated; (b) 1 min; (c) 3 min and (d) 5 min [71].

They were able to control the wavelength and the amplitude of the wrinkles in the submicron- to micron-scale range simply by controlling the duration of Ar plasma pre-treatment. The authors concluded that such DLC-polymer system could be used in the field of biomedical engineering. These supportive examples indicate that DLC-polymer composites already opened new avenues for advanced materials and technologies in a wide span of applications. This area is quite new, so it is expected that a lot of new discoveries are coming in the future. Further investigations of different types of DLC and polymer combinations are needed to expand functionality features and application areas of these promising composite materials. Specifically, polyvinylpyrrolidone (PVP), also commonly called polyvidone or povidone, is a water-soluble polymer made from the monomer N-vinylpyrrolidone [72]. It has important applications in a variety of biotechnology areas, including tissue engineering, controlled drug release, separation of biomacromolecules and use as a biosensor [73, 74]. The DLC-PVP system (in our case is denoted as DLC-PVP composite film) was investigated in this dissertation. It was interesting to explore DLC-PVP composite film properties "on the edge".

1.5 Soda–lime–silica float glass as a substrate and its surface preparation methods

Soda–lime–silica float glass is an amorphous solid material widely used as a substrate in microelectronic, mechanical systems or "lab-on-a-chip" applications because of its excellent chemical durability and inexpensiveness [75]. Float glass has excellent flatness over a large area without polishing and the productivity is extremely high. 90 % of the world's production of flat glass is formed using float technology [76, 77]. Molten glass is poured onto a liquid tin bath, on which it cools and solidifies to produce two flat and parallel surfaces of a sheet. The surface in contact with the molten tin bath experiences tin diffusion and is referred to as the "tin side" while the top side, often called the "air side", can experience surface dealkalization because of the surrounding environment [78]. The tin side is also in contact with supporting rollers during heat treatment. After solidification, the continuous glass sheet undergoes a carefully controlled cooling process to eliminate any residual stresses before being cut into sheets for subsequent use. Thus the two sides of the glass sheet undergo different histories during processing [79]. Glass composition varies depending on its purposes. Typical soda–lime–silica float glass chemical composition by weight include 73% SiO_2, 14% Na_2O, 9% CaO, 4% MgO, 0.15% Al_2O_3, 0.03% K_2O, 0.02% TiO_2 and 0.1% Fe_2O_3 [80]. Fig. 15 shows schematic example of amorphous SiO_2 glass network. It is shown that some silicon ions in the network can be substituted by other large charge and small size cations (e.g. Na^+ and Ca^{2+}).

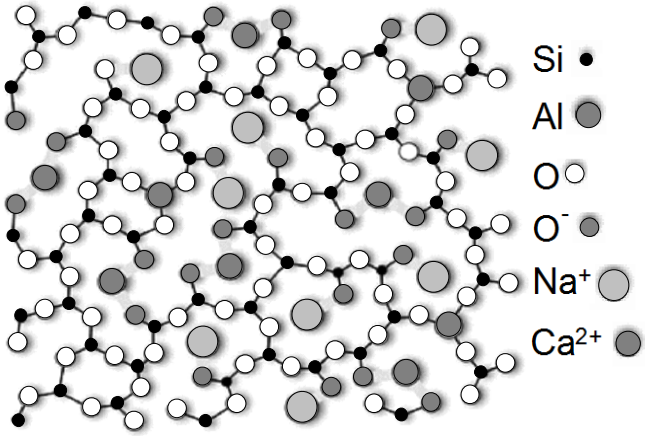

Fig. 15. Amorphous glass structure [81].

Thin films on glass are made to produce controlled specific variations of their optical, electrical, mechanical and chemical properties. The glass to be coated with a thin film may have two different functions: it can be an active element (e.g. a lens) or a passive element (e.g. a substrate) [81]. The deposited thin films may be either functional or decorative in their technical applications.

A clean, dry substrate surface is a necessary prerequisite for adhesive bonding. Rarely can a structural adhesive penetrate through surface contaminants to provide an optimum bond on an unclean surface. Therefore, surface preparation is essential for manufacturing high-quality glass substrate based products coated with thin films. Soda–lime–silica float glass surface preparation methods can be grouped into two categories: wet chemical cleaning involving solvents, and dry cleaning involving ions, electrons, free radicals, and other neutral species. Prominent examples of wet chemical cleaning processes for glass substrates are RCA-1 clean, RCA-2 clean and piranha clean. RCA-1 and piranha are used as a glass surface preparation methods for removing organic residues and certain metals [82]. RCA-2 for removing atomic and ionic contaminants. If wrongly applied, cleaning is replaced by etching and from the aqueous cleaning processes a surface roughening can result [83]. For large volumes of glass substrates an ultrasonic cleaning with aqueous solution containing detergent and surfactant is used. It is effective in removing large contaminants but removal of micro contaminants requires greater mechanical energy e. g. high velocity water jet cleaning process [84]. For modification of glass surface chemistry, dealkalization processes of exposure of glass substrates to atmospheric humidity (also known as weathering) or hot deionized water (also referred to as leaching) for a period of 3 – 4 days are used [78]. A typical example of dry glass surface preparation method is plasma treatment [85]. Plasma treatment can be used for surface activation and contamination removal. Surface activation is a process where surface functional groups are replaced with different atoms or chemical groups from the plasma utilizing source gases such as oxygen, hydrogen, argon, or a mixture of these gases. Surface contamination (i. e. residual organic solvents, oxidation, epoxy

residue and etc.) removal by plasma is an ablation process, where physical sputtering and chemical etching are the key processes involved [86]. Oxygen plasmas create an acidic, while nitrogen produces an alkaline chemistry. Oxygen plasmas are very effective in oxidizing residual hydrocarbon and other organic contamination. Argon plasmas are useful in decomposing and desorbing organics [87].

2. EXPERIMENTAL TECHNIQUES AND METHODS

2.1 Technological methods and equipment

2.1.1 Materials

A commercial soda-lime-silica float glass of thickness 1 mm was used in this study. The chemical composition by weight for the clear float glass was provided by manufacturer (Pilkington NSG Group Flat Glass Business) and is as follows: 72.6 % SiO_2, 13.9 % Na_2O, 8.4 % CaO, 3.9 % MgO, 1.1 % Al_2O_3, 0.6 % K_2O, 0.2 % SO_3, 0.11 % Fe_2O_3. The glass was obtained without any acid interleave coatings on their surfaces. Observing the fluorescence under UV illumination easily identified the tin side of float glass.

Deionized (DI) water (H_2O), 99.8% acetone (REACHEM Slovakia s.r.o.), 27 % ammonium hydroxide (NH_4OH) (REACHEM Slovakia s.r.o.), 30 % hydrogen peroxide (H_2O_2) (REACHEM Slovakia s.r.o.), argon gas (AGA SIA), oxygen gas (AGA SIA) and 96 % sulfuric acid (H_2SO_4) (REACHEM Slovakia s.r.o.) was used for surface preparation of glass.

The >95% pure chromium granules (1 to 4 mm diameter) and chromium disk ~76 mm in diameter was used for chromium thin film deposition.

Acetylene (C_2H_2) gas (AGA SIA), nitrogen (N_2) gas (AGA SIA), hydrogen (H_2) gas, ≥99.5% hexamethyldisiloxane (HMDSO) ($(CH_3)_3SiOSi(CH_3)_3$) (Sigma-Aldrich Co.) was used for synthesis of amorphous hydrogenated carbon (a-C:H), SiO_x containing a-C:H (a-C:H/SiO_x) and nitrogen doped a-C:H/SiO_x (a-C:H:N/SiO_x) thin films.

The 96 % ethanol (REACHEM Slovakia s.r.o.) and polyvinylpyrrolidone (PVP) [MW ~ 58 000] (Sigma-Aldrich Co.) was used for polymeric interlayer formation.

2.1.2 Substrate surface preparation

Glass was cut into (3 × 3) cm^2 slides. The air and tin sides of the float glass were subjected to nine surface preparation methods in order to remove debris, possible reaction products, organic contaminants that might exist on the surfaces. Surface

preparation methods included: rinsing with deionized (DI) H_2O and drying under compressed air (chosen as reference method); processing using ion-plasma preparation method: the slides were exploited in O_2 plasma; ultrasonic cleaning in acetone for 10 min; leaching: glass slides were immersed in 50 °C DI H_2O for a period of 5 days; a batch of RCA-1 cleaning solution (6 parts DI H_2O, 4 parts 27 % NH_4OH, 1 part 30 % H_2O_2) was prepared and heated on a hot plate until it bubbled vigorously. The slides were then immersed in this solution for 60 min with continued heating and stirring. Subsequently, slides were rinsed 3 times with deionized water and dried under compressed air; bombardment by Ar^+ ion beam; Piranha clean: a batch of Piranha cleaning solution (2 parts concentrated 96 % sulfuric acid H_2SO_4, 1 part 30 % hydrogen peroxide H_2O_2) was prepared and heated until it bubbled vigorously. The glass slides were left normally for 30 min in the solution, after which they were removed rinsed 3 times with deionized water and dried under compressed air. The summary of surface preparation methods used in this study is presented in Table 2.

Table 2. Surface preparation methods used in this study

Method	Steps
1	Rinse in DI H_2O, dry under compressed air
2	Method 1 + O_2 plasma for 1 min
3	Method 1 + O_2 plasma for 3 min
4	Method 1 + O_2 plasma for 5 min
5	Ultrasonic clean in acetone for 10 min + Method 1
6	50 ºC DI H_2O for 5 days
7	RCA-1 clean for 60 min
8	Bombardment by Ar^+ ion beam for 5 min
9	Piranha clean for 30 min

2.1.3 Thermal evaporation

Thermal evaporation (also called thermal deposition) is widely used technique to produce thin film. The advantages of thermal evaporation are stability, reproducibility, and high deposition rate [88]. The thermal evaporation consists in heating until evaporation of the material to be deposited. Typical material heating techniques for thermal evaporation include resistive heating and electron beams.

Resistive heating is the most common technique of heating materials that evaporate below ~ 1500 ºC. The target material is in contact with a hot surface which is heated by passing very high current (>200 A) through a material (resistively heated). Typical resistively heated sources are in the form of wire, boat, crucible etc. (Fig. 16) made from W, Ta, Mo, C, or the BN/TiB_2 electrically conductive composite ceramics [87]. Evaporation takes place in a vacuum, which

allows vapor particles to travel directly to the substrate, where they condense back to a solid state in a form of thin film. When evaporation is performed in poor vacuum ($<10^{-3}$ Pa) or close to atmospheric pressure, the resulting deposition is generally non-uniform as evaporated particles undergo significantly more collisions with the surrounding gas molecules inside the evaporation chamber.

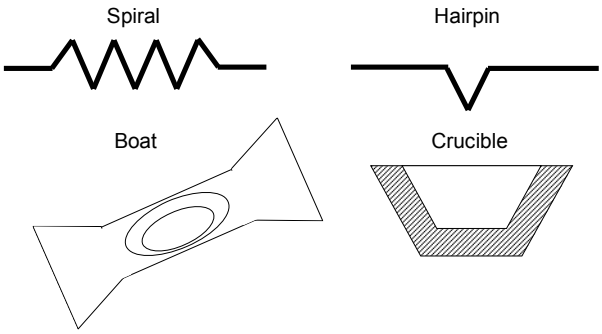

Fig. 16. Resistively heated source configurations

Focused high energy electron beams (e-beams) are commonly used for material evaporation at temperatures above 1500 ºCs. Electron beams can be generated by thermionic emission, field electron emission or the anodic arc method. The generated electron beam is accelerated to a high kinetic energy and directed towards the target material. Upon striking the target material, the kinetic energy of the electrons is converted into other forms of energy through interactions with the target material. The thermal energy that is produced heats up the target material causing it to melt or sublimate [89]. At sufficient temperature and vacuum ($\sim 10^{-3}$ Pa or more) material vapor is produced. The resulting vapor condenses into a solid thin layer of the target material. Electron beam is typically accelerated with voltages from about 5 to 20 kV, to bombard the target material [90]. The target material is placed in crucible container made of titanium, tungsten, molybdenum or graphite. Usually, water cooling is applied to the crucible. The crucible cooling is performed by water circulation. Fig. 17 shows two common sources using e-beam heating [87]. In many designs, the Fig. 17 (right) configuration is used where the filament is kept out of sight of target material in order to avoid chemical interactions and to avoid deposition of target material. A magnetic field is employed to deflect the e-beam from its source to the target material.

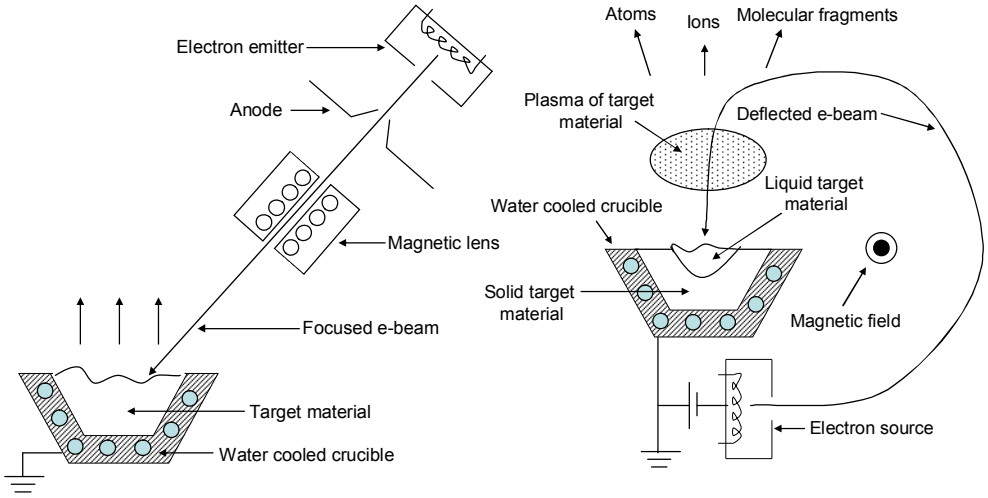

Fig. 17. Electron beam (e-beam) evaporation sources. (left) linear beam source and (right) deflected beam source [87].

2.1.3.1 Thermal evaporation equipment and experimental details

Manually operated thermal evaporation systems UVN-71P3 and Satis CR720CM were used for chromium thin film deposition. In UVN-71P3 system, resistively heated source (boat configuration) was used. Vacuum in the chamber (turbomolecular pump) was 10^{-3} Pa. Approximately 50 mg of chromium granules were placed in the tungsten boat, which was located 100 mm below the substrate. The tungsten boat was heated approximately up to 1656 K (corresponding 1 Pa solid state chromium vapor pressure) using an electric current of 375 A. In Satis CR720CM system, electron beam evaporation source (deflected beam configuration) was used. Base chamber pressure was maintained using a turbomolecular pump and was 1×10^{-3} Pa. Electron beam gun power was 6 kW and chromium granules were used as target material. The deposition rate was 0.5–0.7 nm s^{-1}.

Substrate heating (100 °C) was performed with infrared (IR) lamp heaters installed in the vacuum chambers. The substrate temperature was controlled with "K" type thermocouple probe contacting the substrate. Quartz crystal deposition controllers were also present for thin film thickness monitoring.

2.1.4 Magnetron sputtering

Magnetron sputtering deposition is an alternative PVD process to thermal evaporation to produce thin film. The advantages of magnetron sputtering are proper control on the chemical composition, high deposition rates and low substrate heating during the deposition of the films [91].

In magnetron sputtering process, a target (or cathode) material is bombarded by energetic ions generated in glow discharge plasma, situated in front of the target. The bombardment process causes the removal (sputtering) of target material atoms, which may then condense on a substrate as a thin film. Secondary electrons are also emitted from the target surface as a result of the ion bombardment, and these electrons play an important role in maintaining the plasma [92]. The sputtering gas is often an inert gas such as argon. For efficient momentum transfer, the atomic weight of the sputtering gas should be close to the atomic weight of the target material. For sputtering light elements neon is preferable, while for heavy elements krypton or xenon is used. In magnetron configuration, the magnetic field is located parallel to the target surface, which allows to constrain secondary electron motion close to the target. The magnets are arranged in such a way that one pole is positioned at the central axis of the target and the second pole is formed around the outer edge of the target. The magnetic fields created by such arrangement of magnets trap electrons and increase the probability of ionizing electron–atom collision resulting in the formation of dense plasma in the target region (see Fig. 18) during sputtering process. The magnetron sputtering can be performed at operating pressures as low as 0.1 Pa and voltages of -500 V [92]. The typical substrate ion current density of < 1 mA/cm^2 is generated during conventional magnetron sputtering process. The ion current drawn at the substrate is directly proportional to the target current. The later is directly proportional to deposition rate.

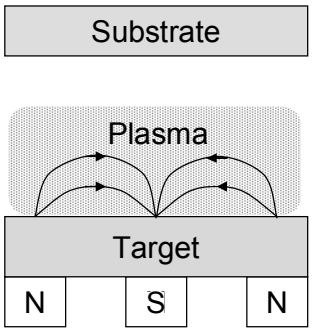

Fig. 18. Schematic of the plasma confinement in magnetron sputtering

Magnetron sputtering can be performed in direct current (DC) or radio frequency (RF) modes. DC magnetron sputtering is mostly used for deposition of conducting materials. If the target material is non-conducting the positive charge will build up on the material and it will stop sputtering. Charge build-up on non-conducting targets can be avoided with the use of RF magnetron sputtering where the sign of the anode-cathode bias is varied at a high rate (usually 13.56 MHz) [93]. Thus, both conducting and non-conducting target materials can be used for thin film deposition.

2.1.4.1 Magnetron sputtering equipment and experimental details

The modified VY-1A (Smorgon) system equipped with RF magnetron was used for sputtering of chromium thin films. Base pressure in the chamber was 1×10^{-4} Pa. A chromium disk was used as a sputtering target. Deposition was carried out at RF input power of 300 W in pure Ar atmosphere. Typical deposition rates of the chromium films were 0.2-0.4 nm s^{-1}. Substrate heating, substrate temperature control and chromium thin film thickness monitoring was performed as in *2.1.3.1* section.

2.1.5 Direct ion beam deposition

Direct ion beam (DIB) deposition uses a broad beam ion source to direct an energetic, chemically active vapor/gas flux for deposition on a substrate. It is mainly used in applications requiring high performance, thin DLC films, particularly in research and development, the tool coating industry, data storage industry and ophthalmic coatings industry. A strong advantage of the ion-beam deposition process is the high degree of control over the thin film properties which results from the largely independent and easy control of critical process parameters such as ion-beam energy, ion-beam current and vapor/gas flow rate. Gridded and gridless ion-beam sources are mainly used for DIB deposition. The later comprises of two main types - end-Hall and closed drift ion sources. Table 3 shows comparison of ion beam sources and some obtainable DLC film properties [94].

The Kaufman-type ion-beam source is the best known example of gridded ion beam source. It provides the most independent control over deposition process parameters over a wide operating range [95]. In this configuration plasma is initiated by applying a voltage (i.e. discharge voltage) between a filament cathode and an anode, adding gas, and heating the filament cathode until it emits thermionic electrons [94]. The electron acceleration to the anode results in gas ionization and plasma formation. The negative voltage applied to the accelerator grid develops a beam by extracting positive ions from the plasma. The ion species formed in plasma are dependant on the vapor/gas flow rate into the ion source and the discharge voltage applied. Ion impact energy and ion-beam current density are controlled by ion beam voltage and accelerator voltage, respectively. Gridded ion-beam sources typically operate at beam currents in the range of 0.2 mA – 1 A and ion energy in the range of 50 eV – 1.5 keV.

The Hall-current ion source operation is based on the physical principles of electron magnetization and on the increase of plasma resistance and electron lifetime, during which electrons can interact with neutral particles and ionize them [96]. Gridless ion-beam source can operate at beam currents up to 10 A. Therefore, very high deposition rates can be achieved (e.g. ~10 nm/s for a-C:H) as compared to gridded ion beam source. Specifically, the magnetic field in a discharge channel of closed drift ion beam source increase from the anode to an ions source exit. The discharge channel has annular form. The electrons are temporarily trapped by the magnetic field created by magnetic coils producing more ionization and increased

plasma density. The ion beam is formed by repelling positive ions from anode. Electrons attracted to the ion beam produce a charge-neutralized beam capable of coating both electrically conducting and insulating substrates [94].

Table 3. Comparison of ion beam sources and some obtainable DLC film properties.

	Gridded ion source	**End Hall ion source**	**Closed drift ion source**
Design characteristics			
Design style	Dual-grid Kaufman	End Hall	Closed drift Hall
Plasma frequency	DC or RF	DC	DC
Electron source for plasma	Hot filament or RF discharge	Hot filament (thick wire; on-axis)	Hollow cathode (on-axis)
Plasma enhancement	Permanent-magnet array	Single permanent magnet	Electromagnet
Ion extraction	Electrostatic via grids	Hall effect	Hall effect
Electron source for ion-beam neutralization	External-filament, hollow-cathode or RF discharge sources	Same as electron source plasma	Same as electron source plasma
Operating characteristics			
Reactive-gas operation	Difficult	Difficult owing to arcing	Excellent
Ion-beam power	High power not possible owing to grids	Spurious arcing at high power	Excellent performance at high power
Contamination	Not an issue if non-filament neutralizer is used	Contamination due to filament and sputter-erosion of reflector plate	Not an issue
Thermal loading of substrate	Not an issue if non-filament neutralizer is used	High thermal load to substrate due to radiation from anode and filament	Not an issue, owing to source cooling and use of hollow-cathode electron source
Control (deposition rate and film properties)	Excellent	Variability due to build-up of insulating coatings	Excellent
Maintenance	Frequent and difficult	Frequent	Infrequent; easy
Obtainable DLC film properties			
Deposition rate	2-10 Å/s	~ 10 Å/s	
Hardness	Up to 40 GPa	Up to 25 GPa	Up to 35 GPa
Thickness uniformity	± 5-10 %	± 5-10 %	± 3-4 %

In contrast, the electrons are only magnetized at the exit part of discharge channel in end-Hall configuration. The magnetic field is created by a single permanent magnet.

The discharge channel has a cylindrical form with a massive hollow conical anode. The cathode, serving as a source of electrons, is usually in the form of a hot filament. The distinctive feature of this ion source is the presence of the cathode neutralizer inside the discharge channel [96]. The discharge current conversion into the ion beam is lower as compared to closed drift ion beam source.

2.1.5.1 Direct ion beam deposition equipment and experimental details

The ion beam deposition system URM 3.279.053 equipped with closed drift ion beam source was used for production of amorphous hydrogenated carbon films. The main parameters of system are given in the Table 4. The Hall-type closed drift ion beam source was used to deposit a-C:H, SiO_x containing a-C:H (a-C:H/SiO_x) and nitrogen doped a-C:H/SiO_x (a-C:H:N/SiO_x) films at room temperature. The base pressure was 2×10^{-4} Pa, work pressure $1 \div 2 \times 10^{-2}$ Pa, and constant ion beam energy of 500 eV was applied with current density of 0.06 mA/cm^2 and 0.08 mA/cm^2 (when combined with PVP). Low energy beam was shown before to yield well defined thin DLC films [57, 97]. The main disadvantage of DLC and ion beam methods is that they lead to films with a large intrinsic compressive stress. This stress causes delamination in thicker films. Therefore, deposition of thin DLC films was chosen for this study [98]. Three precursor gases were used: C_2H_2 for synthesis of a-C:H films; HMDSO with H_2 transport gas for synthesis of a-C:H/SiO_x films; and HMDSO with 20 % N_2/H_2 transport gas mixture for synthesis of a-C:H:N/SiO_x films.

Table 4. Parameters of closed drift ion beam deposition system URM 3.279.053.

Base pressure in chamber: $4 \cdot 10^{-4}$ Pa
Deposition pressure: $(1\text{-}2) \cdot 10^{-2}$ Pa
Accelerating potential of ion-beam source: ≤ 2 kV
Ion beam current density: 0.05 – 0.25 mA/cm^2
Current of solenoid: 6 A
Maximum sample size: 15 cm

2.1.6 Plasma treatment

In the plasma treatment process, a glow discharge plasma is created by evacuating a reaction chamber (partial vacuum) and refilling it with oxygen (O_2), argon, nitrogen, ammonia, fluorine gas and combinations thereof. The gas in the reaction chamber is then energized by RF, microwaves, and alternating (AC) or direct current (DC). The energetic species in gas plasma include free electrons, ions, radicals, metastables and photons in ultraviolet (UV) wave range. Surfaces in contact with the gas are bombarded by these energetic species resulting in energy transfer from plasma to the solid. The energy transfer is dissipated by a variety of

physical and chemical processes which in turn modify the surface of substrate material. The surface can be modified from several nanometers up to ~10 μm in depth. The substrate material modification processes include deposition, etching, oxidation, surface functionalization, crosslinking etc. and are dependant on the substrate material subjected to the plasma treatment, selection of gas or combination of gases, processing time and exposure energies. Plasma treatment is commonly used to clean surfaces from organic contaminants via chemical and physical mechanisms. As a result, non-wettable hydrophobic surfaces are tuned to wettable hydrophilic surfaces [99]. Another application is to selectively alter surface roughness in the plasma environment employing a bombarding effect of ions accelerated towards the surface.

A typical RF powered capacitive plasma chamber configuration schematic is shown in Fig. 19. In this configuration, one electrode is connected to the chamber wall so that the area of one electrode would be larger than that of the other. Increase in the RF power results in increased plasma density and thus a higher ion bombardment energy, and vice versa. The ionized gases are generated at partial pressures in the range of 0.1 - 2 torr. Gas flow can be also varied and is commonly in the range of 100-500 cc/min [100].

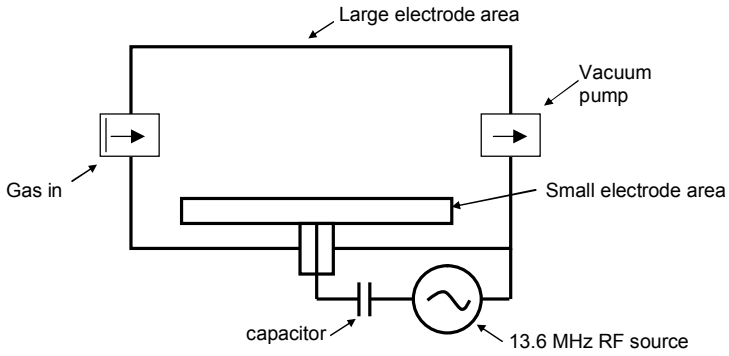

Fig. 19. Schematic of RF powered capacitive plasma chamber configuration

2.1.6.1 Plasma treatment equipment and experimental details

The RF powered capacitive plasma unit Plasma-600T (JSC Kvartz) operating at a frequency of 13.56 MHz and $P = 0.3$ W/cm^2 was used for surface preparation of glass substrates and processing of chromium thin films. The O_2 gas and pressure of 133 Pa was used.

2.1.7 Reactive ion beam etching

Reactive ion beam etching (RIBE) is a process in which the reactive gas is fed into the discharge chamber of the ion beam source. Commonly, the ion sources used are gridded of the Kaufman type (see section 2.3). During RIBE process, the etching species react with the substrate material, its kinetic energy helping to remove volatile etching product. Therefore, the process is partially chemical and partially physical. In contrast to many wet chemical etchants used in wet etching process, the RIBE process etches anisotropically [101] (see Fig. 20 for comparison). Due to this unique ability RIBE is widely used in semiconductor fabrication processes to create a high aspect ratio micro and nano-scale structures. A typical RIBE system consists of a cylindrical vacuum chamber, with a substrate holder and ion beam source. Gas pressure is typically maintained in a range of 2-300 mtorr by adjusting gas flow rates and/or adjusting an exhaust orifice. Gas selection depends on the substrate material to be etched and include Ar, SF_6 Cl_2, O_2 and BCl_3. Etch conditions in an RIBE system strongly depend on the many process parameters, such as pressure, gas flows, and ion beam energy.

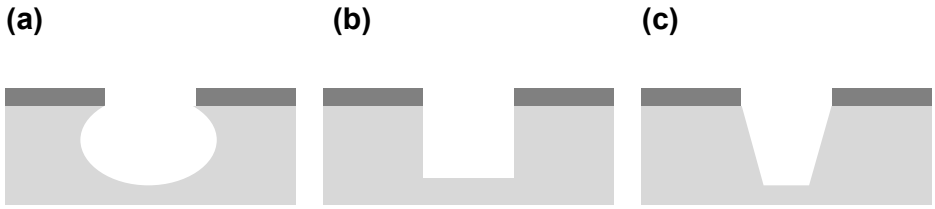

Fig. 20. Characteristic etching profiles of (a) wet isotropic etching, (b) RIBE (anisotropic), and (c) wet anisotropic etching.

2.1.7.1 Reactive ion beam etching equipment and experimental details

The RIBE was performed with the device USI-IONIC. The Ar gas was used in RIBE process. The main parameters of the device are given in the Table 5. The RIBE process was performed for glass substrate surface preparation. The bombardment in RIBE unit was performed by Ar^+ ion beam (etch rate ~40 Å/min) using multi-cell cold hollow-cathode DC ion beam source (Ar^+ ion energy 300 eV, ion beam current 0.25 mA/cm^2, pressure 7×10^{-2} Pa, substrate temperature 293 K ±5 K).

Table 5. The main parameters of the device USI-IONIC.

Base vacuum in the chamber: 5×10^{-4} Pa
Technological pressure in the chamber: $7\times10^{-2} – 4\times10^{-1}$ Pa
Ion beam energy: 0 – 500 keVº
Ion beam current density: 0.01 – 0.30 mA/cm^2

2.1.8 Formation of polymeric interlayer

Polyvinylpyrrolidone films were prepared on the Cr/glass substrates by spin-coating from 5, 10 and 20% PVP dissolved in ethanol (96% vol) using a spin speed of ~2000 rpm for 30 s. Following the coating process, the films were dried in an oven at 50 ^{o}C for 30 min. The films prepared from different concentrations of PVP are denoted as PVP5%, PVP10% and PVP20%, respectively.

2.1.9 Formation of two-step thermally deposited chromium thin films

Chromium thin film having a thickness of 60 nm (or 40 nm) was deposited (resistively heated source) on glass substrates using protocol described in *2.1.3.1* section. Afterwards, the samples were taken out from the vacuum chamber and exposed to O_2 plasma (details can be found in *2.1.6.1* section) for 2 min. Subsequently, a second chromium layer with a thickness of 60 nm (or 40 nm DLC) was deposited.

2.2 Analytical methods and equipment

2.2.1 Contact angle measurements

Wetting phenomena have been studied scientifically during the past 200 years, to one of the many achievements of the British scholar Thomas Young [102]. He suggested a simple equation that equilibrates the forces at the contact point of a liquid drop on a solid surface [103],

$$\gamma_{l,g}\cos\theta = \gamma_{s,g} - \gamma_{s,l}; \quad (1)$$

where γ denote the excess free energy per unit area of the interface indicated by its indices *g*, *l*, and *s* corresponding to the gas, liquid and solid, respectively. The liquid/gas excess free energy $\gamma_{l,g}$ corresponds to the surface tension of the liquid with its vapor. Contact angle θ, which is the other experimentally easily accessible factor in Young's equation. It is the angle, measured through the liquid, where a liquid/gas interface meets a solid surface (Fig. 21). Contact angle (CA) measurements allow general comparisons and can provide a rapid qualitative test for surface wettability characteristics [104]. In general, the lower the contact angle, the higher the surface energy. The increase of energy and decrease of contact angle usually correlates directly with improved adhesion.

Commonly, static contact angle measurement experiments are performed at temperature using the sessile drop method. One droplet of liquid is deposited onto the sample surface and measurements are taken within 10 s after the formation of

sessile droplet. Due to the difficulties encountered to accurately estimate the CA, the static contact angle measurement experiments had a long-standing development. Direct measurement using goniometer on telescope, protractor on pictures are still widely used. The major drawback of these methods are the subjectivity due to the operator action [105]. Therefore, it is often preferred to measure CA angle indirectly by capturing the deposited liquid droplet with high resolution camera and measuring CA using image processing software (e.g. ImageJ). For accurate estimation of CA, the method e.g. B-spline snakes (active contours) is used, which offers the best tradeoff between the use of the general drop shape to guide the detection of the contour of the drop, and the use of an algorithm with local behaviour to compute contact angles with high-accuracy [105].

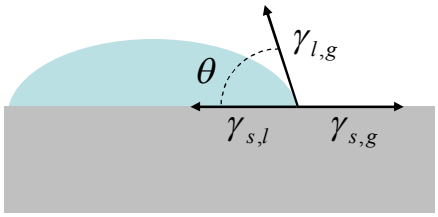

Fig. 21. Schematic of a liquid droplet showing the quantities in Young's equation.

2.2.1.1 Contact angle measurement equipment and experimental details

A portable digital microscope (Kingston) with 2.0 Megapixel image sensor was used for static contact angle measurements. The water droplet images were captured using the software VP-EYE (provided by manufacturer). Contact angle measurements were performed at room temperature (20 °C) by the sessile drop method. One drop of deionized water (5 µl) was deposited onto a dry glass surface. Images of drops were magnified, photographed, and contact angle measured using method based on B-spline snakes (active contours). The method offers the best trade-off between the use of the general drop shape to guide the detection of the contour of the drop, and the use of an algorithm with local behaviour to compute contact angles with high-accuracy [105]. Three measurements were used to evaluate each surface preparation method for air and tin sides of the glass. Each reported value is the mean contact angle of three measurements ± standard error of means. Measurements of contact angles were taken within 10 s after formation of the sessile drop.

2.2.2 Atomic force microscopy

The atomic force microscopy (AFM) is a type of scanning probe microscopy which is used to image the topography and to characterize the morphology of surfaces even at atomic-resolution. It is also used to provide valuable information on

local material properties such as elasticity, hardness, Hamaker constant, adhesion and surface charge densities [106]. The AFM has found a wide range of applications including thin-film technologies, nanotechnologies, micro- and nanotribology, microelectronics, optics, testing systems of the precision mechanics, magnetic recording, vacuum engineering etc.

The AFM uses a cantilever with a sharp tip (probe) at the end as a type of spring to measure the force between the tip and the sample. The local attractive or repulsive force (i.e. molecular force) between the cantilever tip and the sample surface is converted into a bending or deflection of the cantilever. The bending or deflection of the cantilever is detected by a laser beam that is reflected from the cantilever onto a photodetector. The photodetector is usually a photodiode with quadrupole-electrode geometry. The laser spot falls on a different part of the photodetector depending on the position of cantilever. Fig. 22 shows a characteristic AFM system with the main elements indicated [107]. During AFM operation, a piezotube (piezo-scanner) moves a sample in horizontal plane (i.e. XY) under the probe tip from point to point in a manner of raster pattern (see Fig. 23). To drive the piezotube in such pattern, the AFM electronics applies appropriate voltage to segments of the piezotube that causes its bending in a plane parallel to sample surface. In every measurement point, AFM detects the probe position. Electronic system defines change in the probe-to-sample separation and applies corresponding voltage to the piezotube (i.e. Z) to extend or to shorten it to keep the tip-to-surface separation constant, so that the tip moves over a surface at constant distance and repeats its contour. The voltage values on piezotube (i.e. Z) in every measurement point are collected and recorded by the computer software. Afterwards, the collected data is processed and used to display AFM topographical image, surface morphology parameters, or corresponding micromechanical or other characteristics of the sample surface site.

Typically, AFM systems operate in three open-loop modes: non-contact mode, contact mode, and tapping mode. In order to probe electric, magnetic, and/or atomic forces of a selected sample, the non-contact mode is usually utilized by moving the probe slightly away from the sample surface and oscillating the probe at or near its natural resonance frequency [108]. Alternatively, the contact mode acquires sample surface characteristics by monitoring interaction forces while the cantilever tip remains in contact with the sample. The tapping mode of operation combines qualities of both the contact and non-contact modes by acquiring sample data and oscillating the probe at or near its natural resonance frequency while allowing the cantilever tip to impact the target sample for a minimal amount of time [109]. The interaction forces between the tip and sample surface in all three modes can be distinctly identified on a force–distance curve as shown in Fig. 24 [108]. When the interatomic distance is quite large, weak attractive forces are generated between the tip and the sample surface. As the atoms are gradually brought closer to each other the attractive forces increase until the atoms become so close that the electron clouds begin to repel each other electrostatically [108]. The attractive force between atoms becomes smaller due to repulsive force as the interatomic distance is decreased. The interaction force becomes fully repulsive when the atoms are brought in contact.

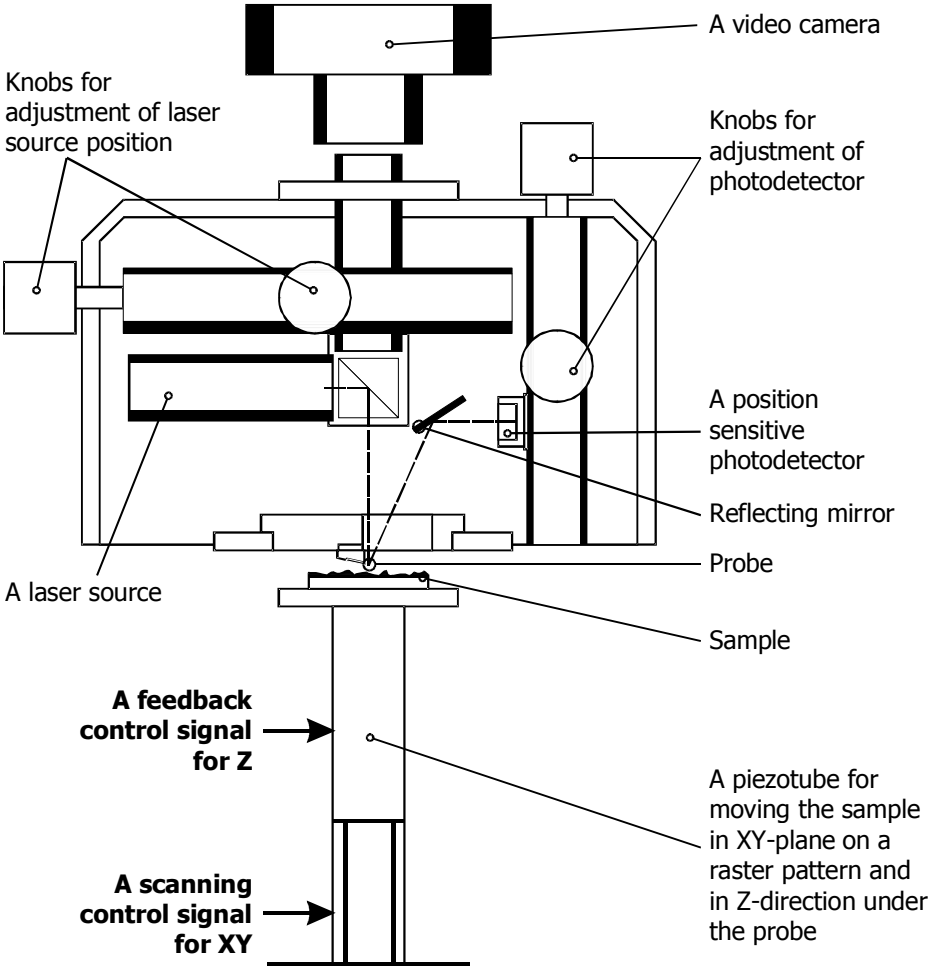

Fig. 22. Schematic of characteristic AFM system with the main elements indicated [107].

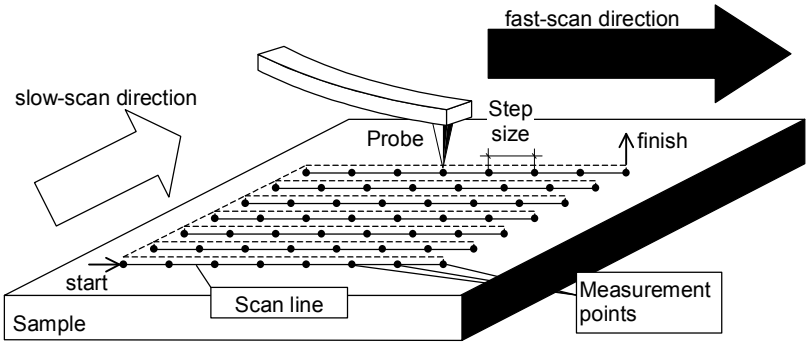

Fig. 23. Schematic of AFM probe motion during the operation [107].

In case the cantilever is retracted from the surface, usually the tip remains in contact with the surface due to the AFM tip-sample adhesion. At some point the force from probe will be enough to overcome the local adhesion resulting in the cantilever tip release. The measured value of this "pull-off" (adhesion) force can be associated with many different types of attraction forces including van der Waals and electrostatic forces. In many cases, the combined magnitude of the forces is affected by the surface topography and depends on factors such as the surface energy characteristics of the tip and the sample [110]. Adhesion mapping images can be constructed from the matrix of points, where in each point AFM tip-sample adhesion was measured. These mapping images are very useful for investigation of heterogeneity of surfaces.

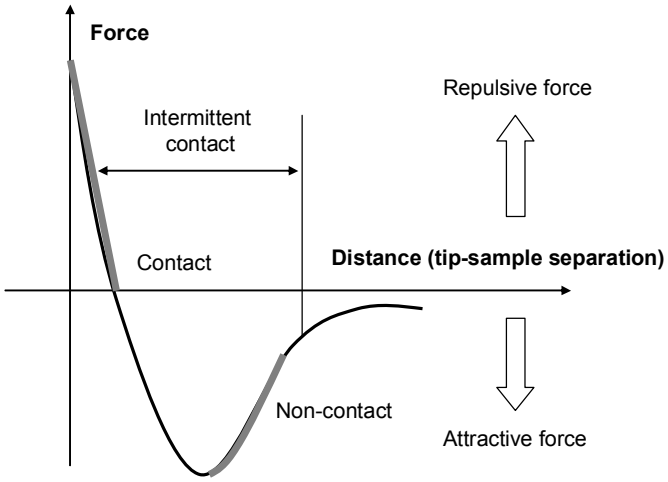

Fig. 24. Schematic of AFM force-distance curve [108].

A detailed evaluation of surface morphology of the thin films is based on the AFM surface topography images, height distribution histograms, bearing ratio curves and roughness parameters, including the root mean square roughness (R_q), skewness (R_{sk}) and kurtosis (R_{ku}). The R_q is the average of the measured height deviations taken within the evaluation area and measured from the mean linear surface. The skewness parameter indicates the symmetry of the surface within the evaluation area. A negative R_{sk} indicates a predominance of valleys while a positive R_{sk} value indicates a surface dominated by peaks. Kurtosis is a measure of the height randomness and sharpness of a surface. For a Gaussian-like surface, R_{ku} it has a value of 3. The farther R_{ku} is from 3, the less random and more repetitive is the surface. These roughness parameters (i.e. R_q, R_{sk}, and R_{ku}) are defined by ISO 4287 standard. The height distribution histogram shows the share of surface points located at a given height relative to the total number of surface points in percent. The bearing ratio curve (i.e. Abbott-Firestone curve) is defined as the dependence of solid material occurrence on feature height. A typical height distribution histogram with bearing ratio curve is depicted in Fig. To obtain more information about surface

morphology, hybrid parameters can be derived by dividing the bearing ratio curve into three regions [111]. The upper region of the bearing ratio curve indicates the portion of surface structures (i.e. peaks), which would primarily be affected during the contact with another surface and is defined as the reduced peak height (R_{pk}). The middle region of the bearing ratio curve indicates the portion of surface structures responsible for stiffness characteristics, performance and life of the surface during wear and is defined as the core-roughness (R_k). The lower region of the bearing ratio curve exhibits surface structures (i.e. valleys) where water molecules adsorbed from the atmosphere could condense or air gabs between contacting surfaces could emerge influencing surface adhesive properties as well as frictional performance and is defined as the reduced valley depth (R_{vk}). These hybrid roughness parameters (i.e. R_{pk}, R_k and R_{vk}) are defined by the standard ISO13565-2.

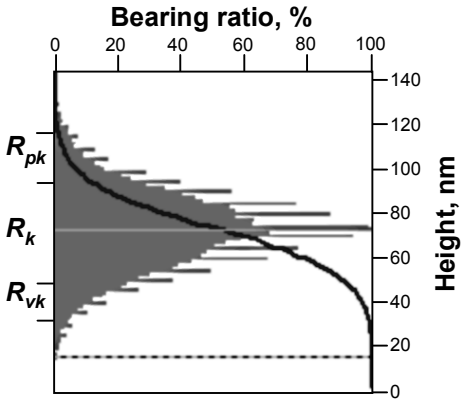

Fig. 25. A typical height distribution histogram with bearing ratio curve. The bearing ratio curve is divided into three regions with hybrid parameters indicated. Dashed line indicates the height at which surface structures are connected to each other. The middle line indicates the mean height.

2.2.2.1 Atomic force microscopy equipment and experimental details

AFM measurements were performed with the device NT-206 (Microtestmachines Co.). Contact mode was used in all measurements. Local surface adhesive forces (i.e. AFM tip-sample adhesion) were calculated from AFM force-distance curves. Granite block having a thickness of 8 cm was used for vibration isolation. The AFM control software was SurfaceScan. The AFM image processing software was SurfaceView / SurfaceXplorer. The main parameters of the device are given in the Table 6.

Table 6. The main parameters of the device NT-206.

Scan field area: up to 50 × 40 μm
Maximum range of measured heights: ~ 2 μm
Lateral resolution (plane XY): 1–5 nm (depending on sample hardness)
Vertical resolution (direction Z): 0.1–0.5 nm (depending on sample hardness)
Scanning matrix: up to 1024×1024 points
Scan rate: 40–250 points/s in X-Y plane
Minimum scanning step: 0.3 nm
Sample size: up to 30×30×8 mm
High voltage amplifier output: ±190 V

AFM experiments were carried out in air at room temperature. Topographical images and force-distance curves were collected using a V-shaped silicon cantilever (spring constant of 3 N/m, tip curvature radius of 10.0 nm and the cone angle of 20º). Adhesion forces were measured by AFM upon detecting the force interaction during approach and retraction of the tip from the sample surface. The point mode was used to set coordinates for generation of the AFM force-distance curve. The adhesion mapping images were generated as follows: the AFM scan range was divided into a matrix with equal distances such that each point had specific coordinates and the adhesion force, F_{ad}, could be extracted from each position. Adhesion mapping images were constructed by displaying the adhesion force values on the AFM topographical images acquired from the same sample area.

2.2.3 Scanning electron microscopy and energy dispersive X-ray spectroscopy

A scanning electron microscope (SEM) is a type of electron microscope that produces images of a sample surface by scanning it with a focused beam of electrons. Typically, e-beam is generated from tungsten filament. Other types of electron emitters include lanthanum hexaboride cathodes. The energy (ranging from 0.2 keV to ~40 keV) of e-beam can be controlled and the beam itself can be manipulated and focused to a spot of ~0.4 nm to 5 nm in diameter using electron optics. The e-beam is scanned in a raster pattern, and the beam's position is combined with the detected signal to produce an image. The interaction of the e-beam with the sample surface results in the interrogation [112] of a certain depth of material below the surface producing secondary electrons, back-scattered electrons, X-rays, light, sample current and transmitted electrons. Secondary electrons are generated in very small depth below the sample surface (several nanometers). They contain information about the sample's surface topography and are collected by secondary electron detectors (most common - Everhart-Thornley [113] configuration) [32]. Secondary electron imaging is a standard mode of operation in all SEM (additionally back-scattered electrons can be imagined). It can produce very high-resolution images of a sample surface, revealing details down to a nanometer. Samples can be observed in high vacuum, in low vacuum, and (in environmental SEM) in wet conditions. Generally in the SEM, specimens must be electrically conductive or at least

electrically grounded to prevent the accumulation of electrostatic charge at the surface. For proper SEM imagining of non-conducting samples, very thin conductive film is usually deposited using PVD method. For biological samples, an additional procedure of critical point drying is performed prior to the thin film deposition. Very often, SEM has an attachment of energy dispersive X-ray spectrometer (EDS) detector. The detector collects X-rays to produce chemical composition of the sample surface. The X-ray generation process initiates with the ejection of an inner shell electron to form a vacancy. From this excited, an upper shell electron drops into the inner shell vacancy. An X-ray is generated with energy equal to the difference between the energies of the electron shell [114] and this energy is unique for different elements. A standard EDS detector contains a crystal that absorbs the energy of incoming X-rays by ionization, yielding free electrons in the crystal that become conductive and produce an electrical charge bias. The X-ray absorption thus converts the energy of individual X-rays into electrical signal of proportional size which corresponds to the characteristic x-rays of the element. Typically, EDS detects elements from boron (5) to americium (95). The EDS detectors are usually cooled with nitrogen.

2.2.3.1 Scanning electron microscopy and energy dispersive X-ray spectroscopy equipment and experimental details

The morphology, approximate composition and the elemental map of the chromium composite film surface, ball scars, wear tracks and wear debris were examined using Hitachi S3400 scanning electron microscope equipped with a Bruker XFlash silicon drift detector (SDD). The main parameters of the device are given in the Table 7. The samples were imaged at the accelerating voltage of 15 kV; no sample coating or any other type of preparation was performed before SEM imaging.

Table 7. The main parameters of Hitachi S3400 SEM.

Resolution with secondary electron imagining: 3.0 nm at 30 kV (High Vacuum Mode); 10nm at 3 kV (High Vacuum Mode).
Resolution with back-scattered electron imagining: 4.0 nm at 30 kV (Low Vacuum Mode).
Magnification: ×5 - ×300,000
Accelerating voltage: 0.3 – 30 kV
Low vacuum range: 6 – 270 Pa
Maximum specimen size: 200 mm in diameter

2.2.4 X-ray photoelectron spectroscopy (XPS) and XPS depth profiling

X-ray photoelectron spectroscopy (XPS) is a surface-sensitive quantitative spectroscopic technique which is based on the photoelectric effect caused by X-ray

photons. In this technique, sample surface is irradiated with X-ray photons, which knock out core electrons from the absorbing atoms. A number of these photoelectrons escape from the top 0-10 nm of the sample being analyzed and their kinetic energy is measured and used to calculate the binding energy for electrons in the core shell of atoms, respectively [115]. XPS binding energy values directly identify each element that exists in/on the surface of the sample material being analyzed. A typical XPS spectrum is a plot of the number of electrons detected versus the binding energy of the electrons detected. In XPS spectrum, different element produces a characteristic set of XPS peaks at characteristic binding energy values. The number of detected electrons in each of the characteristic peaks is directly related to the amount of element within the XPS sampling volume. Thus, XPS spectra can provide quantitative information on elemental composition of the sample surface, a well as chemical or electronic state of each element in the surface. Importantly, X-ray photoelectric effect cannot be observed with hydrogen or helium, but with all other elements present at concentrations grater than 0.1 atomic percent [115]. XPS measurements are performed in high (10^{-8} millibar) or ultra high (10^{-9} millibar) vacuum as electrons travel only short distances in air. In many cases the sample must be electrically grounded to avoid charging because any charge appearing on the sample will affect the kinetic energy of the emitted electron and distort the spectrum [116]. A typical X-ray photoelectron spectrometer consists of an x-ray source and photoelectron energy analyzer. X-ray source is usually a cathode filament, which emits thermal electrons through resistive heating (typical emission current of 30 mA), and an anode to which the electrons are accelerated by appling a high voltage (typically of 9-12 kV). Commercial X-ray sources use Al or Mg as anode material to emit monochromatic or polychromatic Kα X-rays. The energy of an X-ray source with particular wavelength is known (e.g. Mg Kα=1253.6 eV), so the binding energy could be calculated by measuring emitted electrons' kinetic energies. The XPS analyzers can be of either hemispherical [117] or cylindrical-mirror [118] configuration. In hemispherical configuration, two concentric hemispherical electrodes (inner and outer hemispheres) held at proper voltages. It is mainly used for applications where a high resolution is required. In contrast, cylindrical-mirror configuration has two co-axial cylinders which are placed in front of the sample, the inner one being held at a positive potential, while the outer cylinder is held at a negative potential. Thus, only the electrons with the right energy can pass. In this set-up, the signal intensity is high but the resolution is poor. The cylindrical-mirror electron analyzer is often used for checking the elemental composition of the surface.

A depth profile of the sample in terms of XPS quantities can be obtained by combining a sequence of material removal from the sample surface by ion beam interleaved with XPS measurements. Chemical states and elemental composition are likely to be changed by ion beam bombardment, but still a significant amount of information can be obtained. During XPS profiling process, each ion beam etch cycle exposes a new surface of the sample and the XPS spectra provide the means of analyzing the composition of these surfaces. XPS depth profiles are usually presented versus etch time, as the etch rate varies with actual surface composition.

The etch rate can be estimated by depth profiling of thin films of known composition and thickness under the same experimental conditions than the investigated sample [119].

2.2.4.1 X-ray photoelectron spectroscopy (XPS) and XPS depth profiling equipment and experimental details

XPS measurements were performed with Kratos ANALYTICAL XSAM800 and Kratos Axis Ultra DLD spectrometers. The Kratos ANALYTICAL XSAM800 spectrometer was equipped with non-monochromatized Mg Kα radiation at 1253.6 eV and hemispherical energy analyzer. 20 eV pass energy and 0.1 eV energy increment were used in high resolution spectra acquisition. The energy analyzer was operating in fixed transmission mode. No charge neutralization was used. Charge effects were compensated assuming that carbon peak from atmospheric contaminant is located at 284.8 eV. Samples were analyzed after their deposition without any surface cleaning. Relative atomic concentration calculations and peak fitting procedure were performed using original KRATOS DS800 software. The Kratos Axis Ultra DLD spectrometer was equipped with monochromatic radiation at 1486.6 eV from an aluminum Kα source using a 500 mm Rowland circle silicon single crystal monochromator. The X-ray gun was operated using a 15 mA emission current at an accelerating voltage of 15 kV. Low energy electrons were used for charge compensation to neutralize the sample. Depth profiling via high energy ion bombardment was performed using a 5 kV argon-ion beam with an etching rate of 2 nm/min obtained using TaO_2/Ta. Spectra during the depth profiling were acquired in the region of interest using the following experimental parameters: ~50 eV energy window, pass energy of 40 eV, step size of 0.1 eV and dwell time of 500 ms from the 110 μm diameter region. One sweep was used to acquire all regions. The absolute energy scale was calibrated to Cu $2p_{2/3}$ peak binding energy of 932.6 eV using an etched copper plate.

2.2.5 X-ray diffractometry

Crystalline solids exhibit long range structural order, and behave like diffraction gratings for incident light of an appropriate wavelength, ~ 1 Å (X-rays, but also electron and neutron beams) [115]. An X-ray striking an electron of sample's material atom produces secondary spherical waves, which scatter (i.e. elastic scattering) from the electron. Crystalline solid produces a regular array of spherical waves. These waves cancel one another in most directions through destructive interference. However, scattered waves add constructively in a few specific directions, determined by Bragg's law given by the equation:

$$2d \sin \theta = n\lambda \quad (2)$$

, where d is the spacing between diffracting planes, θ is the incident angle, n is any integer, and λ is the wavelength of the beam. If the electron wave scatters are arranged symmetrically with a separation d, the spherical waves will be constructively added only in the directions where their path-length difference $2 \cdot d \cdot \sin\theta$ equals to n multiple of the wavelength λ. In this case, a part of the incoming beam is deflected by an angle 2θ and produces a reflection spot in the diffraction pattern. Thus, after processing the diffraction pattern the XRD measurement can provide information about the crystalline structure, phase content or lack of crystallinity of a sample [115]. XRD measurements can be performed on single crystal, thin films on substrate or powder samples. A typical diffractometer consists of a source of X-ray radiation (typically Cu Kα), a monochromator to choose the wavelength, slits to adjust the shape of the beam, a detector and a goniometer. In typical operation of diffractometer the sample is put on one axis of the diffractometer and tilted by an angle θ while a detector rotates around it on an arm with an angle of 2θ. This configuration is known as Bragg–Brentano 2θ. In another Bragg–Brentano 2θ configuration the sample is stationary while X-ray tube and the detector 2θ are rotated around it. The angle formed between the tube and the detector is 2θ. Commonly, scintillation detectors are used for XRD measurements. They are coupled to an electronic light sensor such as a photomultiplier tube or photodiode, which reemit absorbed light (the one which is deflected by an angle 2θ) by the scintillator in the form of photoelectrons via the photoelectric effect. The multiplication of photoelectrons results in an electrical pulse which is then analyzed. The scintillation detector is optimal for small angles near a direct beam condition and for cases where signal to background is a concern. Another type of detector used in XRD measurements is a one dimensional solid state array detector. It is able to acquire a 4º window at 0.02º resolution and is designed for rapid data acquisition.

2.2.5.1 X-ray diffractometry equipment and experimental details

XRD patterns of chromium thin films were collected using a DRON-6 diffractometer with a Bragg – Brentano geometry in the 2θ range of ~15-90^{o} using Cu-K_{α} radiation. Basic specifications of the device are given in the Table 8.

Table 8. Basic specifications of the DRON-6 diffractometer

X-ray optical scheme: Bragg-Brentano
Range for angles to be scanned, 2θ: - 100 + 165º
Minimum scanning step, 2θ: 0.001º
Accuracy of angle positioning, 2θ and θ: ± 0.005 º
Counting rate: 5×105 imp/s
X-Ray Tube 2,5BSV-27 Cu
NaJ(Tl) Scintillation Detector

2.2.6 Laser ellipsometry

Ellipsometry is an optical measurement technique that characterizes light reflection (or transmission) from samples [120]. It provides contact free determination of thickness and optical constants (e.g. refractive index). Furthermore, it can be used to characterize composition, roughness, doping concentration, crystalline nature and other material properties. The principle of ellipsometry is to measure the change in polarized light upon reflection on a sample (or light transmission by a sample). Usually, ellipsometry measurement is done in the reflection setup. Thin films having a thickness less than a nanometer to several micrometers can be measured. Two types of ellipsometry configurations can be employed. Single-wavelength (i.e. laser ellipsometry) employs a monochromatic light source, e.g. HeNe laser operating in a visible spectral region with a wavelength of 632.8 nm. In spectroscopic ellipsometry, spectra are measured by changing the wavelength of light in a certain spectral range in the infrared, visible or ultraviolet spectral region [120]. A typical ellipsometer consists of a light source, two polarizers and a detector (typically Si photodiode). In ellipsometer operation, electromagnetic radiation is emitted by a light source and linearly polarized by a polarizer. Afterwards, it falls onto the sample and may be decomposed into *s* and *p* component. The *s* component is oscillating perpendicular to the plane of incidence and parallel to the sample surface, and the *p* component is oscillating parallel to the plane of incidence. After reflection the radiation passes a second polarizer (i.e. analyzer) and falls into the detector. The amplitudes of the *s* and *p* components, after reflection are normalized to their initial value. Finally, the ratio (or difference) of these two values is measured. In this configuration, the angle of incidence of emitted radiation equals the angle of reflection.

2.2.6.1 Laser ellipsometry equipment and experimental details

The determination of film thickness and refractive index was performed using laser ellipsometer Gaertner L-115 (Gaertner Scientific Corporation, USA) operating in a visible spectral region with a wavelength of 632.8 nm (HeNe laser). The main parameters of the device are given in the Table 9. Measurements were done at constant incidence angle of 50º. The calculations were done automatically with software LGEMP (provided by manufacturer). Control tests using monocrystalline Si(100) (UniversityWafer, Inc.) samples (a-C:H/SiO_x/Si(100), a-C:H:N/SiO_x/Si(100) and PVP/Si(100)) were conducted to estimate the refractive indices of a-C:H/SiO_x, a-C:H:N/SiO_x and PVP as well as to determine thickness of DLC films for estimation of deposition rates. The uncertainty of measurements for thickness was ± 0.5-1 nm. The uncertainty of measurements for refractive index determination was ±0.01. Corresponding refractive indices of 1.88, 1.85 and 1.52 were determined for a-C:H/SiO_x, a-C:H:N/SiO_x and PVP, respectively.

Table 9. The main parameters of laser ellipsometer Gaertner L-115

Sample size range: 50mm - 6"/150 mm
Angles of incidence: pre-aligned; selectable at 30º, 50º and 70º
Laser beam diameter: 1×3 mm on sample at 70º; 1×1.6mm on sample at 50º; 1×1.2 mm on sample at 30º.
Film Thickness Range: 0-60,000 Å
Thickness measurement accuracy: ± 3 Å over most of the measurement range.
Refractive index measurement accuracy: ± 0.005 over most of the measurement range.
Scanning Increments: 0.01º rotation (0-360º); 0.01mm translation (0-100 mm).

2.2.7 Fourier transform infrared spectroscopy

Molecular vibrations can range from the simple coupled motion of the two atoms of diatomic molecule to complex motion of each atom in a large polyfuctional molecule [121]. Infrared spectroscopy relies on the basis that the energy difference for transitions between the ground state and the first exited state of most vibrational modes (i.e. fundamental vibrations and associated rotational-vibrational structure) corresponds to the energy of radiation in the mid-infrared spectral wavelength region of 400 to 4000 cm^{-1} (mid-infrared region). Additionally, near-IR region having spectral wavelength region in the range of 14000–4000 cm^{-1} can excite overtone or harmonic vibrations. The far-infrared, approximately 400–10 cm^{-1} can be used for rotational spectroscopy. For many vibrational modes, only a few atoms have large displacements and the rest of the molecule is almost stationary. Therefore, the observation of spectral features in a certain region of the spectrum is often indicative of a specific chemical functional group in the molecule [121]. In practical infrared (IR) spectroscopy, the spectrum of sample is obtained by passing or reflecting a beam of IR light through/form the sample. When the frequency of the IR is the same as the vibrational frequency of the specific chemical functional group, absorption occurs. In standard IR spectrometer, this is achieved by separating individual frequencies of energy emitted from the IR source via the use of monochromator (i.e. a prism or grating). After passing or reflecting through/form the sample, the amount of energy at each frequency is measured by a detector (e.g. DLaTGS) and the results represented by a spectrum. In this configuration, typical survey scans take several minutes to measure. The measurement of quality spectra (1-2 cm^{-1} resolution) takes ~30 min. In contrast, all wavelength range is measured at once (i.e. Fellgett's advantage) in Fourier transform infrared (FTIR) spectrometer. It results in a higher Signal-to-noise ratio for a given scan-time or a shorter scan-time for a given resolution. Additionally, more radiation can be passed between the source and detector for each resolution element (i.e. Jacquinot's advantage) [121]. This advantage arises from the fact that Michelson interferometer is adapted for FTIR. Thus, interferometer throughput is determined only by the diameter of the collimated beam coming from the source. In FTIR spectrometer operation the light is emitted from infrared source, refracted towards the fixed mirror (ideally 50 %) and is transmitted towards the moving mirror (ideally 50 %). Afterwards, light is

reflected from the two mirrors back to the beam splitter, passed (ideally 50%) to sample compartment and focused into the sample. Further, light is transmitted or reflected through / from the sample and refocused on to the detector. An FTIR spectrum is obtained by varying the retardation (i.e. difference in optical path length between the two arms to the interferometer) and collecting the signal from the detector for various values of the retardation. The spectrum of absorption, transmission, reflection, emission, photoconductivity or Raman scattering of a sample can be obtained using FTIR spectroscopy.

2.2.7.1 Fourier transform infrared spectroscopy equipment and experimental details

FTIR measurements were carried out to study the blend behavior of PVP upon a-C:H/SiO_x and a-C:H:N/SiO_x direct ion beam deposition. A Vertex 70 FT-IR spectrometer (Bruker Optics Inc.) equipped with a 30Spec (Pike Technologies) specular reflectance accessory having a fixed 30^o degree angle of incidence (3/16" sampling area mask) was used in this study. For each spectrum, the average of 100 successive scans over the range of 400-4000 cm^{-1} at a resolution of 4 cm^{-1} were recorded. Software OPUS 6.0 (Bruker Optics Inc.) was used for data processing of the baseline-corrected spectra. The main specifications of the device are given in the Table 5.

Table 10. The main specifications of Vertex 70 FTIR spectrometer.

Light sources: for visible/near-IR a tungsten halogen lamp; for mid-IR HeNe (632.8 nm).
Detector: DLaTGS covers range from 12000 to 250 cm^{-1}, sensitivity dose >4×108 $cm \cdot Hz^{1/2} \cdot W^{-1}$,
Beam splitter: KBr, covers spectral range from 7500 to 370 cm^{-1}
Sample compartment window: KBr
Measuring configurations: Transmittance, 30º reflectance, variable angle reflectance, attenuated total reflectance, diffuse reflectance
Operating conditions: temperature in the range of 18-35 ºC with humidity ≤ 80 %

2.2.8 Ultraviolet–visible spectroscopy

Ultraviolet-visible (UV/Vis) spectroscopy is used to examine electronic transitions associated with absorptions in the UV (wavelength range 200-400 nm) and visible (400-800 nm) regions of the electromagnetic spectrum. The energies associated with these regions are capable of promoting outer electrons of a molecule from one electronic energy state to a higher level [122]. The more easily excited the electrons, the longer the wavelength of light it can absorb. UV/Vis spectroscopy can be used for the quantitative determination of transition metal ions, highly conjugated organic compounds, and biological macromolecules. It is particularly suitable for the

observation of chemically excited states of hydrocarbons [123]. Further, it can be used for structural evaluation of nanoparticles (e.g. estimation of gold nanoparticles size) [124] and thickness determination of transparent films and layers [125]. Samples can be liquid solutions, solids and gases. A typical UV/Vis spectrophotometer measures the intensity of light passing through a sample (I), and compares it to the intensity of light before it passes through the sample (I_0). The ratio I/I_0 is called the transmittance, and is usually expressed as a percentage ($\%T$). The absorbance, A, is based on the transmittance (i.e. $-\log(\%T/100\%)$). Another configuration of the spectrophotometer is to measure reflectance. In this case, the intensity (I) of reflected light from a sample is measured and compared to the intensity of light reflected from reference material (I) (specular reflectance standard). Here, the ratio I/I_0 is called reflectance ($\%R$). A typical UV/Vis spectrophotometer consists of a light source (i.e. tungsten filament or light emitting diode), a sample holder, a monochromator (with a diffraction grating or prism), and a detector (i.e. photomultiplier tube, photodiode or charge-coupled device). During the measurement operation the monochromator moves the diffraction grating in a step-wise manner for each wavelength so the intensity is measured as a function of wavelength. If the detector is a charge-coupled device the light of different wavelengths is collected simultaneously.

2.2.8.1 Ultraviolet–visible spectroscopy equipment and experimental details

The UV/Vis measurements were performed using a USB4000 UV/Vis Spectrophotometer equipped with a deuterium tungsten lamp and SpectraSuite software. The main specifications of the device are given in the Table 11. For the reflection measurements, an R-series fiber optic reflection probe (R400-7-UV/VIS) and holder were utilized. The probe was held at a 90º angle from the surface. The distance from the tip of the reflection probe to the sample surface was ~3 mm. The AVANTES RS-2 specular reflectance standard with Al+MgF_2, (250-1100 nm wavelength range) was used as the background for all reflection measurements. The thicknesses of DLC-PVP composite films were determined using the interference effect of light and calculated using Eq. 1 [126],

$$d = \frac{w}{2\sqrt{\eta^2 - \sin^2\theta}} \cdot \frac{\lambda_1 \cdot \lambda_2}{\lambda_2 - \lambda_1} \cdot \frac{1}{1000} \tag{3}$$

where d is the film thickness (μm), w is the number of complete waves over the wavelength range, η is the refractive index of the film material and θ is the angle of incidence. Also in Eq. 1, λ_1 and λ_2 represent the short and long wavelength limit, respectively, for wave counting.

Table 11. The main specifications of USB4000 UV/Vis spectrophotometer.

Detector: Toshiba TCD1304AP Linear CCD array
Detector wavelength range: 200-1100 nm
Spectroscopic wavelength range: 200-850 nm
Optical resolution: ~1.5 nm full width at half maximum
Signal-to-noise ratio: 300:1 (at full signal)
Sensitivity: 130 photons/count at 400 nm; 60 photons/count at 600 nm
Integration time: 3.8ms - 10 seconds

2.2.9 Scratch test

The scratch test is a method used for characterizing the surface mechanical properties of thin films and coatings. It has found application in many different fields of materials research [127]. In the scratch test, as schematically shown in Fig. 26, scratch is generated using a diamond stylus/indenter (typically a Rockwell C profile), which is drawn across the sample under constant or progressively increasing load [128].

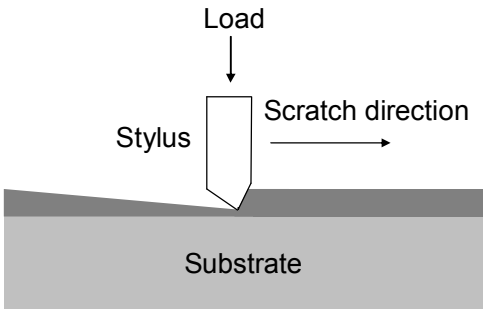

Fig. 26. Schematic of the scratch test [128].

For progressive loading, the critical load is defined as the smallest load at which a recognizable failure occurs. For constant loading, the critical load corresponds to the load at which a regular occurrence of such failure along the scratch track is observed. During the scratch test, elastic and/or plastic deformations occur at specific critical loads along the scratch track. The critical loads are detected by optical microscopy or by variations in acoustic emission and frictional force [128]. The critical load data is used to quantify the adhesive properties (related to detachment at the film-substrate interface) of different film-substrate combinations; and cohesive properties (related to the first failure) within the film. Generally, adhesion is defined as the effect of forces of attraction at the interface of two different solid phases. In contrast, cohesion is the effect of forces of attraction within the same phase (e.g. in the thin solid film) [129]. The driving forces for the failure of the film-substrate system in the scratch test are a combination of elastic-plastic, frictional stresses and the residual internal stress present in the thin film [128]. In the lower load regime, these

stresses generally result in tensile or conformal cracking of the film (i.e. cohesive failure). The onset of these phenomena defines a first critical load. In the higher load regime, the detachment of film from the substrate by spalling, buckling or chipping defines another critical load (i.e. adhesive failure). A commercial scratch tester (see Fig. 27) typically consists of indenter/stylus mounted on cantilever, a motorized friction table, a displacement actuator and displacement sensors.

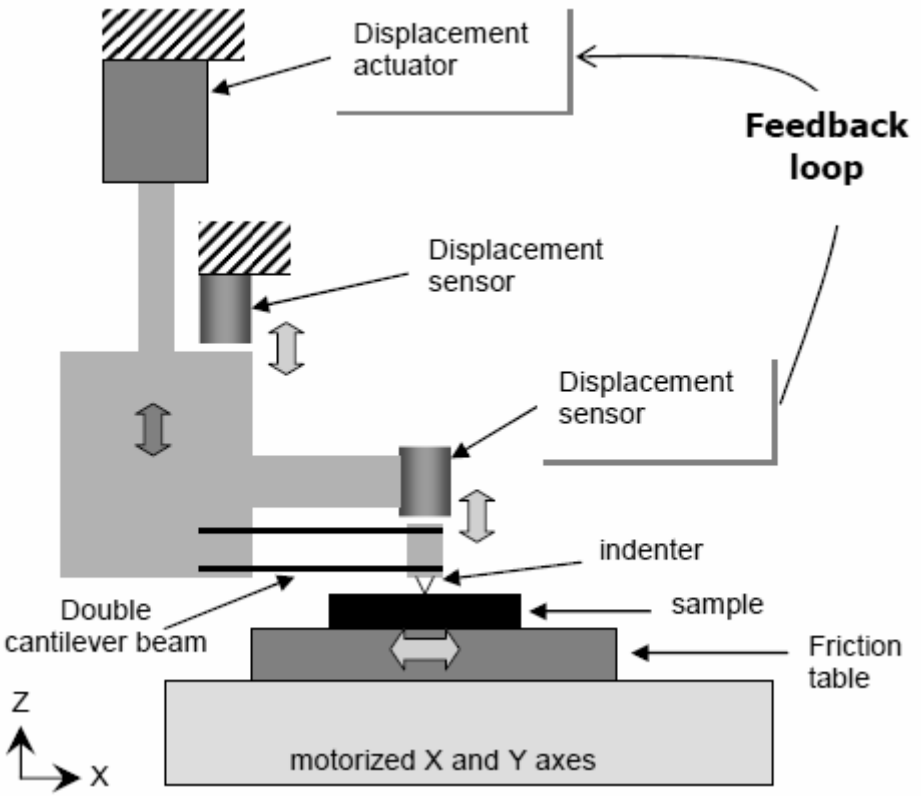

Fig. 27. Schematic of fundamental components in scratch tester [130].

The feedback loop control provides an advantage that the force applied on the sample is not affected by the surface topography. Modern scratch testers measure the acoustic emission, the applied normal force, the tangential (i.e. frictional) force, the penetration depth and residual depth. These parameters provide the mechanical signature of the film-substrate system. The pre-scan (provides a profile of the proposed scratch path) and post-scan (provides a profile of the residual scratch path) procedures are used to measure real penetration depth during the scratch and residual depth (elastic recovery) of the film after the scratch. The penetration depth corresponds to the depth measured during the scratch minus the depth measured in the pre-scan. The residual depth is the difference between the depth measured during the post-scan and the pre-scan. The scratch test appears the best technique for most

situations for the case of hard and brittle films. For soft films, through this test is difficult to extract a true delamination mode (i.e. film detachment) from, it is still useful as a complementary test of other techniques [130].

2.2.9.1 Scratch test equipment and experimental details

Firstly, the adherence of thin chromium films was measured with custom-made PC controlled scratch testing apparatus. Main specifications are given in Table 12. During the scratch test the glass slides with deposited chromium thin film on top were scratched with an indenter applying the progressive load (normal force). The displacement of the indenter, normal force and the occurring tangential (frictional) force were recorded. The abrupt change in tangential force pinpoints the spot on a scratch track where the chromium film gets detached from the float glass substrate, i. e. at the critical normal force [131]. The chromium thin film adhesion to float glass treated under different surface preparation methods were evaluated by comparing critical normal forces of film delamination. Five scratches were performed on each glass slide with chromium thin film and average values of critical force were calculated. Either two or three critical loads were determined for each slide by optical microscopy inspection. The principal scheme of acting forces and force moments of custom-made PC controlled scratch testing apparatus is presented in [132]. In other experiments, the adherence of chromium, chromium composite and DLC films was measured with CSM Nano Scratch Tester. Main specifications are given in Table 12. During the scratch test the the samples were scratched (scratch length 2 mm and speed 4 mm/min) with an sphero-conical stylus (cone angle 90° and indenter radius 5 μm) applying the progressive loading (initial load 3 mN and final load 300 mN) at a fixed rate (loading rate 594 mN/min). The scratches were performed in air atmosphere (temperature 23ºC and humidity 40%). The displacement of the indenter, normal force and the occurring tangential (frictional) force were recorded. Optical microscopy inspection was used to detect coating failure after scratching and differentiate between cohesive failure within the coating and adhesive failure at the interface of the Cr/glass, Cr-composite/glass and DLC/Cr systems. The cohesive and adhesive properties of the chromium, chromium composite and DLC films were evaluated by comparing critical load (L_{c1}), e.g. the load at which the first crack or failure appears on the film and another critical load (L_{c2}), the load at which the full delamination of the film occurs [128]. Three scratches were performed for each sample and mean values of L_{c1} and L_{c2} were calculated.

Table 12. The main specifications of custom-made scratch testing apparatus and Nano Scratch Tester

Custom-made scratch testing apparatus				
	Normal load		Frictional load	
I mode	0.340±0.009 N		0.070±0.002 N	
II mode	3.50±0.07 N		0.180±0.005 N	
III mode	5.40±0.12 N		2.30±0.05 N	
Minimal length of the scratch sample: 15 mm				
Nano Scratch Tester				
Normal load		Standard mode (ST)	High load mode (HL)	High resolution mode (HR)
	Max load:	100 mN	1 N	10 mN
	Resolution:	1.5 μN	15 μN	0.15 μN
Frictional load	Range:	0.2 – 1 N		
	Resolution:	0.3 – 6 μN		
	Range		Repeatability	
X and Y Stages :	X : 120 mm Y : 20 mm		1 μm 1 μm	
Scratch Speed :	From 0.4 to 600 mm/min			
Loading rate :	up to 10 N/min (for ST), up to 1 N/min (for HR), up to 100 N/min (for HL)			

2.2.10 Tribometry

Tribometry is a method used to measure the lifetime of a film and to study its friction and wear behavior. The test itself is called pin-on-disk/ball-on-disk test. Fig. 28 shows a schematic of main components in a typical tribometer [133]. The sample is mounted on a chuck which can be rotated at a predetermined speed. A ball or pin is mounted on a stiff lever, designed as a frictionless force transducer. The elastic arm can move laterally and thus measure the frictional force (i.e. tangential forces) between sample and pin or ball with a sensor. The frictional force is collected as a function of time or number of revolutions. In many cases it is recalculated to display the coefficient of friction on the same axes. A significant change in coefficient of friction corresponds to the ball/pin wearing the film and thus gives a measure of the lifetime of the film. After the test the war rate of the sample can be calculated by several methods. In the first method, the profile across the wear track is measured and sectional area of material which was worn out calculated. Afterwards, it is multiplied by the wear track circumference and wear rate expressed in $mm^3/N/m$. In the second method, the sample is weighted before and after the pin-on-disk/ball-on-disk test with a precision weighing-machine and the material which was worn out is found. The parameters of typical commercial tribometer such as speed, contact pressure, time and the environmental parameters (temperature, humidity and lubricant) can be controlled to allow simulation of real life conditions of a practical wear situation. Most of commercial tribometers can perform rotation of the sample and/or linear reciprocating movement of the sample [133].

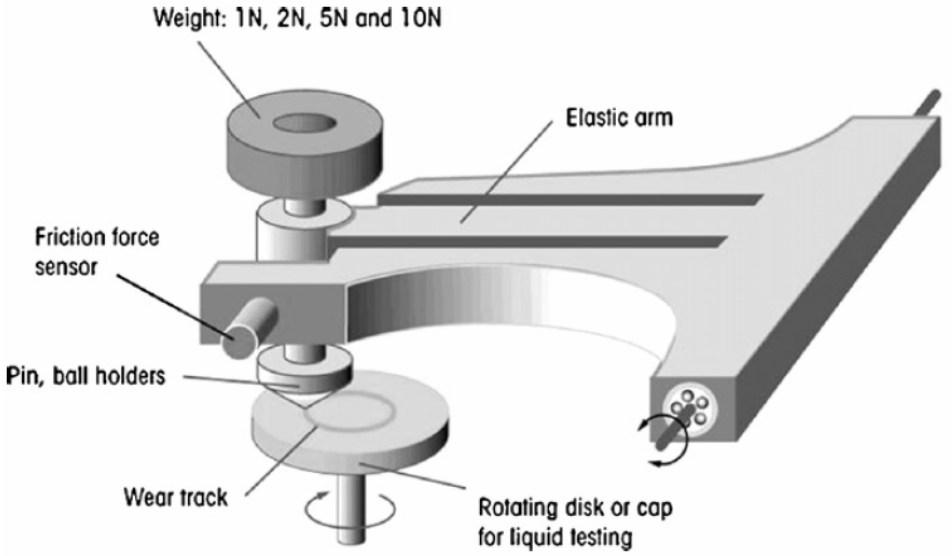

Fig. 28. Schematic of main components in tribometer (pin-on-disk configuration) [133].

2.2.10.1 Tribometry equipment and experimental details

Sliding tests (i.e. ball-on-disk tests) were carried out using a High Temperature Tribometer (CSM Instruments). The main specifications of the tribometer are given in the Table 13. Balls of 100Cr6 and 440C bearing steel with a diameter of 6 mm were used as the counter-parts. These two types of balls are used extensively in bearing applications so the tribological properties of chromium films at room temperature were tested with both. The tests were carried out at temperatures ranging from 20 to 200 ºC. The heating time was about 2 h for the experiments performed in the temperature range of 100 ºC to 200 ºC, while the cooling time was 3 h for 200 °C experiments. Prior to the ball-on-disc measurement, the counter-part was heated to the temperature of the sample. All measurements were provided with a load of 1 N and a linear speed of 0.1 m/s; the relative humidity of air was kept constant at 46 ± 5%. The radius of a wear test track varied from 3 to 6 mm. The number of cycles was 1000 for sliding with both 100Cr6 and 440C balls.

The height of the worn part was determined by measuring the section of the wear track edge using the AFM by collecting the wear track edge profiles. The average value of five deepest (i.e. darkest sections in the optical image) edge profiles measured in each wear track was used to calculate the height of the worn part. The optical images of wear tracks were converted to greyscale with brightness and contrast levels equalized for each image, respectively. The optical images of the wear tracks were reconstructed to 3D topographical images by assigning the height of the worn part and interpreting the luminance of each pixel in the optical image as the height. The width of the wear track was determined by measuring the profile of

the constructed wear track topography. Further, height distribution histograms and bearing ratio curves were derived and mean height was determined. The wear rates of the films were calculated as the worn material volume per sliding distance and normal load.

Table 13. The main specifications of High Temperature Tribometer.

Maximum temperature: 800 °C
Maximum load 10 N/friction coefficient (i.e. higher for low-friction contacts)
Counterparts: balls (diameter 2-15 mm) - alumina, silicon nitride, 100Cr6 and 440C steel
Maximum sample dimension: 55 mm in diameter
Motor speed: up to 1500 rpm

3. EXPERIMENTAL RESULTS AND DISCUSSION

3.1 Surface preparation of glass substrate and properties of chromium thin films

3.1.1 Influence of substrate surface preparation on wetting properties of the surface

Surface preparation methods that effectively remove debris, possible reaction products and organic contaminants produce hydrophilic surface with low water contact angles. Conversely, methods which incompletely remove organic contaminants will leave a more hydrophobic surface with higher contact angles. It was observed in [134] and [135] that glass water contact angles change in the range of 34° – 36.5°. In Ref. [104] it was shown that after application of the RCA-1 clean the glass surface wettability was increased, displaying low contact angle of 2°. The piranha clean treatments on glass resulted in highly variable contact angles ranging from 8° – 43°, 4° and 21° – 27° as it was reported in Ref. [104], [136] and [137], respectively. Glass treatment with oxygen plasma resulted in contact angles below 10° as it was reported in [138].

Wetting properties of glass after different surface preparation methods were examined. Fig. 29 presents mean contact angles of air and tin sides of float glass after different surface preparation methods (see section *2.1.2*). As shown in Fig. 29, the contact angles obtained by reference method were by ~10° lower comparing to as-obtained glass in [134] and [135]. Methods 2 – 4 and 7 revealed the best results, where surfaces were free of hydrophobic contaminants with low contact angles ranging from 4° to 8°. Here, the organic contamination possibly resulted to be not greater than several percent of a monomolecular layer in coverage and contact angles were close to surface total wettability. Comparing with control method (Method 1) it is assumed that oxygen plasma treatment (Methods 2 – 4) activated

glass surface causing the decrease of contact angle from 20° ±2° to ~6° due substitution of chemically active dangling bonds and hydroxyl groups for the carbon contamination in the surface resulting in reduced oxidation as it was reported in [138]. It is considered, that the Method 7 also retains hydroxyl groups on the glass surface, imparting negative charge to the surface (making it hydrophilic) [83]. The contact angles obtained by Methods 2 – 4 and 7 are close to those reported in the literature.

Surface activation and contamination removal by O_2 plasma process requires the investment in proper equipment. It has the advantage of being able to clean considerably more glass slides at the same time with little or no waste products requiring less operator input than wet chemical cleaning procedures and is more suitable for industrial applications. The alternative RCA-1 surface preparation method gives practically the same soda-lime-silica float glass surface wettability properties as plasma treatment and is being easy to set up, requiring the basic chemicals and the use of a fume hood. However, it generates toxic waste products and is more suited in small research laboratories.

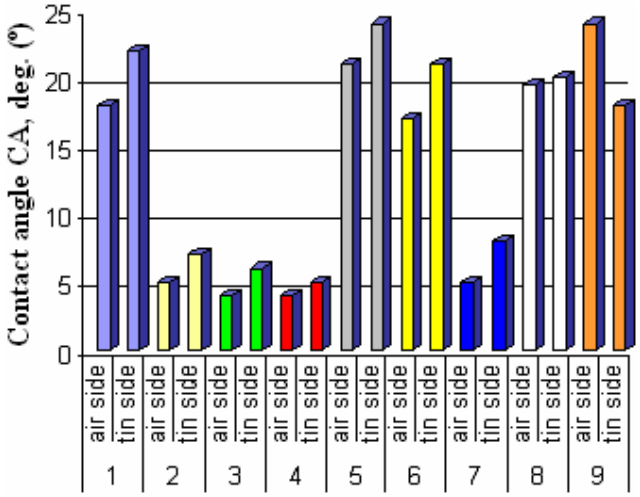

Fig. 29. Mean contact angles of air and tin sides of soda–lime–silica float glass after different surface preparation methods. Each bar represents the mean of three measurements per sample. The standard error of the mean for all contact angles ± 1º.

For Methods 1 – 7 the contact angles were observed slightly higher for the tin side of float glass. The previous work results [139] suggest that the tin side of soda-lime-silica float glass has higher OH group density than the air side resulting in more intense adsorption of organic substances in the atmosphere, and thus governing the wettability of the float glass surface. In order to clarify these results the Method 8 was used. As a result, the contact angles for tin and air sides of float glass were obtained basically equal (Fig. 29). Thus, from [139] it is considered that Sn present monolayers of tin side were etched during bombardment in reactive ion beam etching (RIBE) unit by Ar^+ ion beam thus equalizing glass surface wettability properties of both sides. The contact angles obtained using Method 8 were nearly the

same as reported in [137]. The Piranha clean of Method 9 resulted in opposite reaction, as shown in Fig. 29. It is considered that surface heterogeneity caused by the leaching and/or etching actions of the cleaning agent differently affected float glass surface wettability properties as compared with Methods 1 – 7. The contact angles obtained were rather similar with results obtained in [137] than with [136]. Also, it is considered that the leaching actions of Method 6 and ultrasonic clean in acetone (Method 5) did not noticeably altered soda-lime-silica float glass wettability properties.

3.1.2 Influence of substrate surface preparation and thermal pretreatment on the adhesion strength of chromium thin film to substrate

In the present study, chromium thin film deposition was performed using a thermal evaporation technique employing a resistively heated source (see section *2.1.3.1*). Chromium thin films were deposited on tin and air side of float glass, prepared using different surface preparation methods (see section *2.1.2*). The thickness of chromium thin film was 40 nm. In Fig. 30, the applied normal load and resulting tangential force are displayed as a function of displacement for Cr/glass slides, where soda-lime-silica float glass surface was prepared using Method 1, 4 and 7. In all plots, the first part shows a linear behavior of the tangential force with respect to the applied load. The change in tangential force is detected at the critical normal force where coating failure occurs. For glass slides prepared under Method 1, the average critical normal force had value of 0.087 N, whereas it had value of 0.169 N and 0.14 N for Method 4 and 7, respectively. It can be seen that critical normal force decreases with increasing contact angle (Fig. 29). Slight variations of critical normal force were observed in all measurements for tin and air sides of float glass. The highest average critical normal force was observed for Cr/glass slides, where soda-lime-silica float glass surface was prepared using Method 2 – 4 and 7. It follows that O_2 plasma process and RCA-1 surface preparation method for float glass results in less contaminated surfaces and a higher value of the thin chromium film adhesion to the float glass substrate as measured from the critical normal force by scratch tests. The summary of the scratch test results is presented in Fig. 31.

The optical analysis at the positions at which the change in tangential force was observed showed the characteristic images of chromium thin film delamination (see Fig. 32 for characteristic image of full delamination).

Another series of float glass substrates prepared using O_2 plasma process and RCA-1 clean were subjected to thermal treatment (100 °C) in the vacuum chamber before chromium thin film evaporation process. The scratch tests revealed no change in tangential force over all range of scratch track. It can be concluded that the average critical normal force for coating delamination for these samples exceeded a value of 0.2 N. This was also confirmed by optical analysis of the produced scratch tracks. No stripping or coating failure was observed.

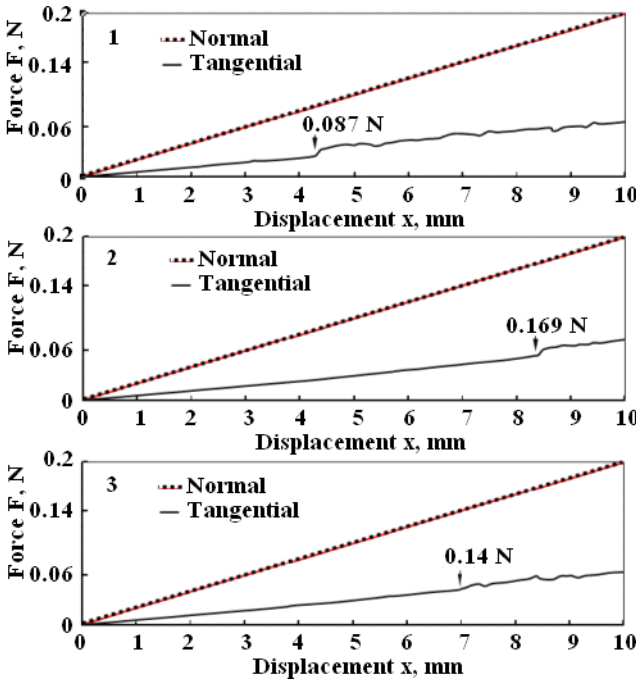

Fig. 30. Tangential and normal force as a function of displacement. (1) Cr/glass slide, where float glass surface was prepared using Method 1, critical normal force value of 0.087 N. (2) Cr/glass slide, where float glass surface was prepared using Method 4, critical normal force value of 0.169 N. (3) Cr/glass slide, where float glass surface was prepared using Method 7, critical normal force value of 0.14 N

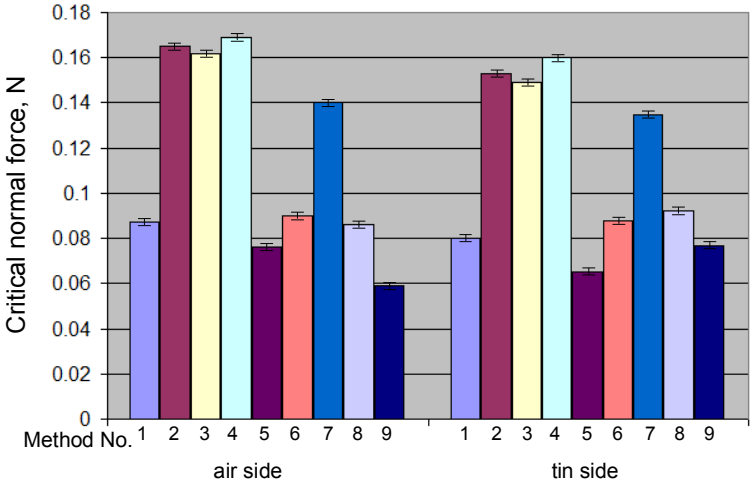

Fig. 31. Summary of the scratch test results. Critical normal force required to delaminate chromium thin film from glass, where soda-lime-silica float glass surface (air side and tin side) was prepared using different surface preparation methods.

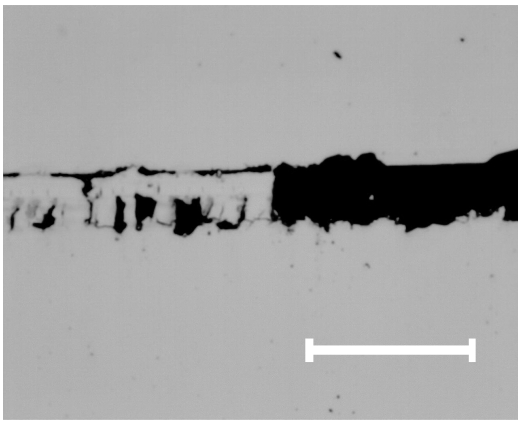

Fig. 32. Characteristic optical image of the scratch track section where the full delamination of the chromium thin film occurs. Similar fracture was observed on the other samples. Mark size 10 µm.

3.1.3 Surface morphology of substrate prepared using RCA-1 clean

AFM 3D topographical image of characteristic glass substrate surface prepared using RCA-1 clean is shown in Fig. 33a. Surface topography shows a random distribution of small peaks having mean height and base diameter of 2.07 nm and ~130-180 nm. Surface RMS roughness, R_q as low as 0.91 nm was observed in AFM scans. Surface skewness, R_{sk} equal to 1.64 indicates low asymmetry relative to the mean and quantifies relatively non-dense distribution of peaks. Kurtosis, R_{ku} equal to 5.39 indicates more sharp peaks than valleys of the glass surface.

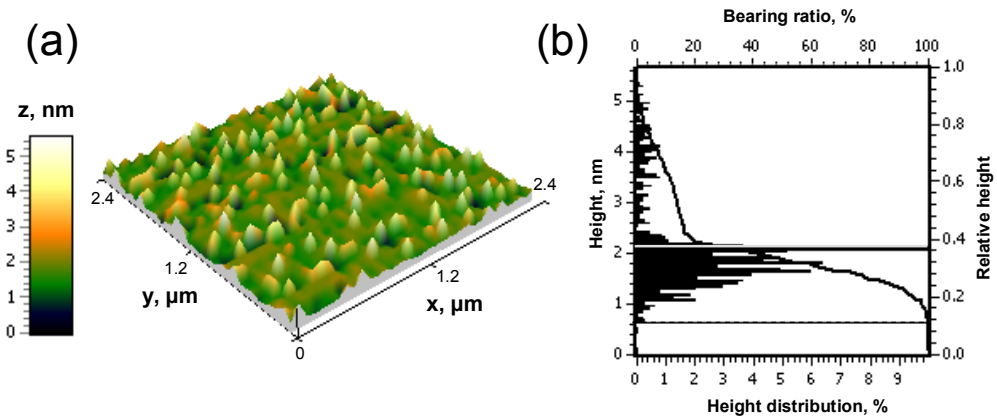

Fig. 33. AFM 3D characteristic topographical image with normalized Z, nm scale of (a) glass surface prepared using RCA-1 clean with (b) normalized height distribution histogram and bearing ratio curve. Dashed line indicates the height at which surface structures are connected to each other. The middle line indicates the mean height.

It is considered that the following surface morphology contribute to the basic model that predicts the effects of roughness, asymmetry, and flatness on the adhesion and contact as discussed in [5] and hydrophilic properties as it was observed by contact angle measurements. In Fig. 33b, the height distribution histogram and bearing ratio curve of the substrate surface is shown. It is an interpretation of similar surface roughness characteristics however it includes not only the rough layer of the surface but all space described by the AFM image. Reduced peak height (R_{pk}) for glass substrate surface was equal to 2.6 nm with surface structures ranging from 2.4 nm to 5.0 nm i.e. from the base of normalized height. Core-roughness (R_k) was equal to 1.1 nm with surface structures ranging from 1.3 nm to 2.4 nm. Reduced valley depth (R_{vk}) was equal to 0.5 nm with surface structures ranging from 0.8 nm to 1.3 nm. Specifically, the local surface structures which fall into R_{pk} region could be associated with unmolten SiO_2. M. Chopinet et al. reported that unmolten grains of SiO_2 are carried towards the upper surface of the crucible due to their low density and the presence of attached bubbles during float glass fabrication process [140].

3.1.4 Surface morphology and atomic force microscope tip-sample adhesion of thermally deposited and magnetron sputtered chromium thin films

In this work, glass substrate was prepared using RCA-1 surface preparation method (section *2.1.2*) and air side was selected for chromium thin film deposition. Thin film deposition was performed using thermal evaporation (electron beam evaporation source) (see section *2.1.3.1*) and magnetron sputtering techniques (see section *2.1.4.1*). The thickness of chromium thin films was 50 nm. Typical AFM topographical images of thermally deposited and magnetron sputtered chromium thin films are shown in Fig. 34a and b, respectively. Thermally deposited chromium film surface topography shows a dense distribution of surface mounds with a RMS roughness, R_q, of 1.13 ± 0.02 nm. In contrast, magnetron sputtered chromium surfaces contained islands, formed during the fusion of surface mounds, with R_q value of 1.16 ± 0.02 nm. Despite nearly equal R_q values of chromium films deposited using both methods, thermally deposited chromium thin film surfaces exhibited smaller skewness (R_{sk} = 0.61 ± 0.05) and kurtosis (R_{ku} = 3.49 ± 0.05) as compared to those of magnetron sputtered chromium thin films (0.80 ± 0.03 and 4.98 ± 0.07, respectively). Tabulated values of chromium thin film surface morphology parameters determined using AFM are presented in Table 14.

It can be proposed that the localized islands seen in Fig. 34b are responsible for increased R_{ku} values. Topographic profile images along a diagonal line in the middle of scan were constructed from AFM data and are also shown in Fig. 34a and b, for both deposition techniques. An approximate surface mound width of the thermally deposited chromium films ranges from 0.1 to 0.4 μm whereas islands in magnetron sputtered films are - 0.5 to 2.0 μm showing a lower propensity towards aggregation. The distribution of surface mounds and localized islands shown in Fig. 34b were quantified in terms of porosity. Porosity was defined as the percentage of pore area

with respect to total sample area and obtained after noise reduction and flattening of the image, pore shape regularization, binarization and quantification operations. Details for the method can be found elsewhere [141]. The mean value of porosity for five images was determined to be 0.73 for thermally deposited chromium films as compared with 0.54 for magnetron sputtered chromium films. This shows that magnetron sputtered surfaces have better separated islands with larger connecting area. In Fig. 35a and b, height distribution and bearing ratio of thermally deposited and magnetron sputtered chromium thin films are shown. The bearing ratio goes to zero beyond 1.3 nm and 1.9 nm for thermally deposited and magnetron sputtered chromium films, respectively, indicating that surface mounds and islands are connected to each other at these heights above the surface.

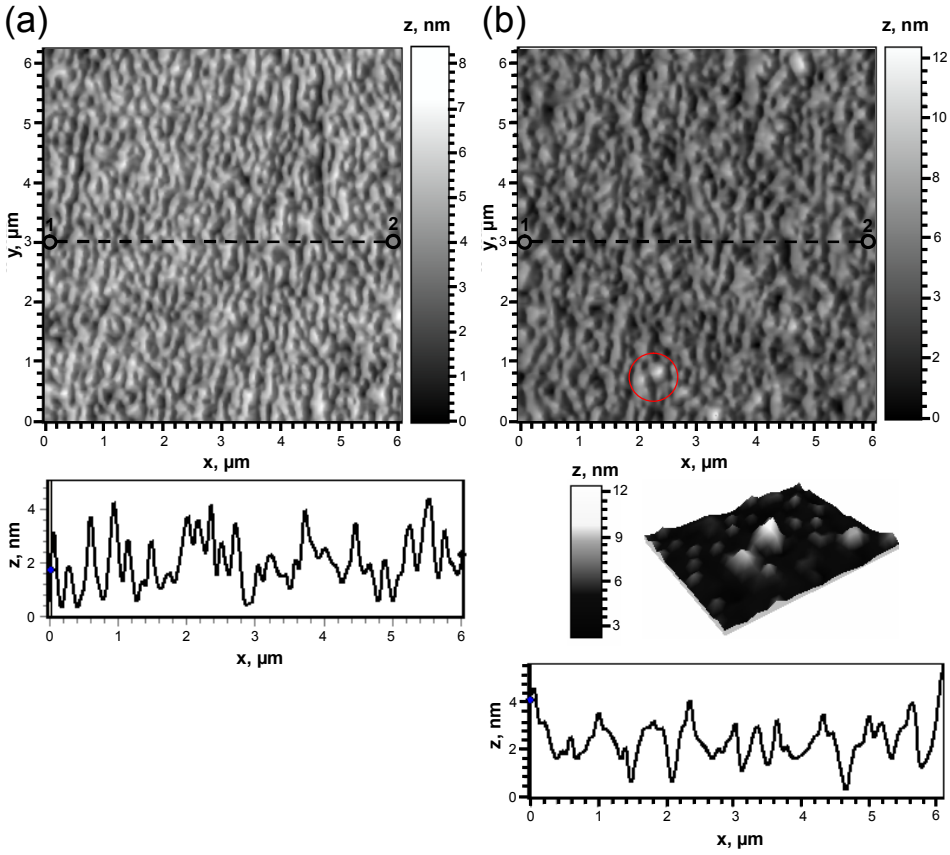

Fig. 34. Characteristic AFM topographical images of (a) thermally deposited and (b) magnetron sputtered chromium thin films with the corresponding surface profile images along the diagonal lines marked by the endpoint (1) and (2), respectively. The 3D topographical image of 1.3 × 1.1 µm in (b) shows localized islands responsible for the increased R_{ku} values for magnetron sputtered chromium thin films.

A non continuous surface feature height distribution of thermally deposited chromium thin film was obtained due to the high degree of porosity and can be seen in Fig. 35a. Smoother height distribution of surface features in magnetron sputtered chromium films resulted in continuous height distribution (Fig. 35b).

Table 14. Corresponding surface morphology parameters of thermally deposited and magnetron sputtered chromium thin films as determined from AFM measurements. Each value of surface morphology parameter represents the mean value from five measurements.

e-beam-deposited		RF sputtered	
R_q	1.13 ± 0.02 nm	R_q	1.16 ± 0.02 nm
R_{sk}	0.61 ± 0.05	R_{sk}	0.80 ± 0.03
R_{ku}	3.49 ± 0.04	R_{ku}	4.98 ± 0.07

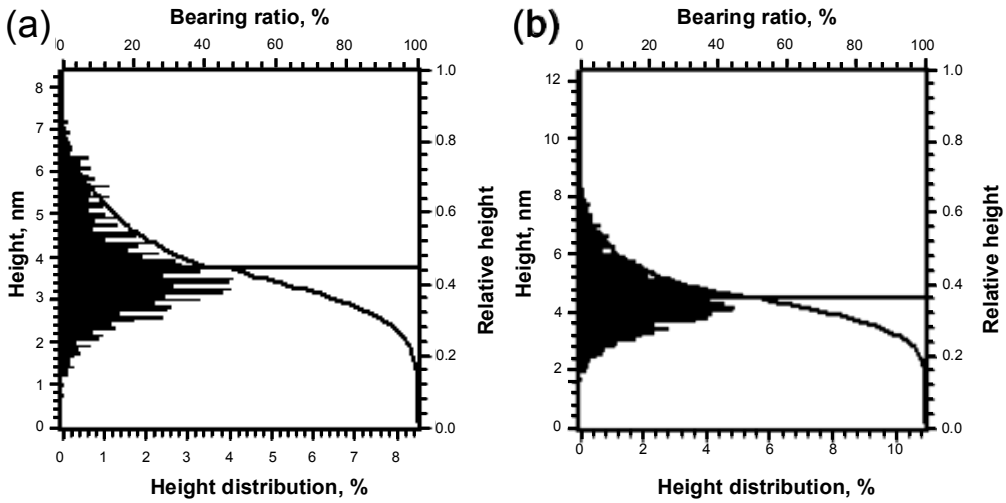

Fig. 35. Height distribution histograms and bearing ratio curves: (a) thermally deposited chromium film and (b) magnetron sputtered chromium film.

AFM tip-sample adhesive force of 284 ± 10 nN was observed for thermally deposited chromium surfaces, which is smaller than that of magnetron sputtered chromium surfaces (332 ± 17 nN) (see Fig. 36 for characteristic AFM force-distance curve that was used to extract adhesion values). It is proposed that magnetron sputtered chromium surfaces had a larger flat area over which the adhesion forces were active during interaction with the AFM tip, resulting in a higher adhesive force. This data agrees with the basic model predicting the effects of roughness, asymmetry, and flatness on adhesion as discussed by Tayebi and coworkers [142]. Additionally, the presence of surface contaminants or oxide layers may considerably alter adhesive behavior of the surfaces [143].

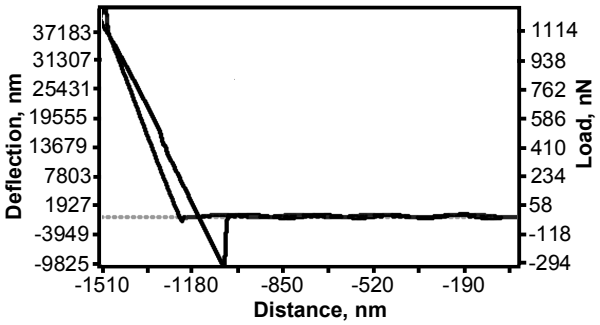

Fig. 36. Characteristic AFM force-distance curve measured on magnetron sputtered chromium thin film surface.

3.1.5 Chemical and structural properties of thermally deposited and magnetron sputtered chromium thin films

XPS *s*urvey spectra of samples prepared by thermal evaporation and magnetron sputtering techniques (as in section *3.1.4*) were used for elemental surface sensitive quantification and shown in Fig. 37. From these spectra, peaks due to carbon, chromium and oxygen can be observed. To elucidate possible differences between the two vacuum deposition techniques used on chemical composition of chromium thin films, high resolution spectra were obtained and atomic concentration analysis was performed and presented in Table 15.

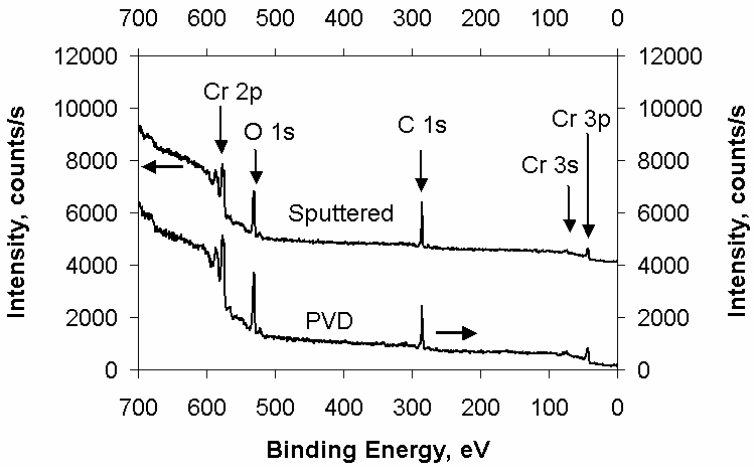

Fig. 37. Survey XPS spectra of thermally deposited (indicated as "PVD") and magnetron sputtered (indicated as "Sputtered") chromium thin films

It can be seen that for both samples surface atomic composition is very similar. It can be proposed that relatively large amounts of carbon found on the surface of both samples originates from atmospheric contaminants – similar to those found in [144].

Chromium thin film deposition was performed in a vacuum chamber different than that used for XPS measurements, thus atmospheric contamination may have occurred during transport. It is also known that some amount of oxygen is always found on the surface of a sample if the sample was exposed to air after deposition [144]. In such a case the amount of oxygen on the surface of the sample can exceed the theoretical value for pure oxides [144, 145].

Table 15. Atomic concentrations calculated from XPS data of thermally deposited and magnetron sputtered chromium thin films.

Sample	Atomic concentrations, %		
	Cr 2p	O 1s	C 1s
Thermally deposited	26	31	43
Magnetron sputtered	24	30	46

To investigate chemical bonding of chromium thin film surfaces and to reveal differences in chemical composition between samples deposited using two different methods, high resolution XPS spectra were analyzed using peak fitting. Results of the fitting procedure for chromium, oxygen and carbon spectra for both samples are presented in Fig. 38a, b and c respectively. High resolution Cr 2p XPS spectra shown in Fig. 38a are peak fitted using four components for both samples. The metallic chromium peak position has previously been reported at 574.5 eV [146], 574.1 eV [30], 574 eV [147] or 574.2 eV [148]. Therefore the peak at 573.7 eV can be assigned to Cr-Cr bonds in metallic chromium. A smaller component located at 575.2 eV can also be seen in Fig. 38a. This component can be attributed to CrO_x ($x<<2$) or mixed Cr-O-C bonds [16]. We assigned a peak at 576.4 eV to Cr-O bonds in Cr_2O_3 in good agreement with the values reported in the literature (Cr_2O_3 at 576.6 eV [147, 148]). Lastly, the component at 577.7 eV can be assigned to Cr-OH bonds in $Cr(OH)_3$ in agreement with the literature value of 577.3 eV [148]. High resolution XPS spectra of O 1s region in Fig. 38b show three components. The first component at 529.9 eV is in a good agreement with the data reported in the literature for Cr-O bonds in Cr_2O_3 [30, 144, 148], in agreement with the Cr-O peak in Cr 2p spectra. The second peak at 531.6 eV can be attributed to two overlapping peaks of O-H bonds in $Cr(OH)_3$ [144, 148] and O-C bonds from atmospheric contaminants [149]. The small peak at 533.3 eV is due to the O-H bonds of water vapor adsorbed on the sample surface. From Fig. 38a and b it can be seen that O 1s and Cr 2p spectra for samples prepared using two different methods are almost identical. In particular, peak positions and peak heights are very similar. However the high resolution spectrum of C 1s region (Fig. 38c) showed one major difference. In this spectrum the fitting procedure resulted in four well-defined components in the e-beam-deposited sample whereas only three in magnetron sputtered samples. Both samples show strong components at 284.8 eV assigned to C – C and C – H bonds [147, 150]. Two components at higher binding energy region are almost identical for both e-beam-deposited and sputtered films.

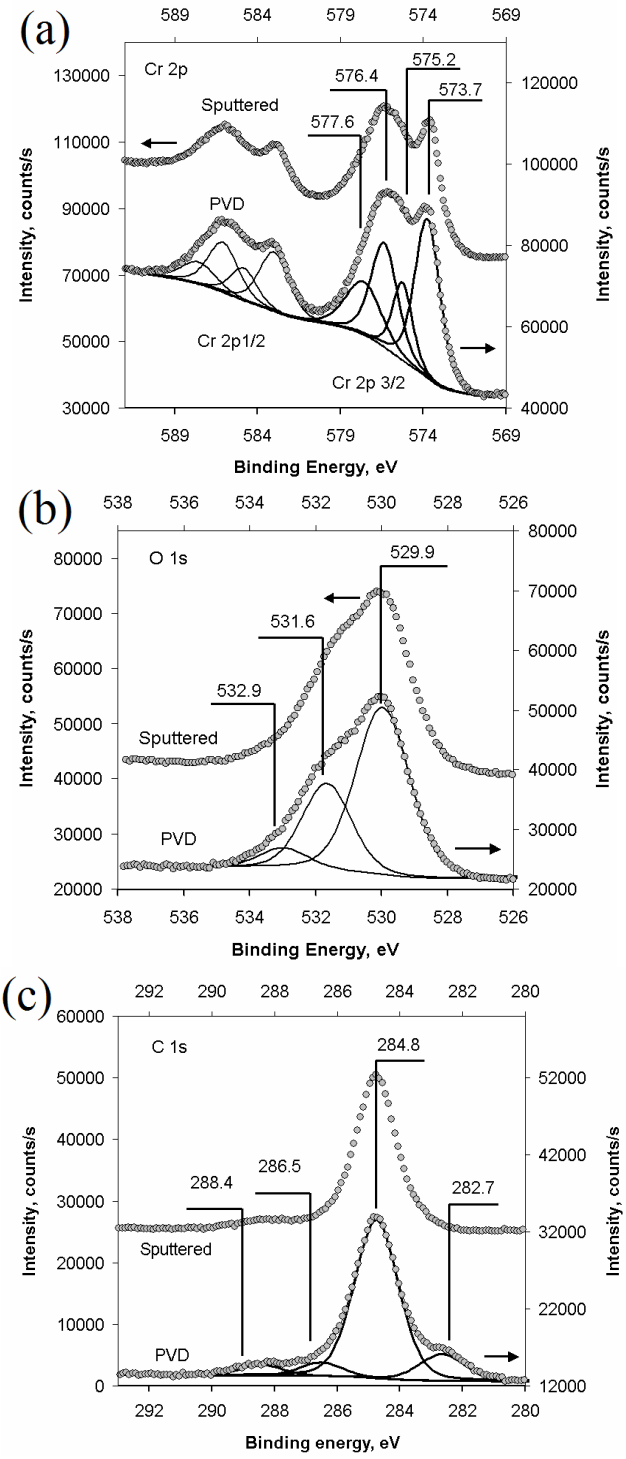

Fig. 38. High resolution XPS spectra with fitted components in (a) Cr 2p, (b) O 1s and (c) C 1s regions.

They are located at 286.5 eV and 288.4 eV and are in good agreement with literature data for C–O and O-C=O bonds, respectively [147, 148, 150]. These two components can originate from atmospheric contamination [151]. For thermally deposited chromium samples (Fig. 38c) a well-pronounced component, located at 282.7 eV, can be seen. It is due to the C-Cr bonds, as compared to the values reported in the literature at 282.6 eV [147] to 283.3 eV [150]. It can be proposed that formation of C-Cr bonds is due to organic contamination left on the substrate surface during the initial stages of metallization [152] or due to residual gas from the substrate during the heating procedure. Additionally, impurities in thermally deposited chromium films could arise from base pressure differences between magnetron sputtering and thermal evaporation systems [20]. Finally, surface nanostructure differences between thermally deposited and magnetron sputtered chromium films could arise due to a shadowing effect and the mean free path of sputtered particles as discussed in [31].

The XRD patterns of the thermally deposited and magnetron sputtered chromium thin films are shown in Fig. 39. XRD patterns of thermally deposited chromium thin films on glass substrates shows one peak with 2θ at 44.2° which is indicative of the body-centered cubic (110) plane of Cr metal crystal lattice structure. Peaks corresponding to the (110) reflection with 2θ of 44.5° and a weak (211) reflection with 2θ at 81.7° were observed for magnetron sputtered chromium thin films.

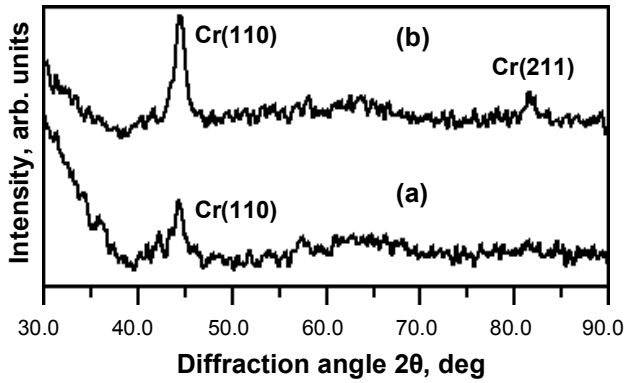

Fig. 39. X-ray diffraction patterns of Cr thin films deposited using (a) thermal evaporation and (b) magnetron sputtering.

The interatomic distance between (110) atomic planes (d-spacing) in thermally deposited and magnetron sputtered chromium thin films was determined to be 2.0445 Å and 2.0326 Å, respectively. d-spacing of 1.1772 Å was determined for (211) planes in magnetron sputtered chromium thin films. Since substrates were heated up to 100ºC before deposition, changes in observed diffraction pattern may come from the chemical reactivity between Cr and Ar during magnetron sputtering. Weak (211) reflection of magnetron sputtered chromium thin films could be attributable to a different chromium film condensation and growth mechanism

which resulted in larger separation of the islands consisting of trapped chromium crystallites.

3.2 A comparative evaluation of novel chromium composite thin films

3.2.1 Surface morphology, cohesive and adhesive properties of one-step and two-step thermally deposited chromium thin films

Firstly, glass substrate was prepared using RCA-1 surface preparation method (section *2.1.2*). The air side of soda–lime–silica float glass was selected for thin film deposition. One-step thermal deposition of chromium thin film was performed using thermal evaporation (resistively heated source) (see section *2.1.3.1*). Two-step thermal deposition was performed as described in section *2.1.9*. The thickness of chromium thin films was 120 nm. AFM 3D topographical images of one-step and two-step thermally deposited chromium thin films are shown in Fig. 40a and b. For one-step and two-step thermal deposition of chromium thin films, the surface RMS roughness values of 0.90 nm and 0.85 nm were observed. Analysis of R_{sk}, parameter reveals smoothening of the sharp surface islands (see Fig. 40a and b) with skewness values of 0.79 and 1.12 for one-step and two-step thermal deposition of chromium thin films. Such a skewness, in case of one-step deposition, may come from deposited layer-to-peaks cover on the glass substrate surface with Cr_xO_y formation at the initial deposition stages and growth of metallic chromium on the top of the oxide layer as it was observed in [30]. The kurtosis values for one-step thermal deposition of chromium thin films had a value of 4.29 while for two-step deposition process it had a value of 5.81. Surface treatment with O_2 plasma after first deposition resulted in possible formation of amorphous thin chromium oxide layer [153] which initiated different chromium condensation mechanism during second deposition process giving different height distribution of the surface structures.

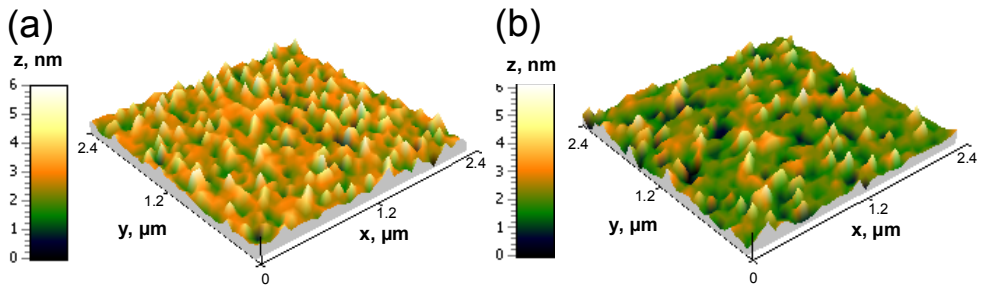

Fig. 40. AFM 3D characteristic topographical images with normalized Z, nm scale: (a) one-step thermally deposited chromium film surface and (b) two-step thermally deposited chromium film surface.

In Fig. 41a and b the height distribution histograms and bearing ratio curves of one-step and two-step thermally deposited chromium film surfaces are shown. Reduced peak height (R_{pk}) equal to 1.4 nm and 1.2 nm with surface structures ranging 4.0-5.4 nm and 3.7-4.9 nm for one-step and two-set thermally deposited chromium films. Core-roughness (R_k) equal to 2.4 nm and 2.6 nm with surface structures ranging 1.6-4.0 nm and 1.1-3.7 nm for one-step and two-set thermal deposited chromium films. Reduced valley depth (R_{vk}) equal to 0.6 nm and 0.8 nm with surface structures ranging 1.0-1.6 nm and 0.3-1.1 nm for one-step and two-set thermal deposited chromium films. The influence of differences in chromium films surfaces morphology observed from detailed analysis of gathered AFM data on the film/substrate adhesion will be discussed later in this section.

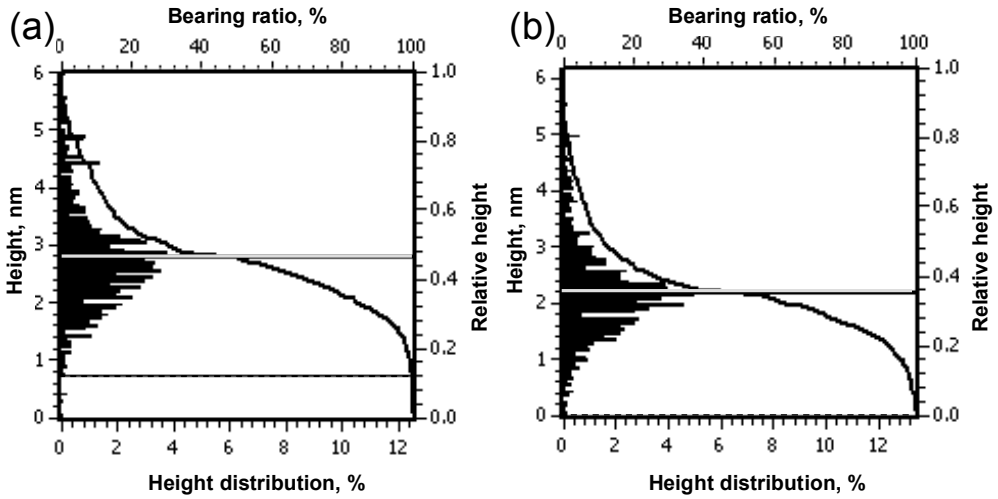

Fig. 41. Normalized height distribution histograms and bearing ratio curves: (a) one-step thermally deposited chromium film surface and (b) two-step thermally deposited chromium surface. Dashed line indicates the height at which surface structures are connected to each other. The middle line indicates the mean height.

During a scratch test, normal force, friction coefficient, penetration depth and residual depth were recorded by the CSM Nano Scratch Tester. Cohesive and adhesive properties of the films were evaluated according procedure described in section *2.2.9.1.* Briefly, these properties were evaluated by comparing critical load (L_{c1}) at which the first crack or failure appears on the film (i.e. cohesive failure) and another critical load (L_{c2}) at which the full delamination of the film occurs (i.e. adhesive failure). Fig. 42a and b shows characteristic resulting curves as a function of the scratch length for one-step and two-step thermally deposited chromium films, respectively. The results show that two-step thermally deposited chromium thin films have better cohesive and adhesive properties, the first delamination occurring at 165 ± 10 mN (Fig. 43a) and the full delamination at 221 ± 5 mN (Fig. 43b) while the first delamination for one-step thermally deposited chromium thin films occurs

at 81 ± 8 mN (Fig. 43c) and the full delamination at 198 ± 5 mN (Fig. 43d). Moreover, the results are very repeatable as shows the low value of standard deviation. Both films exhibit very similar elastic recovery properties as observed from penetration depth and residual depth curves. The summary of critical load results is presented in Fig. 44.

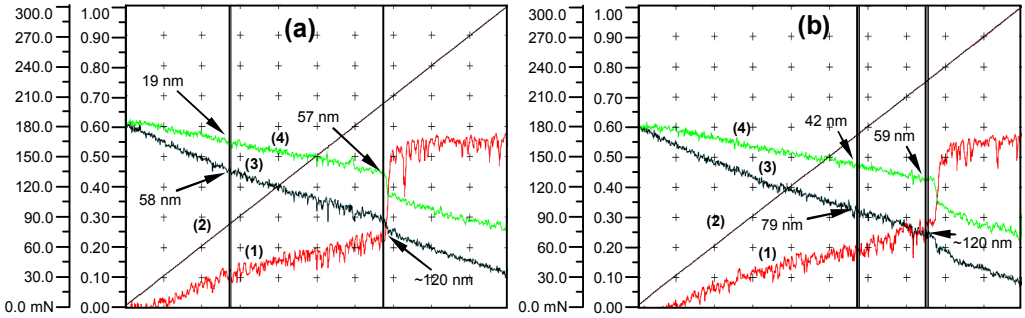

Fig. 42. Scratch test data for (a) one-step and (b) two-step thermal deposited chromium thin films. Friction coefficient (1), normal force (2), penetration depth (3) and residual depth (4) characteristic resulting curves as a function of the scratch length are shown. First vertical axis (from right to left) corresponds to the friction coefficient and the second axis to normal force. Vertical lines indicate the critical loads. Arrows indicate the penetration depth and residual depth at the critical loads.

Considering contact mechanics of the indenter with surface peaks which fall in the upper region of bearing ratio curve it is suggested that scratches with progressive load, fixed rate conditions induce very high contact stresses in surface peaks resulting in chromium film crack or spall which covers those peaks under tensile stresses. Once the chromium film spalls the wear particles could act as an abrasive causing more damage to the film with increased friction. One-step thermal deposited chromium films exhibited slightly higher R_{pk} and lower R_k values with higher probability of the indenter meeting such peaks during scratch path and lower distribution of structures which bear the load of the indenter influencing earlier cohesive failure of the film. Additionally, slightly higher R_{vk} for two-step thermal deposited chromium films could result in reduced contact friction with indenter due to higher random occurrence of voids/dimples on the surface which trap wear particles and reduce abrasion. It is also observed that Cr_xO_y (i.e. passivation by atmospheric oxygen [154, 155])/Cr/Cr_xO_y (i.e. O_2 plasma induced oxidation [156])/Cr/Cr_xO_y (i.e. Cr_xO_y formation mechanism as observed in [30]) multilayered composite-substrate system results in improved adhesion and wear resistance and less eruption of the film (due to multilayer boundaries) as observed from Fig. 42a and b and Fig. 43b and d when compared to that of single Cr_xO_y/Cr/Cr_xO_y.

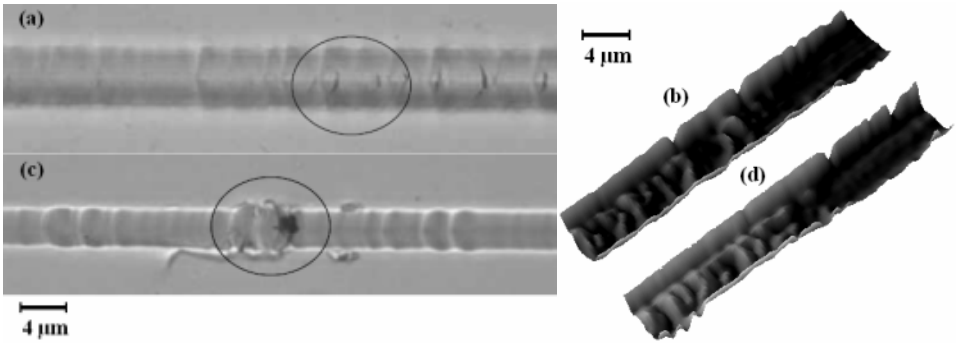

Fig. 43. Optical micrographs and 3D surface plots of critical failure points along a progressive load scratch performed on two-step (a) and (b), and one-step (c) and (d) thermally deposited chromium thin films. The first failure, L_{c1} (a) and (c), corresponds to initial cracking (indicated by ellipse markers), the second failure, L_{c2} (b) and (d) to the full delamination of the chromium film. Scratch direction is from left to right. The same fracture can be observed on the other samples.

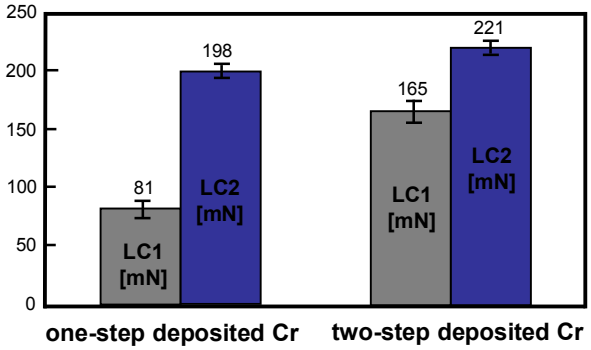

Fig. 44. Summary of critical loads results of one-step and two-step thermal deposited chromium films. L_{c1} corresponds to the first failure where the initial cracking is present and L_{c2} the second failure of the full delamination of thin films.

3.2.2 Structural and chemical properties of the two-step thermally deposited chromium thin films

Here, soda–lime–silica float glass substrate was prepared using RCA-1 surface preparation method (section *2.1.2*). The air side of glass was selected for thin film deposition. Two-step thermal deposition was performed as described in section *2.1.9*. The thickness of the two-step thermally deposited chromium films was 80 nm. The XRD pattern of the two-step thermally deposited chromium film (Fig. 45) showed a broad peak centered at $2\theta = 24.6°$ implying the resulting film might be partially amorphous [157-159]. As the chromium film was very thin the broad peak might have appeared due to the soda-lime-silica float glass contribution [160]. Importantly,

a well-defined peak centered at 2θ = 44.5° was observed, which was indicative of the body-centered cubic Cr metal crystal lattice structure (110) plane. The appearance of the body-centered cubic (110) plane of Cr metal crystal lattice structure was attributed to the low substrate heating temperature. It is well known that the substrate heating temperature plays an important role in the chromium film condensation and growth mechanism. From the previous XRD studies [19-21] of chromium films deposited on the glass substrates it can be seen, that with no substrate heating (or with substrate heating at the temperatures lower than 100°C), the body-centered cubic (110) plane of Cr metal crystal lattice was observable, while with the substrate heating temperatures in the range of 250-350 °C the body-centered cubic (200) plane of Cr metal crystal lattice structure was observable.

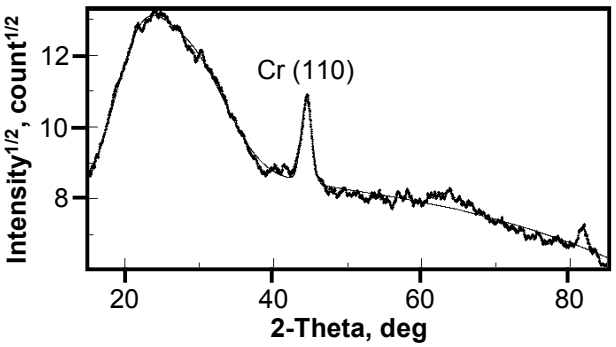

Fig. 45. X-ray diffraction pattern of the two-step thermally deposited chromium film.

High resolution XPS spectra of Cr 2p and O 1s regions of two-step thermally deposited chromium film are shown in Fig. 46 with the corresponding quantification shown in Table 16. Spectra are shown before and after the first etching cycle whereas the quantification is provided for the five consecutive etching cycles. It can be seen that the native sample contains a sharp doublet with Cr $2p_{3/2}$ peak at 574.2 eV due to the metallic Cr with the broad peak around 576.9 eV due to the mixed oxide and hydroxide species [144]. Additionally, Biesinger *et al*. showed that a complex Cr 2p multiplet structure arises making exact quantification of the oxygenated chromium compounds on the surface difficult due to the multiplet splitting, shake-up and plasmon loss structure overlapping peaks [161]. O 1s region showed two peaks at 530.6 and 532.0 eV due to the chromium oxide and hydroxylated chromium, respectively [144]. Elemental quantification performed showed that the surface is comprised of ~67% oxygen with the remainder of chromium thus indeed confirming oxidative behavior.

After the first etching cycle of 120 s, higher energy features due to the oxygenated chromium compounds disappeared and only metallic chromium peak was present. This type of Cr 2p speciation remained constant throughout the etching analysis until chromium signal completely disappeared. O 1s region, however, showed presence of ~2% of oxygen within the first five etching cycles (with no silicon signal detected), until oxygen signal from soda-lime-silica float glass

substrate started appearing. No distinct oxygenated layer, however, was detected during the etching experiment. Combined with the observation of the small amount of oxygen signal, we can propose that (a) during the deposition interlayer oxygen diffused into the chromium films or (b) high energy argon beam induced structural disorder thus resulting in an averaged oxygen signal throughout the sample. Latter is possible since high energy argon ion beam is known to dramatically perturb the thin film structure [162].

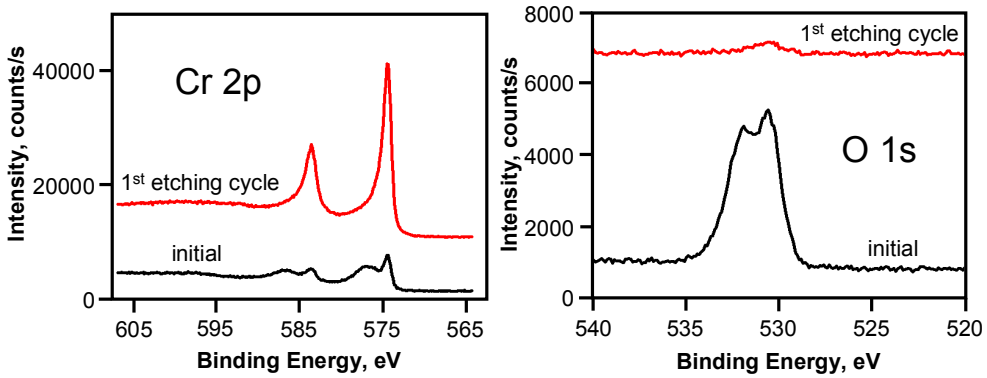

Fig. 46. High resolution Cr 2p and O 1s region XPS spectra of as-deposited chromium films and after the first etching cycle.

Table 16. Elemental quantification of the two-step thermally deposited chromium film obtained using XPS depth profile.

Etching time, s	Cr 2p %	O 1s %
0	37.9	62.1
300	96.4	3.6
600	97.2	2.8
900	97.3	2.7
1200	97.8	2.2

3.2.3 Tribological properties of the two-step thermally deposited chromium thin films

Similar samples as in section *3.3.2* were tested with High Temperature Tribometer (CSM Instruments). The ball-on-disk test procedure is described in section *2.2.10.1*. A typical frictional trace of the two-step thermally deposited chromium thin film on a soda-lime-silica float glass substrate is shown in Fig. 47a and b. The advantage of the wear tests performed here, when compared to the previously conducted scratch tests of the two-step thermally deposited chromium films, was the determination of the film-substrate lifetime. In many coatings

applications, the resistance to wear can be more important than the load required to permanently damage the material [133].

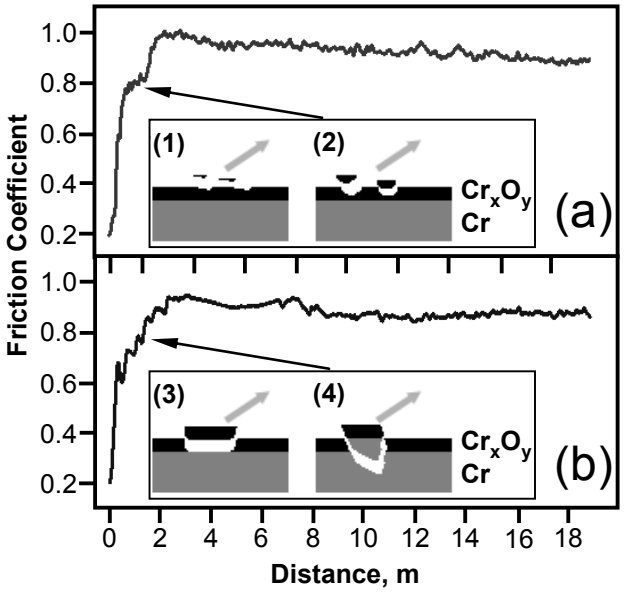

Fig. 47. Typical friction trace obtained with (a) 100Cr6 (b) and 440C bearing steel balls at room temperature on two-step thermally deposited chromium films. The detachment of Cr_xO_y takes place (1) at the top of Cr_xO_y surface, (2) within the thin Cr_xO_y layer, (3) at the Cr_xO_y/Cr interface and (4) in the Cr film during running-in period.

The static friction partners were 100Cr6 and 440C balls and the sliding tests were performed at room temperature. Running-in period is achieved by an abrupt increase of the friction coefficient to a value of ~0.82 for sliding against 100Cr6 ball (Fig. 47a). After 0.3 m of sliding the friction coefficient increased to its maximum value of ~0.94 and further stabilization to its average value of 0.9 was achieved. For sliding against 440C ball (Fig. 47b), the running-in period was accompanied by an abrupt increase of the friction coefficient to a value of ~0.6 and a stepwise increase of the friction coefficient to a value of about ~0.93. After 7.4 m of sliding, the friction coefficient was slightly reduced and further stabilization to average value of 0.87 was achieved. The variation of the friction coefficient for sliding against 100Cr6 and 440C balls during running-in period could be associated with the thin native oxide layer (Cr_xO_y), which covers the metallic chromium film, removal. It can be inferred that the removal of the thin Cr_xO_y layer during running-in period for sliding against 100Cr6 and 440C balls was dominated by the different fracture and material detachment behavior, both originating from adhesive wear [22]. The detachment of the Cr_xO_y layer took place at the top of the thin film surface (Fig. 47a inset (1)) and/or within the superficial oxide film (Fig. 47a inset (2)) for sliding against 100Cr6 ball, and at the Cr_xO_y/Cr interface (Fig. 47b inset (3)) and within the Cr film itself (Fig. 47b inset (4)) for sliding against the 440C ball. After ~18 m of

sliding at a relatively steady friction coefficient, no further changes were observed suggesting that the two-step thermally deposited chromium films endured the dry sliding wear experiments. The friction trace results are further supported by the characteristic wear track section topographical images shown in Fig. 48a and b. The topographical image of the wear track section for sliding against 100Cr6 ball (Fig. 48a) revealed that the wear was governed by an abrasive mechanism with a limited micro-scale cohesive fracture and material detachment. The abrasion and fracture wear reflections could also be observed in the topographical image of the wear track section for sliding against 400C ball (Fig. 48b). However, the cohesive fracture of material was more significant resulting in a brittle material detachment at the inner part of the wear track (characteristic region marked as (1) in Fig. 48b). This is mainly attributed to the detachment of the Cr_xO_y layer in the Cr film during running-in period, which induced crack growth during the early stages of the dry sliding. The morphology of the wear track sections was further quantified by the height distribution histograms and bearing ratio curves and is shown in Fig. 48a_1 and b_1 for sliding against 100Cr6 and 400C balls, respectively. The characteristic regions of the height distribution are indicated by markers (1), (2) and (3), which correspond to the same notation in topographical images. It is evident, that the wear of the two-step thermally deposited chromium films was also influenced by the different contact area distribution between the ball and the film during dry sliding experiment.

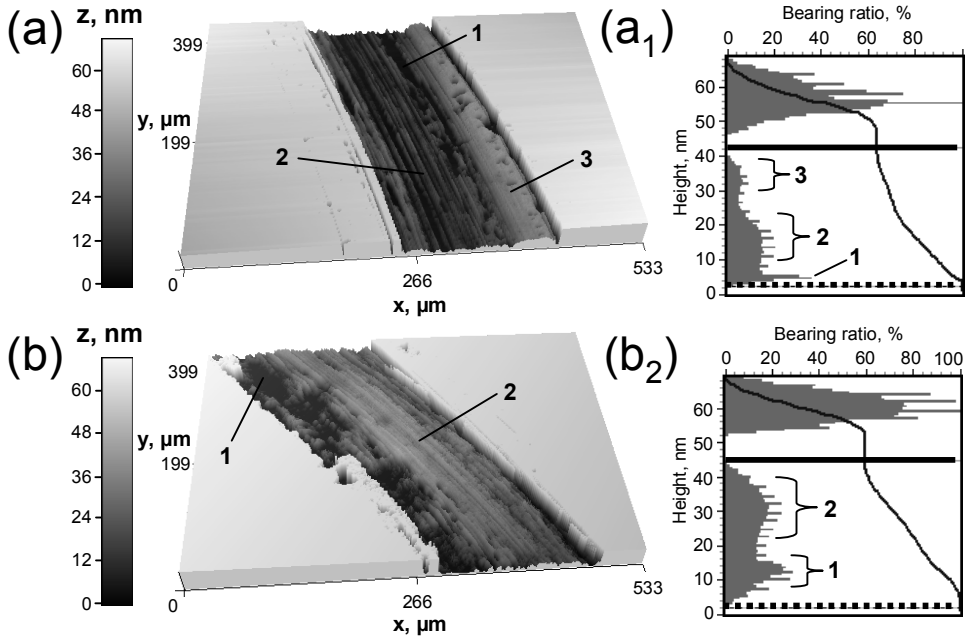

Fig. 48. Characteristic wear track section topographical images with normalized Z, nm scale for sliding against (a) 100Cr6 and (b) 400C bearing steel balls at room temperature with corresponding normalized height distribution histograms and bearing ratio curves at (a_1) and (b_1), respectively. Dashed line indicates the height at which surface structures are connected to each other. The middle line indicates the mean height.

Importantly, despite the differences in frictional behavior and wear mechanisms observed, the wear tracks exhibited nearly the same mean height (indicated by the solid horizontal line in Fig. 48a_1 and b_1) equal to 42 and 45 nm for sliding against 100Cr6 and 440C balls, respectively, indicating that only the first half of metallic chromium film was worn out after ~18 m of dry sliding. Further, chemical composition of the Cr film and the corresponding wear tracks for sliding against 100Cr6 and 400C balls was analyzed (Fig. 49a and b) via energy dispersive spectroscopy. It was confirmed that the film endured dry sliding experiments at room temperature. The initial film had a Cr mass percent value of 21.5 %, which was reduced to 14.3 and 13.5 % for sliding against 100Cr6 and 400C balls, respectively. In addition to chromium, signals corresponding to oxygen, sodium, magnesium, silicon, and calcium were detected in EDS spectra. The latter four elements originated from the soda-lime-silica float glass substrate.

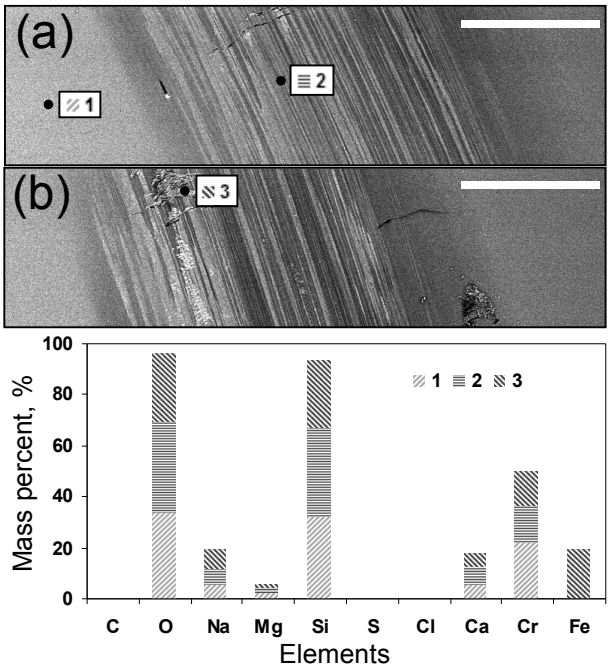

Fig. 49. SEM micrographs (scale bar of 100μm) of the wear track sections for sliding against (a) 100Cr6 and (b) 400C bearing steel balls at room temperature with EDS point analysis performed at (1), (2) and (3), corresponding to the trace of elemental composition shown (bottom).

Additional iron contribution having mass percent value of 19.2 % was detected in the wear track for sliding against 400C ball, suggesting that material transfer from the counter-part took place during the dry sliding experiment. The wear rate at the room temperature was equal to 7.96 and 8.34 × 10^{-6} mm^3/Nm for sliding against 100Cr6 and 440C balls, respectively, which is comparable with that for the hard chromate films [163, 164] used to provide abrasion resistant surface. Apart from the

dry sliding experiments at room temperature, several tests at 100 and 200 ºC were performed to check the influence of the testing temperature on the tribological properties of the chromium composite films.

Fig. 50a and b represents a typical frictional trace of two-step thermally deposited chromium film at the corresponding temperatures for sliding against 440C balls, respectively. Running-in period at 100 ºC is achieved by an abrupt increase of the friction coefficient to a value of ~0.9 for sliding against 440C ball (Fig. 50a). Afterwards, friction coefficient slightly increased to its maximum value of ~0.97 and after ~6.2 m of dry sliding and a dramatic decrease to a value of ~0.84 was observed, indicating cut-off point of the film. Next, friction coefficient gradually decreased during next ~13 m of dry sliding and further stabilization until the average value of 0.6 was achieved. For sliding at 200 ºC (Fig. 50b), the running-in period was accompanied by an abrupt increase of the friction coefficient to a value of ~0.6 and after ~0.5 m of sliding to a value of ~0.83. In contrast to sliding test performed at 100 ºC, the gradual decrease of friction coefficient to a value of ~0.75 was observed during the next ~7 m of sliding, after which more significant variations in friction coefficient were observed, indicating cut-off point of the film. The region for sliding from ~16.6 to ~35 m shows considerable fluctuations in the friction coefficient which could be associated with the removal of wear debris [165, 166]. It induced an abrupt decrease of the friction coefficient, reducing the value by ~ 50%.

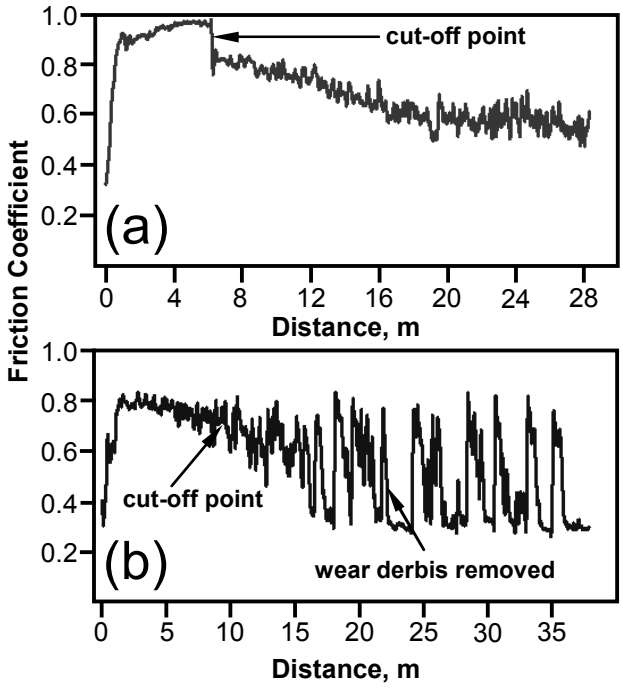

Fig. 50. Typical friction trace obtained with the 440C bearing steel balls at (a) 100 and (b) 200 ºC on two-step thermally deposited chromium films.

This behavior suggests that the wear debris generated during the sliding possibly undergoes a thermally activated chemical process which affects the material transfer on the surface of the wear track. When the removal process is interrupted, the friction coefficient tends to increase due to the further formation of wear debris. Characteristic periods with and without removal of the wear debris were observed in the corresponding region exhibiting a similar behavior. The characteristic periods follow slightly different sequential manner, indicating different states of non-homogeneous wear debris layer formation.

Frictional trace results are further supported by the characteristic wear track section topographical images, height distribution histograms and bearing ratio curves shown in Fig. 51a and b. It is evident that the two-step thermally deposited chromium films were worn out completely with the mean height (indicated by a solid horizontal line in Fig. 51 (left) a and b of the wear track) equal to 464 and 540 nm for sliding at 100 and 200 ºC, respectively. The topography of the wear tracks showed 1st and 2nd level characteristic regions which are magnified in Fig. 51 (right) a, b and indicated in the topographical images.

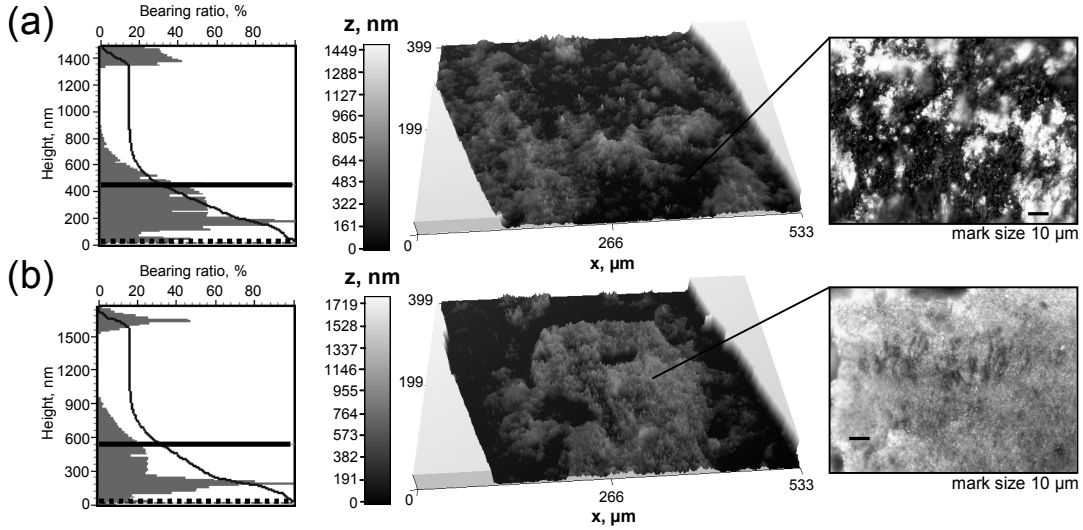

Fig. 51. Characteristic wear track section topographical images (middle) with normalized Z, nm scale for sliding against 400C bearing steel balls at (a) 100 and (b) 200 ºC with the corresponding normalized height distribution histograms and bearing ratio curves at (left), respectively. Dashed line indicates the height at which surface structures are connected to each other. The middle line indicates the mean height. Magnified 1st and 2nd level characteristic regions are shown at (right).

EDS mapping images shown in Fig. 52a_1 and b_1 confirmed that the two-step thermally deposited chromium films were worn out after sliding against 440C balls at 100 and 200 ºC. Very weak Cr signal in wear track sections was observed by point analysis using an EDS at (1) and (2) in Fig. 8a, (1) and (3) in Fig. 52b, with a mass percent value of 3.2 and 2.5 %, 4.8 and 2.5 %, respectively. Micro-particles

mainly consisting of carbon and oxygen in point (3) in Fig. 52b, which corresponds to the same notation in b_3) were observed near the edges of the wear tracks. Similar to the topographical representations of wear track sections (Fig. 51 (middle) a and b), no presence of wear scars was observed (Fig. 52a and b), confirming that the wear tracks were covered by adhered wear debris layer. The formation of a wear debris layer was probably enhanced by the progressive oxidation [167], which is confirmed by the increased amounts of oxygen in the wear track sections as determined from the EDS mapping (Fig. $52a_2$ and b_2) and EDS point analysis at (1) in Fig. 52a, (1) and (2) in Fig. 52b, which corresponds to the same notation in a_3 and b_3, respectively. No presence of iron was observed via EDS analysis of wear track sections for sliding at 100 and 200 ºC, indicating that the dominant wear was that of soda-lime-silica float glass substrate after the cut-off point of the film.

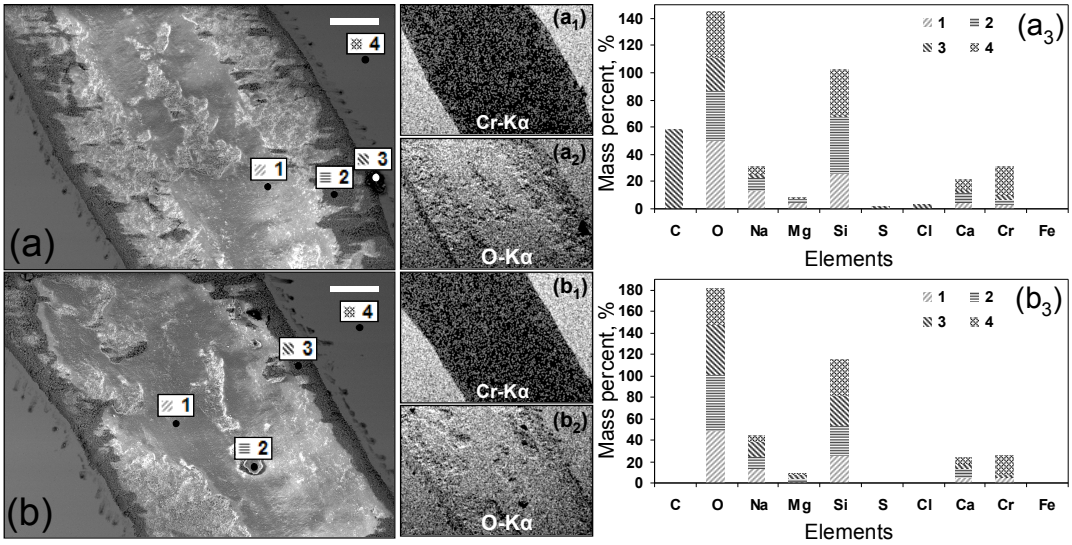

Fig. 52. SEM micrographs (scale bar of 100µm) of the wear track sections for sliding against 400C bearing steel balls at (a) 100 and (b) 200 ºC with the EDS point analysis performed at (1), (2) (3) and (4), corresponding to the trace elemental composition shown at a_3 and b_3, respectively. EDS mapping of (Cr–Kα) shown at (a_1) and (b_1), (O–Kα) (a_2) and (b_2).

3.2.4 Optical properties of one-step and two-step thermally deposited chromium thin films

The optical properties of one-step and two-step thermally deposited chromium thin films (samples as in section *3.2.1*) were determined via UV/Vis spectroscopy (section *2.2.8.1*). In Fig. 53 the characteristic reflection spectrum one-step and two-step thermally deposited chromium thin films is presented. The two-step thermally deposited chromium thin films exhibited higher reflection values in the wavelength

range of 250-800 nm as compared with films deposited using conventional thermal deposition process. The observed difference is associated with the composite structure and surface morphology of two-step thermally deposited chromium thin films.

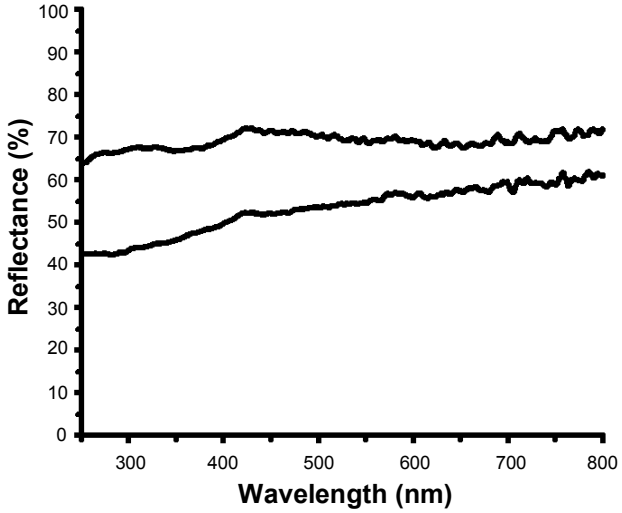

Fig. 53. Characteristic reflection spectrum of one-step (lower from bottom) and two-step thermal deposited chromium thin films.

3.3 Diamond-like carbon (DLC) and DLC-polymer composite films on chromium coated glass

3.3.1 Surface morphology, cohesive and adhesive properties of amorphous hydrogenated carbon nanocomposite films

In the present investigation, amorphous hydrogenated carbon (a-C:H), SiO_x containing a-C:H (a-C:H/SiO_x) and nitrogen doped a-C:H/SiO_x (a-C:H:N/SiOx) thin films (thickness 200 nm) were deposited on chromium composite thin film (section *2.1.9*; film thickness was 80 nm) coated glass (glass was prepared using RCA-1 clean as described in section *2.1.2*; air side was selected for chromium film deposition) using a closed drift ion beam source. Acetylene gas, hexamethyldisiloxane and hydrogen or 20% nitrogen/hydrogen mixture were used as precursors. A detailed deposition protocol is described in section *2.1.5.1*. Firstly, surface analysis was performed using atomic force microscopy via topography, surface morphology parameter, height distribution histogram and bearing ratio curve based hybrid parameter measurements. AFM 3D topographical images, normalized height distribution histograms and bearing ratio curves of characteristic a-

C:H:N/SiO_x, a-C:H and a-C:H/SiO_x surfaces obtained are shown in Fig. 54a, b and c, respectively. AFM 3D topographical images show that all three DLC films exhibit different morphologies with specific surface textures. Tabulated analysis of surface morphology parameters shown in Table 17 and obtained from AFM topography images provide further comparative details. All surfaces exhibited relatively low surface RMS roughness. The lowest RMS roughness of 0.73 nm was observed for a-C:H/SiO_x films with the surface structures having a mean height of 2.82 nm. Largest asymmetry of surface structures was observed for a-C:H films with R_{sk} value of -0.19 which indicates a predominance of valleys. Positive skewness values were observed for a-C:H:N/SiO_x and a-C:H/SiO_x films indicating more surface peaks than valleys. The height distribution of a-C:H films is sharper than on a-C:H:N/SiO_x and a-C:H/SiO_x. The surface of a-C:H:N/SiO_x film had the lowest R_{ku} value of 4.05. Relatively similar surface topography to a-C:H:N/SiO_x films has been reported to have a longer slip-rolling resistance (lifespan) [168].

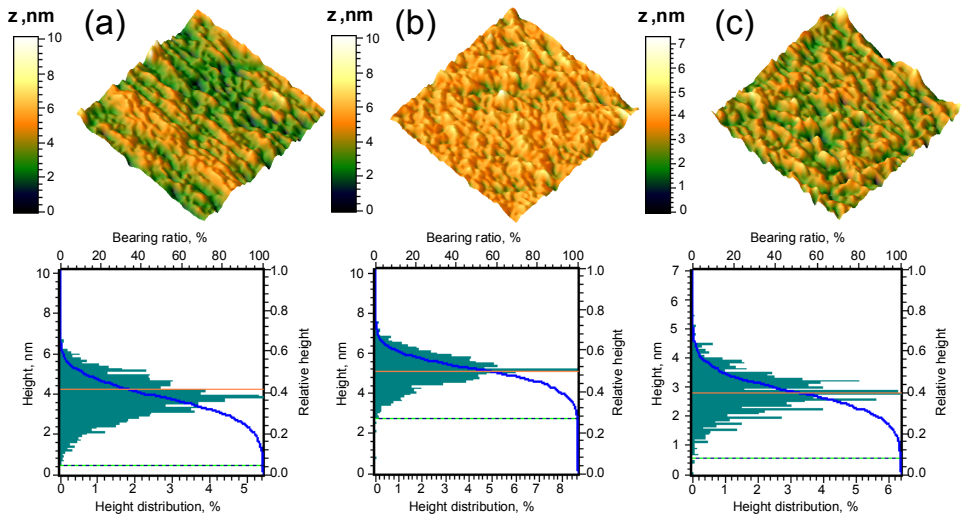

Fig. 54. (top) Characteristic 4 μm × 4 μm AFM 3D topographical images with normalized z axis in nm as well as (bottom) normalized height distribution histograms and bearing ratio curves of (a) a-C:H:N/SiO_x film surface, (b) a-C:H film surface and (c) a-C:H/SiO_x film surface. Dashed horizontal line in height distribution histogram indicates the height at which surface structures are connected to each other. The solid horizontal line indicates the mean height.

Table 17. Summary of surface morphology parameters.

Sample	Parameters						
	R_q, nm	Z_{mean}, nm	R_{sk}	R_{ku}	R_k, nm	R_{pk}, nm	R_{vk}, nm
a-C:H:N/SiO_x	1.04	3.80	0.03	4.05	2.60	0.80	1.10
a-C:H	0.84	5.17	-0.19	5.45	1.90	1.20	0.80
a-C:H/SiO_x	0.73	2.82	0.13	4.38	1.80	0.95	0.70

Secondly, cohesive and adhesive properties of amorphous hydrogenated carbon films were studied using progressive loading scratch tests (see section *2.2.9.1*) followed by optical microscopy analysis. Scratch tests were performed on all three samples with normal force, frictional force, friction coefficient, penetration depth and residual depth recorded. Fig. 55a, b and c shows characteristic resulting scratch parameter curves as a function of the scratch distance for a-C:H:N/SiO_x, a-C:H, and a-C:H/SiO_x synthesized films respectively. These results show that a-C:H:N/SiO_x films have better adhesion properties with the first delamination occurring at 24 ± 1 mN and full delamination at 134 ± 1 mN (Fig. 55a with the corresponding optical scratch image shown in Fig. 56a) while the first delamination for a-C:H/SiO_x films occurs at 21 ± 1 mN and the full delamination at 131 ± 3 mN (Fig. 55c and Fig. 56c). The full delamination critical load is very similar in the case of a-C:H:N/SiO_x and a-C:H/SiO_x films. However, a-C:H shows differences (Fig. Fig. 55b and Fig. 56b), where the first delamination occurs at 25 ± 2 mN and full delamination at 69 ± 3 mN. From the data shown in Fig. 55, a-C:H film possesses the lowest resistance to scratching. Analysis of penetration and residual depth curves shown in Fig. 55 suggests a-C:H:N/SiO_x films have better elastic recovery when compared to a-C:H/SiO_x films.

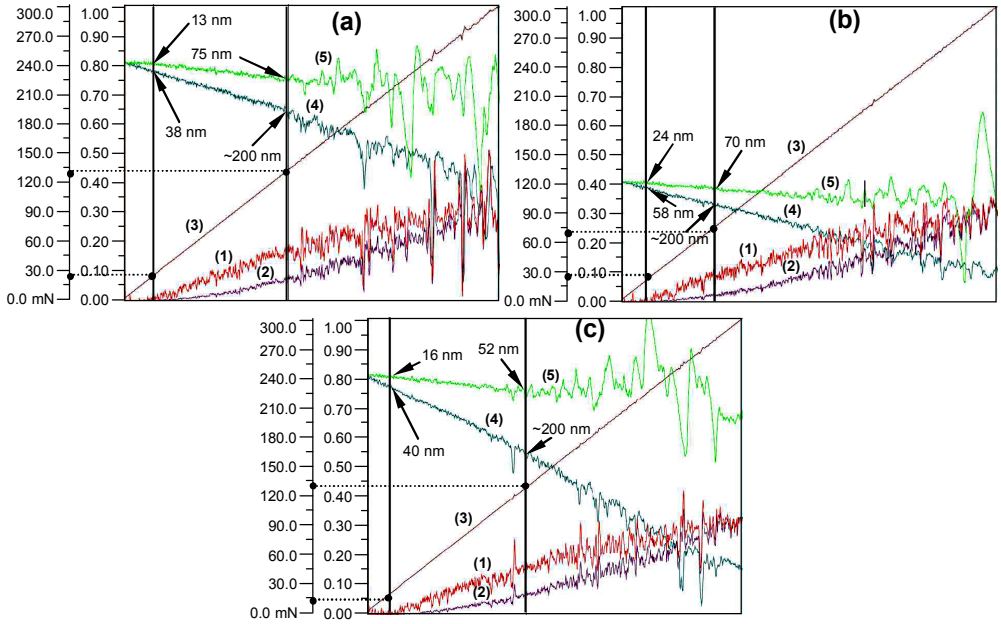

Fig. 55. Scratch test data for (a) a-C:H:N/SiO_x, (b) a-C:H and (c) a-C:H/SiO_x films. Friction coefficient (1), frictional force (2), normal force (3), penetration depth (4) and residual depth (5) characteristic resulting curves as a function of the scratch length are shown. First vertical axis (from right to left) corresponds to the friction coefficient and the second axis to frictional force and normal force. Arrows indicate the penetration depth and residual depth at the critical loads. Dotted horizontal lines indicate values of critical loads.

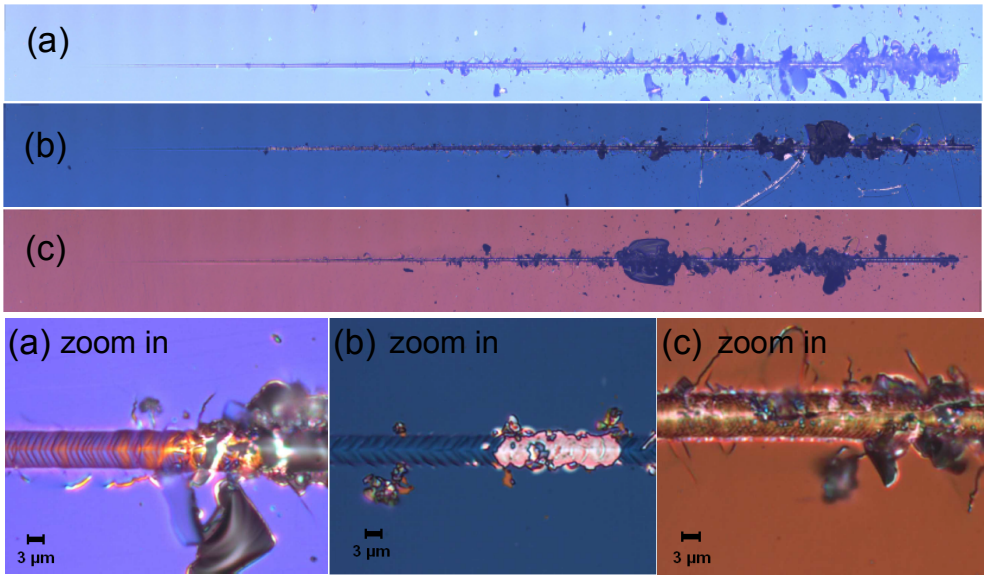

Fig. 56. (top) Optical micrographs of the scratched (a) a-C:H:N/SiO_x, (b) a-C:H and (c) a-C:H/SiO_x films. (bottom) Zoom in into the full delamination area of the film for each sample. Scratch direction is from left to right.

The increase in elastic recovery and wear resistance of the films can be associated with stronger cross-linking between graphitic planes in a-C:H:N/SiO_x films and a higher degree of structural disorder [169]. Moreover, the results are very reproducible as shown by the low value of standard deviation. The summary of critical load test results is presented in Fig. 57.

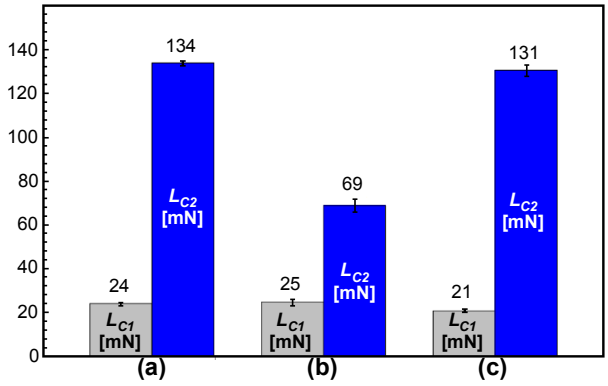

Fig. 57. Plotted summary of the critical load results of (a) a-C:H:N/SiO_x, (b) a-C:H and (c) a-C:H/SiO_x films. L_{c1} corresponds to the first failure where the initial cracking was present and L_{c2} - to the second failure at the point of the full delamination of thin films.

Although the initial surface morphology analysis and scratch data tests followed by optical inspection of the films provides quantitative information about cohesive and adhesive properties of the films, wear mechanisms in particular at the beginning of the scratching, requires some additional elucidation. AFM was used to measure critical loading sections of the scratches. AFM topographical images of L_{c1} and L_{c2} sections are presented in the Fig. 58.

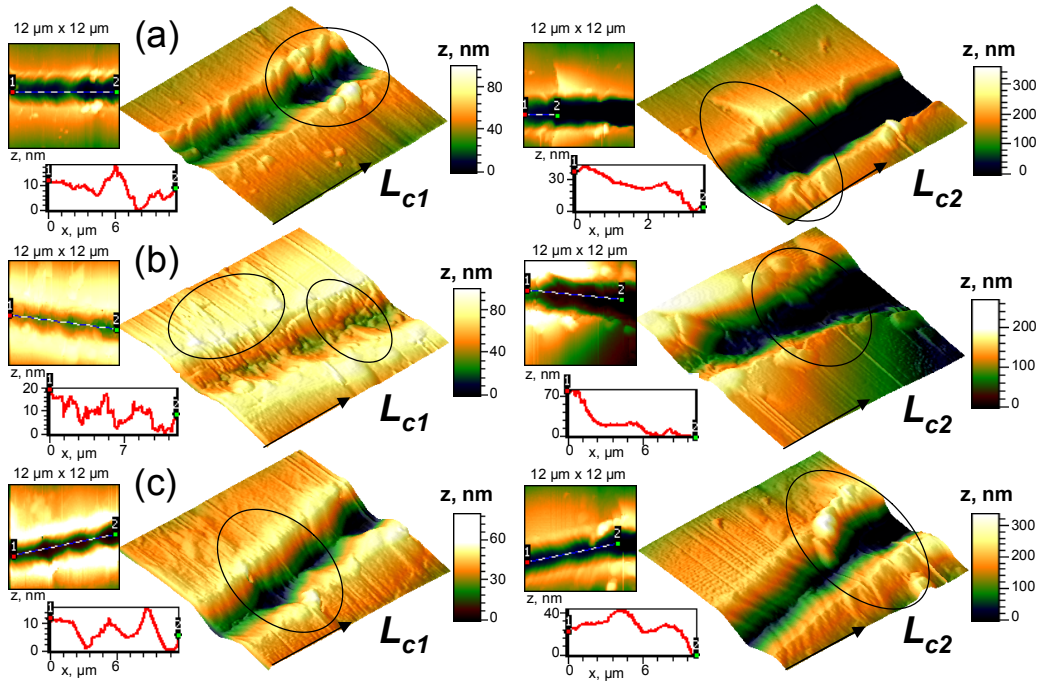

Fig. 58. Characteristic 12 μm × 12 μm AFM 3D topographical images with a normalized z scale in nm of critical loading sections along the progressive load scratch performed on of (a) a-C:H:N/SiO_x, (b) a-C:H and (c) a-C:H/SiO_x films. Length profile images of scratch track nanostructure along the diagonal lines in AFM topographical images are also shown. The first failure L_{c1} corresponds to the initial cracking (indicated by ellipsoid markers on the topography image) while the second failure L_{c2} corresponds to the full delamination of the film (also indicated by ellipse markers). Scratch direction is indicated by a black arrow.

It can be seen that the initial failure of a-C:H:N/SiO_x and a-C:H/SiO_x films was accomplished by a fracture according to a typical "herringbone" – style cracks [170] that appear in a scratch track (Fig. 58a and c at the L_{c1} section) due to the *fatigue* + *fracture* wear mechanism [171]. Compressive loading of the surface deforms it to the extent where high, mainly shear, stress is formed which exceeds the DLC film strength and the crack is formed resulting in crack growth and material detachment [171]. The same tendency could be observed for a-C:H synthesized films as "herringbone" cracks also appear on the scratch track in Fig. 56b. AFM length profile images of the L_{c1} scratch track section shown in Fig. 58a, b and c and optical

micrographs of full film delamination for each sample in Fig. 56a, b, c show good qualitative agreement. However, a distinct feature of a-C:H film is more abrupt surface topography and length profile of the scratch track as compared with the other two DLC films. This difference could be attributed to the specific surface nanostructural features of a-C:H film. This can be explained as follows. During the scratch test, the indenter first has a contact with the surface peaks which fall in the upper region of the bearing ratio curve. It is suggested that scratches at a progressive load and fixed rate conditions induce very high contact stress in surface peaks resulting in DLC film crack or spall. Once the DLC film spall, the resulting wear particles could act as an abrasive material causing more damage to the film upon increased friction. The a-C:H films exhibited higher asymmetry and R_{pk} values (Table 17) which gives higher probability of the indenter meeting such peaks during the scratch path as compared with a-C:H:N/SiO_x and a-C:H/SiO_x films. Therefore, it is suggested that not only *fatigue + fracture* wear mechanism was present during the formation of the scratch, but also a nanostructural abrasive wear which caused stronger surface deformation and debris generation resulting in a more abrupt surface topography and earlier full delamination of the film. Additionally, another film failure could be noticed in the L_{c1} scratch track section in Fig. 58b. The scratch resembles a string of beads which indicates that some amount of the film has been displaced vertically: this may result from the high brittleness and intrinsic stress of the DLC film [172]. An AFM topographical image of the a-C:H:N/SiO_x film delamination at section L_{c2} (Fig. 58a) indicates a sharp crack perpendicular to the scratch track. After this crack, adhesion between the a-C:H:N/SiO_x and Cr film is broken down and full DLC film delamination takes place. Full delamination of the a-C:H film occurs abruptly with large amounts of material detached (L_{c2} scratch track section length profile in Fig. 5b) resulting in a broadening of the scratch track while full delamination of a-C:H/SiO_x film (Fig. 58c) is initiated after the crack growth process when a critical amount of film have been pulled off. This shows that initial DLC film cracking mechanisms are the same for both a-C:H:N/SiO_x and a-C:H/SiO_x and different for a-C:H films. Furthermore, full delamination mechanisms are different for all three DLC films.

3.3.2 Surface chemical properties of amorphous hydrogenated carbon nanocomposite films

XPS analysis of a-C:H:N/SiO_x, a-C:H, and a-C:H/SiO_x films (as in section *3.3.1*) was performed. A corresponding full elemental quantification is presented in Table 18. It can be seen that a-C:H films mostly contain carbon with some amount of oxygen present on the surface. Both a-C:H/SiO_x and a-C:H:N/SiO_x contained a considerable amount of silicon with 13.4 and 24.6 % respectively. There is also a corresponding increase in surface oxygen presumably due to SiO_x bond formation. Additionally, while oxygen amounts remain the same between a-C:H/SiO_x and a-C:H:N/SiO_x, there is a decrease in carbon by ~15% in the latter. This could indicate that silicon is incorporated into this film via sp^3 hybridized diamond like, not

graphitic, sp^2 bonds with carbon. Alternatively, SiO_x formation and phase segregation proceeds. Similar O-Si-C bonds have been observed before in DLC films [173]. This additional amount of silicon is proposed to improve a-C:H:N/SiO_x thin film stress related properties. One can expect that use of 20 % nitrogen/hydrogen mixture as carrier gas contributes to lower concentration of atomic hydrogen in the flux [57] and resultant increase of Si transfer on to the surface.

Table 18. Elemental quantification obtained from XPS analysis.

Sample	C 1s %	N 1s %	O 1s %	Si 2p %
a-C:H:N/SiO_x	44.9	1.4	29.1	24.6
a-C:H	91.5	0.0	8.5	0.0
a-C:H/SiO_x	59.0	0.0	27.6	13.4

High resolution C1s XPS spectra are shown in Fig. 59 together with the corresponding peak fits. It can be seen that the major C1s peak in all three thin DLC films is due to the C-C bonds at 284.6 eV. Full width at half maximum of this peak for a-C:H:N/SiO_x, a-C:H, and a-C:H/SiO_x samples was 1.7, 1.2 and 1.5 eV, broader for both a-C:H:N/SiO_x and a-C:H/SiO_x than those typical for diamond and graphite (1.4 and 1.3 eV, respectively) [174].

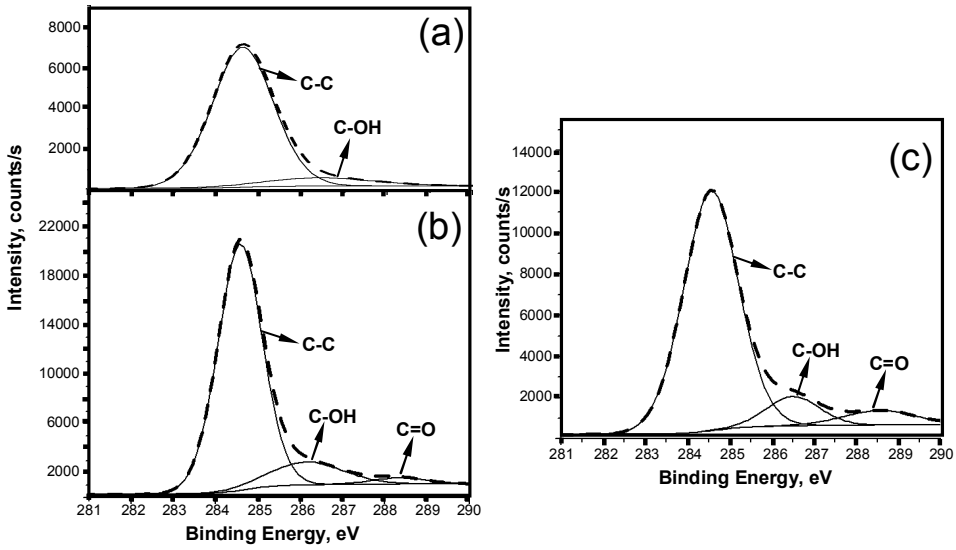

Fig. 59. High resolution C1s XPS spectra of (a) a-C:H:N/SiO_x, (b) a-C:H and (c) a-C:H/SiO_x films. Dashed lines are actual data and solid lines are Gaussian/Lorentzian product with 30% Lorentzian and 70% Gaussian character.

It can be proposed that this is due to the carbon in both sp^3 and sp^2 bonding configurations. The exact ratio, however, can't be accurately determined due to the absence of the distinct shoulders as well as due to the presence of Si-C-O bonds. Additionally, two more shoulders can be distinguished in a-C:H and a-C:H/SiO_x samples at 286.5 and 288.5 eV, assigned to C-O-C and O-C-O bonds respectively [174]. The latter peak was absent in C:H:N/SiO_x with the increased silicon and decreased carbon concentrations. In general, oxygenated carbon bonds have been shown to result in the decreased mechanical properties of the DLC films by terminate carbon network [175, 176]. It can be proposed that the presence of nitrogen atmosphere during synthesis of DLC films decreased the amount of terminal C-O bonds thus slightly improving thin films wear resistance.

3.3.3 Optical properties of amorphous hydrogenated carbon nanocomposite films combined with polyvinylpyrrolidone

In the present study, soda-lime-silica float glass was prepared using RCA-1 surface preparation method (section *2.1.2*) and air side was selected for chromium thin film deposition. Chromium thin film deposition was performed using thermal evaporation (electron beam evaporation source) technique as described in section *2.1.3.1*. The thickness of chromium thin films was 50 nm. In the first series, polyvinylpyrrolidone (PVP) films were spin-coated on Cr/glass templates from 5, 10 and 20% PVP dissolved in ethanol. More details on formation of PVP layer can be found in section *2.1.8*. In the second series, SiO_x containing amorphous hydrogenated carbon (a-C:H/SiO_x) and nitrogen doped a-C:H/SiO_x (a-C:HN/SiO_x) films were deposited on PVP/Cr/glass using a Hall-type closed drift ion beam source. The details on deposition of amorphous hydrogenated carbon films can be found in section *2.1.5.1.* Optical properties and thickness of DLC-PVP composite films was determined using UV/vis spectroscopy. Fig. 60 shows the reflectance curves of a-C:H/SiO_x/PVP5%, a-C:H/SiO_x/PVP10%, a-C:H/SiO_x/PVP20%, a-C:H:N/SiO_x/PVP5%, a-C:H:N/SiO_x/PVP10% and a-C:H:N/SiO_x/PVP20% composite films as a function of wavelength where the interference effects give rise to oscillating curves. The number of oscillating curves, in turn, depends on the film thickness. The thicknesses of undoped DLC-PVP and nitrogen-doped DLC-PVP composite films are presented in Table 19. As a result, PVP5%, PVP10% and PVP20% films on Cr/glass substrates used for a-C:H/SiO_x deposition had thicknesses of ~0.404, 0.948 and 1.221 μm, respectively. In contrast, the PVP films on Cr/glass substrates used for a-C:H:N/SiO_x deposition had thicknesses approximately of 0.408, 0.958 and 1.325 μm, respectively. The nitrogen-doped DLC-PVP composite films exhibited higher reflection values for constructive interference maxima compared to the undoped DLC-PVP composite films.

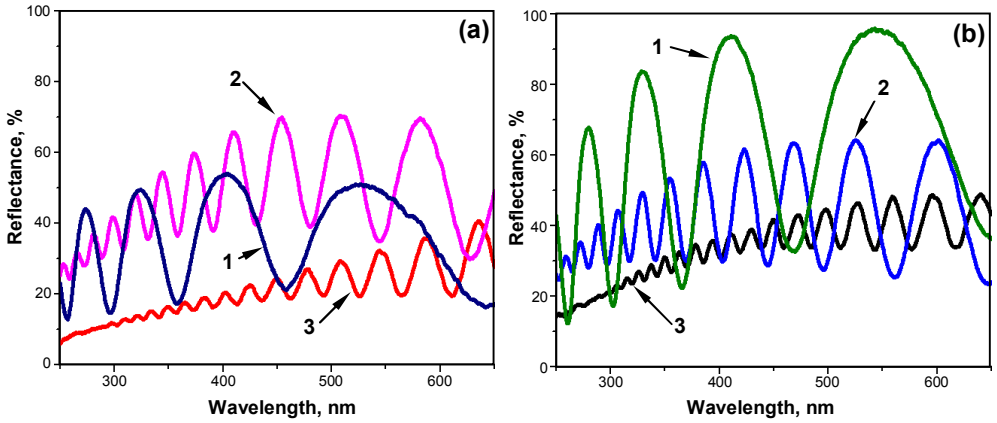

Fig. 60. Reflectance spectra of undoped DLC-PVP (a) and nitrogen-doped DLC-PVP (b) composite films. Number marks (1), (2) and (3) indicate the PVP5%, PVP10% and PVP20%, respectively.

Table 19. Summary of the thicknesses of undoped DLC-PVP and nitrogen-doped DLC-PVP composite films.

Sample	Film thickness, μm
a-C:H/SiO_x/PVP5%	0.454
a-C:H/SiO_x/PVP10%	0.998
a-C:H/SiO_x/PVP20%	1.271
a-C:H:N/SiO_x/PVP5%	0.458
a-C:H:N/SiO_x/PVP10%	1.008
a-C:H:N/SiO_x/PVP20%	1.375

3.3.4 Surface morphology of amorphous hydrogenated carbon nanocomposite films combined with polyvinylpyrrolidone

A detailed surface characterization of DLC-PVP composite films (same as in section *3.3.3*) was followed using AFM topography images, surface morphology parameters, height distribution histograms and bearing ratio curves with hybrid parameters. Typical AFM topographical images of PVP5%, PVP10% and PVP20% films on Cr/glass substrates and the undoped DLC-PVP and nitrogen-doped DLC-PVP composite films on Cr/glass templates are presented in Fig. 61a-i. The AFM topographical images directly show that the undoped DLC-PVP and nitrogen-doped DLC-PVP composite films have different morphologies with characteristic surface textures. A calculation and closer analysis of the surface morphology parameters (see Table 20) reveal many interesting features.

The surface morphology of PVP5%, PVP10% and PVP20% films on Cr/glass substrates was highly reproducible. The topography (Fig. 61a, b and c) shows a random distribution of small surface mounds with R_q as low as 0.85 nm. Negative

R_{sk} values were calculated for all PVP films, indicating that the surface valleys dominate over the peak regimes. The domination of surface valleys could be due to mass transfer processes involving the removal of ethanol by evaporation from PVP during the drying procedure. Kurtosis R_{ku} values for PVP films are near the Gaussian-like surface value of 3.0 confirming the random distribution of surface mounds. The slight deviation of kurtosis is attributable to minor localized islands (e.g. clearly seen in Fig. 61b).

It was observed that R_q values of the undoped DLC-PVP and nitrogen-doped DLC-PVP composite films are increased with increasing thickness of the PVP template. After the a-C:H/SiO_x deposition process, a clear wrinkle pattern was observed having a mean height (Z_{mean}) of 105.00, 142.77 and 133.37 nm for the a-C:H/SiO_x/PVP5%, a-C:H/SiO_x/PVP10% and a-C:H/SiO_x/PVP20% composite films, respectively. The average width of the wrinkle (with respect to the mean line of surface profile) was found to be 1.1, 1.4 and 1.6 µm for the a-C:H/SiO_x/PVP5%, a-C:H/SiO_x/PVP10% and a-C:H/SiO_x/PVP20% composite films, respectively. Disordered wrinkles were observed in topography of the a-C:H/SiO_x/PVP5% and a-C:H/SiO_x/PVP10% composite films (Fig. 61d and e) with increasing R_{sk} and R_{ku} values. The a-C:H/SiO_x/PVP20% composite films resulted in more bumpy surfaces (Fig. 61f), which had lower R_{ku} values and narrower tilt-angle distribution (i.e. more directional wrinkles) compared to the a-C:H/SiO_x/PVP5% and a-C:H/SiO_x/PVP10% composite films. After the a-C:H:N/SiO_x deposition process, lower R_q and Z_{mean} were observed for the nitrogen-doped DLC-PVP composite films. According to the skewness values, surface peaks dominate over surface valleys for the a-C:H:N/SiO_x/PVP5% and a-C:H:N/SiO_x/PVP10% composite films. However, the wrinkle structure formation for these films (Fig. 61g and h) is not clear. The topography of a-C:H:N/SiO_x/PVP5% and a-C:H:N/SiO_x/PVP10% composite films shows the dense distribution of pillars separated by the valley contour or surface mounds connected to each other forming a hill-like structures. The a-C:H:N/SiO_x/PVP20% composite films were found to have a more defined wrinkle structure with an average width of 1.15 µm. These wrinkles are separated by a larger area valley area, are shorter and more oblique (Fig. 61i) as well as having lower R_{sk} and R_{ku} values compared to surface structures observed in topography of the undoped DLC-PVP composite films. However, the a-C:H:N/SiO_x/PVP20% composite films also have relatively similar surface morphology and characteristic wrinkle structure.

Fig. 62a-f show the height distribution histograms and bearing ratio curves of the undoped DLC-PVP composite films and nitrogen-doped DLC-PVP composite films with the corresponding R_{pk}, R_k and R_{vk} values presented in Table 20. The undoped DLC-PVP composite films had R_{pk} values of 12, 15 and 16 nm with the corresponding surface structure heights in the range of 138-150, 195-210 and 196-212 nm for PVP5%, PVP10% and PVP20% samples, respectively. Nitrogen-doped DLC-PVP composite films had R_{pk} values of 26, 14 and 14 nm with the corresponding surface structure height in the range of 70-96, 80-94 and 84-98 nm for PVP5%, PVP10% and PVP20% samples, respectively.

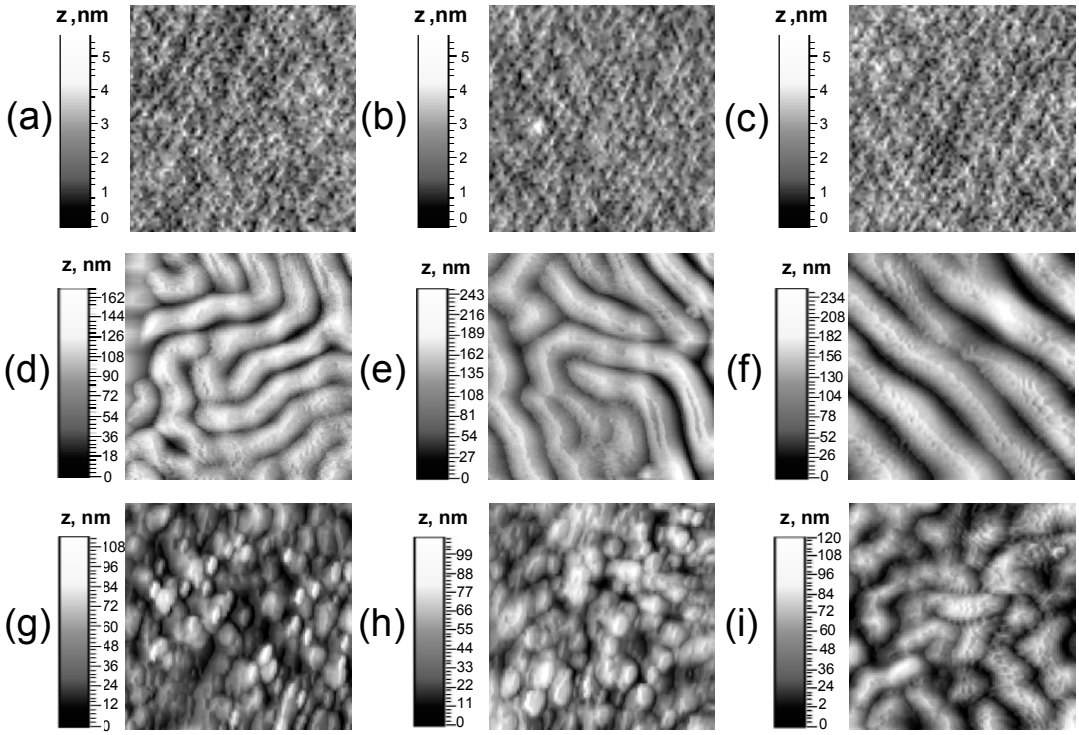

Fig. 61. AFM characteristic topographical images (12 μm × 12 μm scan size) with normalized Z, nm scale of PVP5% (a), PVP10% (b) and PVP20% (c) films and a-C:H/SiOx/PVP5% (d), a-C:H/SiO_x/PVP10% (e), a-C:H/SiO_x/PVP20% (f), a-C:H:N/SiO_x/PVP5% (g), a-C:H:N/SiO_x/PVP10% (h) and a-C:H:N/SiO_x/PVP20% (i) composite films.

Table 20. Summary of surface morphology parameters.

Sample	Parameters						
	R_q, nm	Z_{mean}, nm	R_{sk}	R_{ku}	R_k, nm	R_{pk}, nm	R_{vk}, nm
PVP5%	0.88	3.42	-0.47	3.14	1.33	0.54	1.36
PVP10%	0.91	4.10	-0.61	3.92	1.42	0.71	1.40
PVP20%	0.85	3.23	-0.82	3.03	1.50	0.60	1.50
a-C:H/SiO_x/PVP5%	24.14	105.00	-0.50	3.10	63.00	12.00	27.00
a-C:H/SiO_x/PVP10%	33.16	142.77	-0.58	3.54	90.00	15.00	45.00
a-C:H/SiO_x/PVP20%	41.33	133.37	-0.39	2.62	96.00	16.00	44.00
a-C:H:N/SiO_x/PVP5%	17.52	48.34	0.57	3.53	42.00	26.00	10.00
a-C:H:N/SiO_x/PVP10%	17.04	56.59	0.06	2.82	46.00	14.00	12.00
a-C:H:N/SiO_x/PVP20%	19.97	56.43	-0.04	2.53	56.00	14.00	12.00

Furthermore, the undoped DLC-PVP composite films had R_k values of 63, 90 and 96 nm with surface structure height in the range of 75-138, 105-195 and 100-196 nm for PVP5%, PVP10% and PVP20% samples, respectively. Nitrogen-doped DLC-PVP composite films had R_k values equal to 42, 46 and 56 nm with the surface structure height in the range of 28-70, 34-80 and 28-84 nm for PVP5%, PVP10% and PVP20% samples, respectively. Finally, the undoped DLC-PVP composite films had R_{vk} values of 27, 45 and 44 nm with the surface structure height in the range of 48-75, 60-105 and 56-100 nm for PVP5%, PVP10% and PVP20% samples, respectively. Nitrogen-doped DLC-PVP composite films had R_{vk} values of 10, 12 and 12 nm with the surface structure height in the range of 18-28, 22-34 and 16-28 nm for PVP5%, PVP10% and PVP20% samples, respectively.

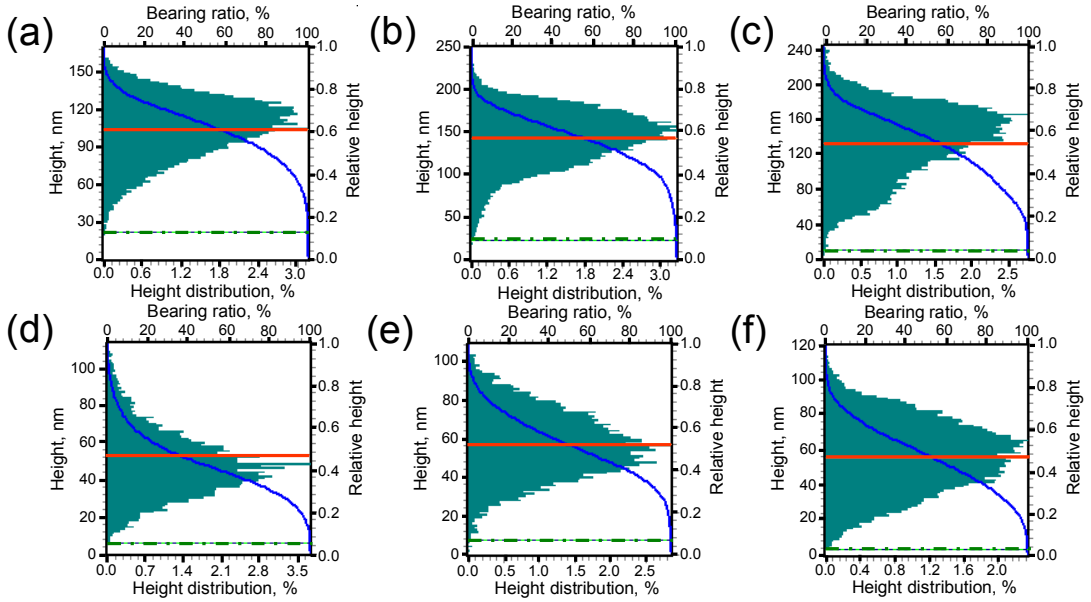

Fig. 62. Normalized height distribution histograms and bearing ratio curves of a-C:H/SiO_x/PVP5% (a), a-C:H/SiO_x/PVP10% (b), a-C:H/SiO_x/PVP20% (c), a-C:H:N/SiO_x/PVP5% (d), a-C:H:N/SiO_x/PVP10% (e) and a-C:H:N/SiO_x/PVP20% (f) composite films.

The analysis of height distribution histograms and bearing ratio curves with hybrid parameters suggests that the core roughness parameter can be tailored for the composite films by altering the PVP template thickness. For example, a higher structural uniformity could be tailored for the undoped DLC-PVP and nitrogen-doped DLC-PVP composite films by increasing the PVP template thickness.

3.3.5 Atomic force microscope tip-sample adhesion of amorphous hydrogenated carbon nanocomposite films combined with polyvinylpyrrolidone

An adhesion mapping images of composite films (as in section *3.3.3*) are shown in Fig. 63a-f. The adhesion forces observed on adhesion mapping images are in good agreement with the topography of the surfaces as seen in the AFM images. The surface structures that fall into the reduced valley depth region had higher adhesion force F_{ad}, while those that fell into the reduced peak height region revealed a reduced tip-sample adhesion. The variance in adhesion force detected was lower for the undoped DLC-PVP compared to the nitrogen-doped DLC-PVP composite films due to lower structural homogeneity of the surfaces as discussed in AFM surface morphological analysis.

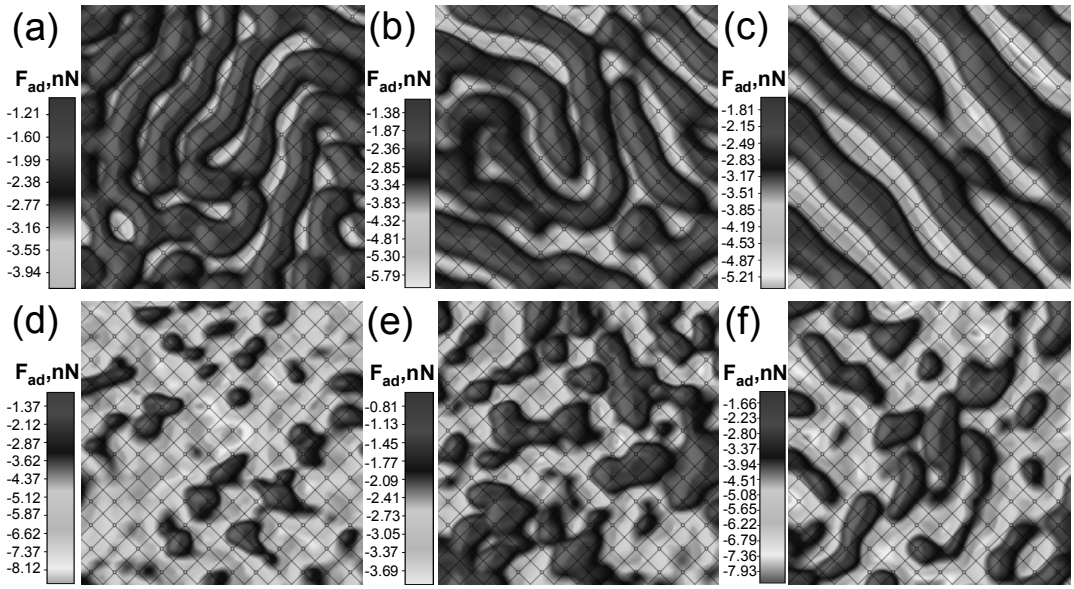

Fig. 63. Adhesion mapping images constructed by displaying the adhesion force values in spectrum look up table scheme on 12 μm × 12 μm scan size AFM topographical images with F_{ad}, nN scale of a-C:H/SiO_x/PVP5% (a), a-C:H/SiO_x/PVP10% (b), a-C:H/SiO_x/PVP20% (c), a-C:H:N/SiO_x/PVP5% (d), a-C:H:N/SiO_x/PVP10% (e) and a-C:H:N/SiO_x/PVP20% (f) composite films. The circle marks separated by mesh indicate the points where AFM force-distance curve measurements were performed.

Surface topography with deep valleys, as shown in Fig. 63c, d and f have a higher tendency to adsorb (we interpret this phenomena as the "catch effect") water molecules from the atmosphere into the deep valleys giving rise to higher van der Waals force (also capillarity force) [177], which significantly increases adhesion between tip-sample. Thus, the nano-scale thickness of thin water films is larger in valley areas. Surface topography, such as that shown in Fig. 61f, could provide directional segmentation for molecular mobility on the surface. No AFM tip

contamination resulting in significant increase in adhesive force was observed in our experiment [178]. It is important to note that adhesive forces measured with a micro-scale AFM tip would be considerably larger compared to our nano-scale AFM tip due to the larger radius of curvature for the micro-scale AFM tip, which results in a larger meniscus force contribution to the adhesive force [179]. Additionally, the thickness of adsorbed water layer and adhesion force is dependent on relative humidity (RH). For an AFM tip radius of curvature of 15.0 nm, the adhesion force is larger than 10 nN at RH values greater than 60% and becomes smaller than 5 nN for RH values lower than 20% as observed in [180]; in good agreement with our results.

3.3.6 Structural properties of amorphous hydrogenated carbon nanocomposite films combined with polyvinylpyrrolidone

FTIR spectroscopy analysis was performed to study blend behaviour of PVP upon a-C:H/SiO_x and a-C:H:N/SiO_x direct ion beam deposition (similar samples as in section *3.3.3*). Fig. 64 shows the infrared spectra of the carbonyl stretching mode of the composite films. After PVP surface modification with a-C:H:N/SiO_x for the a-C:H:N/SiO_x/PVP20% composite films, infrared absorption features were observed, including a strong C=O stretching mode at 1710-1660 cm^{-1} (peak maximum at 1674 cm^{-1}) and a strong C=O stretching mode at 1690-1645 cm^{-1}, corresponding to the free and the hydrogen-bonded carbonyl groups, respectively.

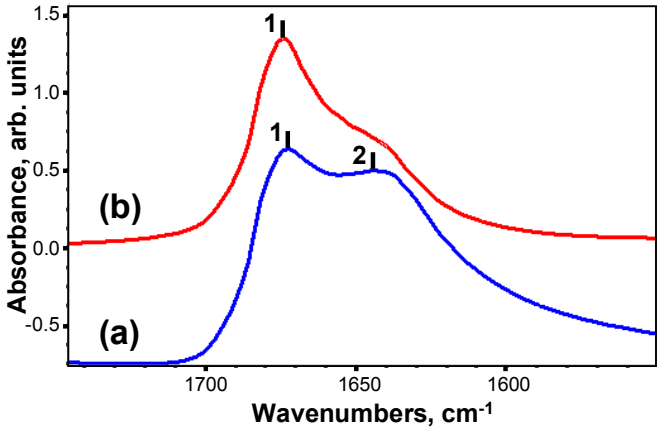

Fig. 64. FTIR spectra of a-C:H/SiO_x/PVP20% (a) and a-C:H:N/SiO_x/PVP20% (b) composite films. Assigned peaks (1) at 1672.6 cm^{-1} and (2) at 1644.0 cm^{-1} for (a); and (1) at 1674.1 cm^{-1} for (b).

This result suggests that the interactions occurring between PVP and C:H:N/SiO_x (the PVP C=O band at 1690-1645 cm^{-1}) is possibly bound with C-H bonds of a-C:H:N/SiO_x. The PVP C=O band at 1674 cm^{-1}, which corresponds to the valence vibrations in the free carbonyl groups of PVP [181] combined with a-C:H:N/SiO_x. For a-C:H/SiO_x/PVP20% composite films, the carbonyl stretching frequency is split

into two bands at 1672 cm^{-1} and 1644 cm^{-1}. The later is responsible for C=C stretching in the 1650-1605 cm^{-1} region of PVP possibly bound to C-C bonds of a-C:H/SiO_x. Very strong C=O stretching were also observed for a-C:H/SiO_x/PVP10% and a-C:H:N/SiO_x/PVP10% composite films with peak positions at 1664 cm^{-1} and 1669 cm^{-1}. These peak positions are quite low for a carbonyl band. However, N-C stretching contributions [182] in the same region can cause spectral overlap and can shift the peak position to lower wavenumbers. A substantial shift to a lower peak position also occurred for the a-C:H/SiO_x/PVP5% and a-C:H:N/SiO_x/PVP5% composite films with a C=O peak position of ~1650 cm^{-1}. The lower the peak position could also be due to intermolecular hydrogen bonding. The panoramic view of FTIR spectra within the wavelength range of 400-4000 cm^{-1} for the PVP5%, PVP10% and PVP20% films as well as both the undoped DLC-PVP and nitrogen-doped DLC-PVP composite films are shown in Fig. 65a-i. The signals corresponding to other functional groups were assigned [183, 184] and are reported in the Table 21. As no significant changes for other functional groups were observed, with the exception of signal intensity due to film thickness, it is reasonable to conclude that the main interactions involved in the blend behaviour of PVP upon a-C:H/SiO_x and a-C:H:N/SiO_x direct ion beam deposition employing a Hall-effect ion source are associated with the carbonyl group of PVP.

The observed self-assembly structure of PVP upon a-C:H/SiO_x and a-C:H:N/SiO_x direct ion beam deposition can be explained by the interaction between the ionized species in the plasma with the PVP. The plasma species incident on the growing film consists of ions and neutrals (un-dissociated precursor gas, radicals and unsaturated species) and significant amount of carrier gas, which contributes to chemical sputtering [185]. Depending on the carrier gas or mixture of carrier gases different interfacial interactions of PVP with amorphous carbon takes place during direct ion beam deposition, generating some amount of strain in the PVP. This strain induces the wrinkle formation and influences segmentalization effects and growth of amorphous carbon film. These interfacial interactions induce changes in the carbonyl group of PVP, which are dependent on the carrier gas used for direct ion beam deposition of DLC. Additionally, previous studies reported that nitrogen incorporation as a part of carrier gas results in amorphous carbon formation with more terminating groups [186]. This behavior is responsible for the different self-assembly structure of PVP after surface modification with a-C:H:N/SiO_x. Secondly, the ion beam interaction with the PVP film affects its thermal stability, which is dependent on the film thickness. Therefore, different amount of strain is generated in the PVP, which leads to changes in self-assembly structure and functional group behavior. Further, the hydrophobic nature of the amorphous carbon and different modulus of the materials [187] are also meaningful for the self-assembly mechanism.

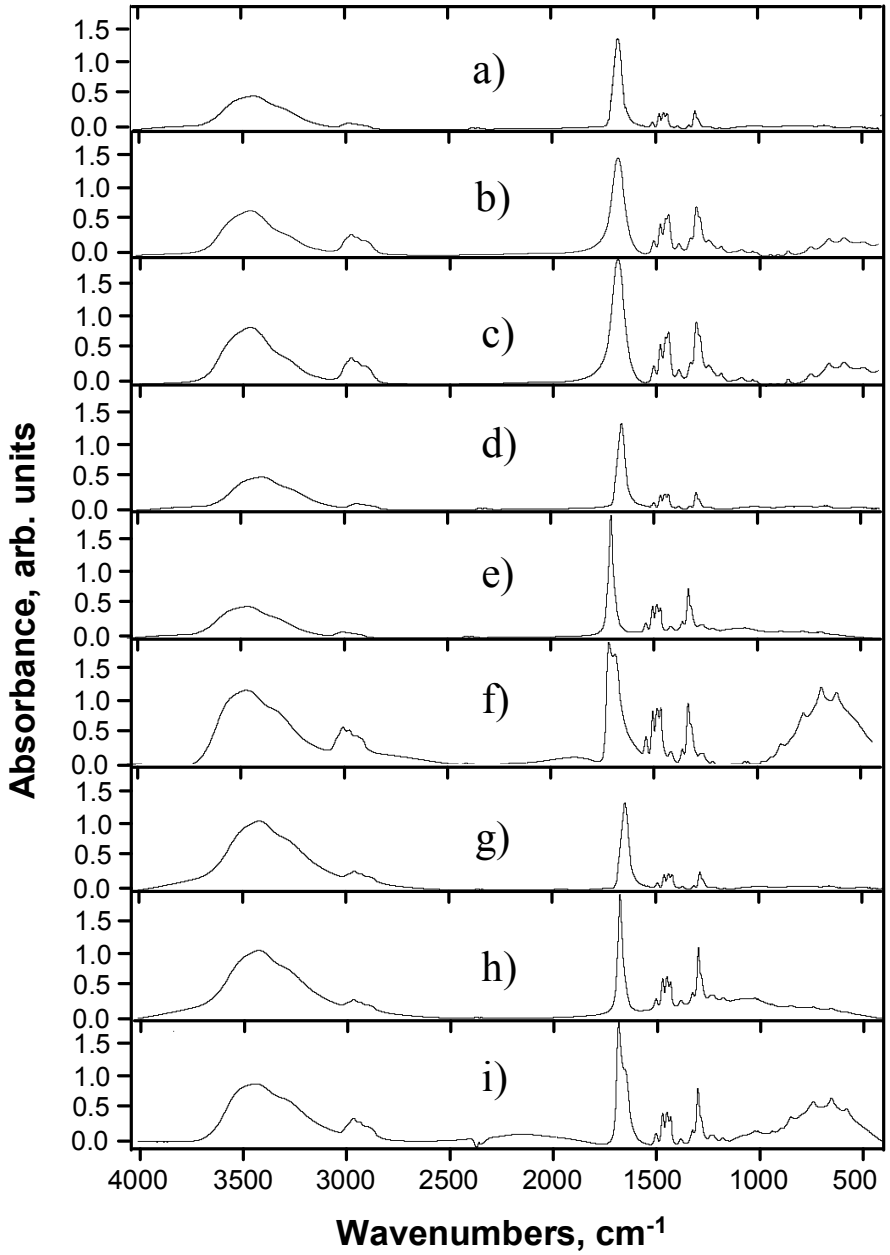

Fig. 65. Panoramic FTIR spectra of PVP5% (a), PVP10% (b) and PVP20% (c) films and a-C:H/SiOx/PVP5% (d), a-C:H/SiO_x/PVP10% (e), a-C:H/SiO_x/PVP20% (f), a-C:H:N/SiO_x/PVP5% (g), a-C:H:N/SiO_x/PVP10% (h) and a-C:H:N/SiO_x/PVP20% (i) composite films.

Table 21. Other peak assignments of the undoped DLC-PVP and nitrogen-doped DLC-PVP composite films.

Sample	Position, cm^{-1}	Probable assignment
a-C:H/SiO_x/PVP5%	1495/1462/1440/1424 2954/2926/2896 1319	C-H deformations of cyclic CH_2 groups CH and CH_2 stretch C-N stretch/C-H bend
a-C:H/SiO_x/PVP10%	1495/1463/1441/1425 2956/2927/2898 1319	C-H deformations of cyclic CH_2 groups CH and CH_2 stretch C-N stretch/C-H bend
a-C:H/SiO_x/PVP20%	1494/1462/1440/1423 2954/2925/2895 1319	C-H deformations of cyclic CH_2 groups CH and CH_2 stretch C-N stretch/C-H bend
a-C:H:N/SiO_x/PVP5%	1495/1462/1440/1424 2954/2926/2896 1319	C-H deformations of cyclic CH_2 groups CH and CH_2 stretch C-N stretch/C-H bend
a-C:H:N/SiO_x/PVP10%	1495/1463/1441/1425 2955/2925 1319	C-H deformations of cyclic CH_2 groups CH and CH_2 stretch C-N stretch/C-H bend
a-C:H:N/SiO_x/PVP20%	1495/1463/1442/1425 2955/2923/2896 1319	C-H deformations of cyclic CH_2 groups CH and CH_2 stretch C-N stretch/C-H bend

3.4 Final remarks

It was demonstrated how simple design of multilayered chromium composite films, prepared via combination of thermal evaporation technique and O_2 plasma treatment can improve the adhesion and cohesion of a film-substrate system. They showed the best scratch resistance than compared to conventional chromium films and different hydrogenated amorphous carbon films. Moreover, the composite films exhibited higher reflection values in the wavelength range of 250-800 nm, lower root-mean square roughness and more favorable surface morphology as compared with conventional films which are used for lithographic masks, glass scales and reticles. The wear rate of the composite films at the room temperature is comparable with that of the hard chromate films used to provide abrasion resistant surface. As compared with application of protective films on top of chromium film, the novel technology is more effective. It can simplify the deposition process due to the use of a single metal source. In case of lithographic mask used in contact lithography, the application of protective coating would also lower the resolution (i.e. widen the gap between the mask and substrate coated photoresist). Furthermore, O_2 plasma treatment technology can be easily integrated into the PVD process. It would be a cost-effective improvement - the whole fabrication process would be performed in a single vacuum unit. Finally, a novel chromium composite film is a strong candidate for improvement of lithographic masks, glass scales and reticles. Fig. 66 shows a prototype incremental optical scale fabricated from two-step thermally deposited chromium thin film on glass substrate. The testing of these novel composite films is

already in progress and patenting is planned when additional support will be received.

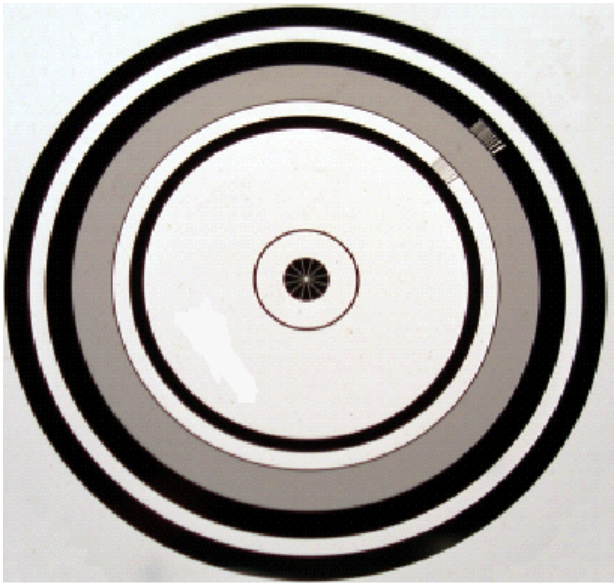

Fig. 66. The prototype incremental optical scale fabricated from the two-step thermally deposited chromium thin film on glass substrate.

The DLC-PVP composite does not fit as a protective film. However, the observed surface morphologies provide new ideas for its use. In early future the same experimental procedure will be applied on the grooved PVP surface and the self-assembly structure will be investigated at the Institute of Materials Science of Kaunas University of Technology. The goal is to obtain ordered self-assembled structure of DLC-PVP (e.g. Fig. 14). Afterwards, the new type of precision positioning scales can be developed, which would employ both imagining scanning and interferential scanning principles, so that two devices could move / position independently on a single precision scale (e.g. laser tracking system with rocket launch positioning stage).

4. CONCLUSIONS

1. Surface activation and contamination removal by O_2 plasma process and RCA-1 surface preparation method revealed the best results, where surfaces were free of hydrophobic contaminants with low contact angles ranging from 4° to 8°. Soda-lime-silica float glass surface wettability properties of both sides were equalized after bombardment in RIBE unit by Ar^+ ion beam. The oxygen plasma treatment and RCA-1 clean were effective methods for improved chromium thin film adhesive bonding to soda-lime-silica float glass substrate as confirmed by scratch tests. When combined with thermal pretreatment (100 °C) in the vacuum chamber before chromium thin film evaporation process the critical normal force for coating delamination exceeded a value of 0.2 N.
2. Chromium thin films prepared via thermal evaporation consisted of isolated surface mounds while in magnetron sputtered samples, these mounds combined to form larger islands. A lower AFM tip-sample adhesive force of 284 ± 10 nN was observed for thermally deposited chromium surfaces as compared with magnetron sputtered chromium surfaces having a value of 332 ± 17 nN. Variations in AFM tip-sample adhesive force were attributed to nanostructural differences of the films. The nanostructural differences between chromium thin films deposited using two different techniques were attributed to the C-Cr bond formation as observed in C 1s spectrum at 282.7 eV for thermally deposited chromium films and different chromium film condensation and growth mechanism as confirmed by the weak (211) reflection with 2θ at 81.7^o in magnetron sputtered samples.
3. The two-step thermal deposition of chromium thin films followed by O_2 plasma treatment after the first deposition improved adhesion and cohesion of the film-substrate system as compared with typical thin film deposition process. The cohesive failure of the multilayered chromium film influenced by more contact-wear-resistant surface morphology increased from 81 ± 8 mN to 165 ± 10 mN. Further, the adhesion to the substrate was improved and critical adhesive loads were increased from 198 ± 5 mN to 221 ± 5 mN with less eruption of the film due to multilayer boundaries.
4. The XRD analysis of two-step thermally deposited chromium film showed a well-defined body-centered cubic (110) plane of Cr metal crystal lattice structure. XPS analysis revealed a sharp doublet with Cr $2p_{3/2}$ peak at 574.2 eV due to the metallic Cr with the broad peak around 576.9 eV due to the mixed oxide and hydroxides. The Cr 2p specification remained constant throughout the etching analysis (XPS profiling), with peak due to oxides and hydroxides disappearing after the first etching cycle. Importantly, O 1s region showed presence of ~2% of oxygen within the first five etching cycles with no silicon signal (glass substrate contribution) detected, showing oxygen diffused into the Cr film.
5. The ball-on-disc experiments showed that the frictional coefficient of the two-step thermally deposited chromium films sliding against 100Cr6

and 440C balls is relatively high and stable at the room temperature. The topographical images of the wear track sections for sliding against 100Cr6 and 440C balls at room temperature revealed that the wear was governed by abrasion and fracture mechanisms. Two-step thermally deposited chromium films exhibited low wear rates at room temperature. Only the first half of the metallic chromium film was worn out after ~18 m of dry sliding at room temperature, as confirmed by the height distribution histograms, bearing ratio curves and EDS analysis. Further increase in temperature resulted in a decrease in wear resistance of the film. The cut-off point of the film was reached after ~6.2 m and ~7 m of dry sliding at 100 and 200 ºC, respectively.

6. The two-step thermally deposited chromium thin films exhibited higher reflection values over the wavelength range of 250-800 nm as compared with films deposited using conventional thermal deposition process.
7. The a-C:H/SiO_x and a-C:H:N/SiO_x films showed better mechanical strength as compared to conventional a-C:H films. The a-C:H:N/SiO_x and a-C:H/SiO_x films exhibited a fatigue and fracture induced wear mechanism while a-C:H films - additional wear due to nanostructural abrasiveness arising from the specific (sharp height distribution with higher R_{ku} and R_{pk} values) surface morphology of the film. The XPS analysis demonstrated increased amounts of silicon and the absence of terminal oxygenated carbon bonds which was attributed to the improved mechanical properties of a-C:H:N/SiO_x films.
8. The detailed AFM analysis directly showed that the a-C:H/SiO_x/PVP and a-C:H:N/SiO_x/PVP composite films represent different morphologies with characteristic surface textures. The RMS roughness for the undoped a-C:H/SiO_x/PVP and a-C:H:N/SiO_x/PVP composite films increased with PVP film thickness. With increasing PVP film thickness, a larger core-roughness parameter could be obtained after a-C:H/SiO_x and a-C:H:N/SiO_x deposition process, which indicates that higher structural uniformity of self-assembled surface structures could be tailored for the a-C:H/SiO_x/PVP and a-C:H:N/SiO_x/PVP composite films. The variance in AFM tip-sample adhesion force detected was lower for the undoped DLC-PVP compared to the nitrogen-doped DLC-PVP composite films due to lower structural homogeneity of the surfaces.
9. FTIR analysis showed that interfacial interactions of PVP with the direct ion beam induce changes in the infrared absorption features of the PVP carbonyl group and are dependent on the carrier gas used for the synthesis of the amorphous hydrogenated carbon films.

5. REFERENCES

[1] Metz, K.M.; Colavita, P.E.; Tse, K.Y.; Hamers, R.J., Nanotextured gold coatings on carbon nanofiber scaffolds as ultrahigh surface-area electrodes, *Journal of Power Sources*, 2012, vol. 198, no. p. 393-401.

[2] Ketenoğlu, D.; Ünal, B., Influence of surface roughness on the electrical conductivity of semiconducting thin films, *Physica A: Statistical Mechanics and its Applications*, 2013, vol. 392, no. 14, p. 3008-3017.

[3] Ng, V.; Hu, J.; Adeyeye, A.; Wang, J.; Chong, T., Factors affecting surface roughness and coercivity of Ni 80 Fe 20 thin films, *Journal of Applied Physics*, 2002, vol. 91, no. 10, p. 7206-7208.

[4] Rabady, R.; Avrutsky, I., Reduced surface roughness of solid thin films prepared by alternating-bias, radio-frequency magnetron sputtering, *Journal of the Optical Society of America B*, 2003, vol. 20, no. 10, p. 2174-2178.

[5] Kappl, M., Surface and interfacial forces, John Wiley & Sons, 2009.

[6] Pelliccione, M.; Lu, T.M., Evolution of Thin Film Morphology, Berlin: Springer, 2008. ISBN: 978-0-387-75108-5, 2008.

[7] Raoufi, D.; Hosseinpanahi, F., The effect of film thickness on surface morphology of ITO thin films, *Journal of Theoretical and Applied Physics*, 2013, vol. 7, no. 1, p. 1-8.

[8] Stagon, S.P.; Huang, H.; Baldwin, J.K.; Misra, A., Anomaly of film porosity dependence on deposition rate, *Applied Physics Letters*, 2012, vol. 100, no. 6, p. 061601.

[9] Lu, T.M.; Zhao, Y.P.; Drotar, J.; Karabacak, T.; Wang, G.C., Novel mechanisms on the growth morphology of films, in: MRS Proceedings, Cambridge Univ Press, 2002.

[10] Lakhtakia, A.; Messier, R., Sculptured Thin Films: Nanoengineered Morphology and Optics, SPIE press Bellingham, WA, 2005.

[11] Cartwright, J.H.; Escribano, B.; Sainz-Díaz, C.I., Ice films follow structure zone model morphologies, *Thin Solid Films*, 2010, vol. 518, no. 12, p. 3422-3427.

[12] Messier, R.; Venugopal, V.C.; Sunal, P.D., Origin and evolution of sculptured thin films, *Journal of Vacuum Science & Technology A*, 2000, vol. 18, no. 4, p. 1538-1545.

[13] Besnard, A.; Martin, N.; Carpentier, L., Three-dimensional growth simulation: A study of substrate oriented films, in: IOP Conference Series: Materials Science and Engineering, IOP Publishing, 2010, p. 012011.

[14] Javadi, S.; Ghoranneviss, M.; Hojabri, A.; Habibi, M.; Hosseinnejad, M., Deposition of chromium thin films on stainless steel-304 substrates using a low energy plasma focus device, *Journal of Fusion Energy*, 2012, vol. 31, no. 3, p. 242-248.

[15] Seok, J.; Jadeed, N.; Lin, R., Sputter-deposited nanocrystalline Cr and CrN coatings on steels, *Surface and Coatings Technology*, 2001, vol. 138, no. 1, p. 14-22.

[16] Schwenke, H.; Neuschaefer-Rube, U.; Pfeifer, T.; Kunzmann, H., Optical methods for dimensional metrology in production engineering, *CIRP Annals-Manufacturing Technology*, 2002, vol. 51, no. 2, p. 685-699.

[17] Gibb, H.J.; Lees, P.S.; Pinsky, P.F.; Rooney, B.C., Lung cancer among workers in chromium chemical production, *American Journal of Industrial Medicine*, 2000, vol. 38, no. 2, p. 115-126.

[18] Navinšek, B.; Panjan, P.; Milošev, I., PVD coatings as an environmentally clean alternative to electroplating and electroless processes, *Surface and Coatings Technology*, 1999, vol. 116, no. p. 476-487.

[19] Gautier, C.; Machet, J., Effects of deposition parameters on the texture of chromium films deposited by vacuum arc evaporation, *Thin Solid Films*, 1996, vol. 289, no. 1, p. 34-38.

[20] Kulkarni, A.; Chang, L., Electrical and structural characteristics of chromium thin films deposited on glass and alumina substrates, *Thin Solid Films*, 1997, vol. 301, no. 1, p. 17-22.
[21] Lousa, A.; Romero, J.; Martınez, E.; Esteve, J.; Montala, F.; Carreras, L., Multilayered chromium/chromium nitride coatings for use in pressure die-casting, *Surface and Coatings Technology*, 2001, vol. 146, no. p. 268-273.
[22] Kim, P., CoCrTa thin films for magnetic recording media, dissertation, University of Twente, 1999, p. 116-126.
[23] Balu, R.; Raju, A.; Lakshminarayanan, V.; Mohan, S., Investigations on the influence of process parameters on the structural evolution of ion beam sputter deposited chromium thin films, *Materials Science and Engineering: B*, 2005, vol. 123, no. 1, p. 7-12.
[24] Abu-Shgair, K.; Abu-Safe, H.H.; Aryasomayajula, A.; Beake, B.; Gordon, M.H., Characterizing crystalline chromium oxide thin film growth parameters, *Reviews on Advanced Materials Science*, 2010, vol. 24, no. p. 64-68.
[25] Frost, R.L.; Martens, W.N.; Yang, J.; Cheng, H., Transition of synthetic chromium oxide gel to crystalline chromium oxide: a hot stage Raman spectroscopic study, *Journal of Raman Spectroscopy*, 2010, vol. 42 no. 5 p. 1069–1074.
[26] Bannai, E., Sphere Packings, Lattices and Groups, Springer, 1999.
[27] Zhang, L.; Kuhn, M.; Diebold, U., Epitaxial growth of ultrathin films of chromium and its oxides on Pt (111), *Journal of Vacuum Science & Technology A*, 1997, vol. 15, no. 3, p. 1576-1580.
[28] Stierle, A.; Zabel, H., Kinetics of Cr_2O_3 growth during the oxidation of Cr (110), *Europhysics Letters*, 1997, vol. 37, no. 5, p. 365.
[29] Arellano, G., Geometric structure and desorption kinetics of CO on the Cr_2O_3 (0001)/Cr (110) Surface, dissertation, Texas State University, 2010.
[30] Jukna, T.; Baltrušaitis, J.; Sinkevičius, V.; Viržonis, D., A thin chromium film formation monitoring method: Monitoring of the early stages, *Thin Solid Films*, 2008, vol. 516, no. 10, p. 2943-2947.
[31] Lintymer, J.; Gavoille, J.; Martin, N.; Takadoum, J., Glancing angle deposition to modify microstructure and properties of sputter deposited chromium thin films, *Surface and Coatings Technology*, 2003, vol. 174, no. p. 316-323.
[32] Agarwal, S.; Jain, A.; Lal, C.; Ganesan, V.; Jain, I., Surface morphology and the phase formation at Cr/Si system, *Applied Surface Science*, 2007, vol. 253, no. 10, p. 4721-4726.
[33] Wang, J.; Griffis, D.; Garcia, R.; Russell, P., Etching characteristics of chromium thin films by an electron beam induced surface reaction, *Semiconductor Science and Technology*, 2003, vol. 18, no. 4, p. 199.
[34] Manier, C.; Spaltmann, D.; Woydt, M., Tribology of DLC films under slip-rolling conditions, in: Tribology of Diamond-Like Carbon Films, Springer, 2008, pp. 383-409.
[35] Permyakov, V.; Proleeva, Y.N., Electrical properties and structure of thin chromium films, *Soviet Physics Journal*, 1971, vol. 14, no. 9, p. 1207-1210.
[36] Baird, R.; Haeberle, R., The effect of alkali ion migration on the adhesion of sputtered chromium metallizations to glass, *Journal of Vacuum Science & Technology A*, 1986, vol. 4, no. 3, p. 532-535.
[37] Wei, G.; Scharf, T.; Zhou, J.; Huang, F.; Weaver, M.; Barnard, J., Nanotribology studies of Cr, Cr_2N and CrN thin films using constant and ramped load nanoscratch techniques, *Surface and Coatings Technology*, 2001, vol. 146, no. p. 357-362.
[38] Robertson, J., Diamond-like amorphous carbon, *Materials Science and Engineering: R: Reports*, 2002, vol. 37, no. 4, p. 129-281.
[39] Robertson, J., Amorphous carbon, *Advances in Physics*, 1986, vol. 35, no. 4, p. 317-374.
[40] Ferrari, A.C., Non-destructive characterisation of carbon films, in: Tribology of Diamond-Like Carbon Films, Springer, 2008, p. 25-82.

[41] Ahmed, S.F.; Banerjee, D.; Chattopadhyay, K., The influence of fluorine doping on the optical properties of diamond-like carbon thin films, *Vacuum*, 2010, vol. 84, no. 6, p. 837-842.
[42] Jones, B.; Mahendran, A.; Anson, A.; Reynolds, A.; Bulpett, R.; Franks, J., Diamond-like carbon coating of alternative metal alloys for medical and surgical applications, *Diamond and Related Materials*, 2010, vol. 19, no. 7, p. 685-689.
[43] Roy, R.K.; Choi, H.W.; Yi, J.W.; Moon, M.W.; Lee, K.R.; Han, D.K.; Shin, J.H.; Kamijo, A.; Hasebe, T., Hemocompatibility of surface-modified, silicon-incorporated, diamond-like carbon films, *Acta Biomaterialia*, 2009, vol. 5, no. 1, p. 249-256.
[44] Yokota, T.; Terai, T.; Kobayashi, T.; Meguro, T.; Iwaki, M., Cell adhesion to nitrogen-doped DLCs fabricated by plasma-based ion implantation and deposition method using toluene gas, *Surface and Coatings Technology*, 2007, vol. 201, no. 19, p. 8048-8051.
[45] Ikeyama, M.; Nakao, S.; Miyagawa, Y.; Miyagawa, S., Effects of Si content in DLC films on their friction and wear properties, *Surface and Coatings Technology*, 2005, vol. 191, no. 1, p. 38-42.
[46] Liu, Y.; Erdemir, A.; Meletis, E., An investigation of the relationship between graphitization and frictional behavior of DLC coatings, *Surface and Coatings Technology*, 1996, vol. 86, no. p. 564-568.
[47] Hauert, R., A review of modified DLC coatings for biological applications, *Diamond and Related Materials*, 2003, vol. 12, no. 3, p. 583-589.
[48] Maguire, P.; McLaughlin, J.; Okpalugo, T.; Lemoine, P.; Papakonstantinou, P.; McAdams, E.; Needham, M.; Ogwu, A.; Ball, M.; Abbas, G., Mechanical stability, corrosion performance and bioresponse of amorphous diamond-like carbon for medical stents and guidewires, *Diamond and Related Materials*, 2005, vol. 14, no. 8, p. 1277-1288.
[49] Mitura, E.; Mitura, S.; Niedzielski, P.; Has, Z.; Wolowiec, R.; Jakubowski, A.; Szmidt, J.; Sokołowska, A.; Louda, P.; Marciniak, J., Diamond-like carbon coatings for biomedical applications, *Diamond and Related Materials*, 1994, vol. 3, no. 4, p. 896-898.
[50] Lin, C.; Wei, D.; Chang, C.; Liao, W., Optical properties of diamond-like carbon films for antireflection coating by RF magnetron sputtering method, *Physics Procedia*, 2011, vol. 18, no. p. 46-50.
[51] Litovchenko, V.; Klyui, N., Solar cells based on DLC film–Si structures for space application, *Solar Energy Materials and Solar Cells*, 2001, vol. 68, no. 1, p. 55-70.
[52] Bhushan, B.; Sundararajan, S., Micro/nanoscale friction and wear mechanisms of thin films using atomic force and friction force microscopy, *Acta Materialia*, 1998, vol. 46, no. 11, p. 3793-3804.
[53] Gupta, B.; Bhushan, B., Micromechanical properties of amorphous carbon coatings deposited by different deposition techniques, *Thin Solid Films*, 1995, vol. 270, no. 1, p. 391-398.
[54] Kim, Y.; Cho, S.; Choi, W.; Hong, B.; Yoon, D., Dependence of the bonding structure of DLC thin films on the deposition conditions of PECVD method, *Surface and Coatings Technology*, 2003, vol. 169, no. p. 291-294.
[55] Meškinis, Š.; Gudaitis, R.; Kopustinskas, V.; Tamulevičius, S., Electrical and piezoresistive properties of ion beam deposited DLC films, *Applied Surface Science*, 2008, vol. 254, no. 16, p. 5252-5256.
[56] Tamulevičienė, A.; Meškinis, Š.; Kopustinskas, V.; Tamulevičius, S., Diamond like carbon film as potential antireflective coating for silicon solar cells, *Materials Science= Medžiagotyra/Kaunas University of Technology, Academy of Sciences of Lithuania. Kaunas: Technologija. ISSN*, 2010, vol. no. p. 1392-1320.
[57] Tamulevičienė, A.; Meškinis, Š.; Kopustinskas, V.; Tamulevičius, S., Carrier gas and ion beam parameter effects on the structure and properties of aC:H/SiO_x films deposited

employing closed drift ion beam source, *Nuclear Instruments and Methods in Physics Research Section B: Beam Interactions with Materials and Atoms*, 2012, vol. 282, p. 116-120.
[58] Pauleau, Y., Residual stresses in DLC films and adhesion to various substrates, in: Tribology of Diamond-Like Carbon Films, Springer, 2008, p. 102-136.
[59] Wei, C.;Yen, J.-Y., Effect of film thickness and interlayer on the adhesion strength of diamond like carbon films on different substrates, *Diamond and Related Materials*, 2007, vol. 16, no. 4, p. 1325-1330.
[60] Funada, Y.; Awazu, K.; Yasui, H.; Sugita, T., Evaluation of raw hardness of DLC thin films prepared by IBAD, *Nuclear Instruments and Methods in Physics Research Section B: Beam Interactions with Materials and Atoms*, 1999, vol. 148, no. 1, p. 664-668.
[61] Turri, R.G.; Santos, R.M.; Rangel, E.C.; da Cruz, N.C.; Bortoleto, J.R.; Dias da Silva, J.H.; Antonio, C.A.; Durrant, S.F., Optical, mechanical and surface properties of amorphous carbonaceous thin films obtained by plasma enhanced chemical vapor deposition and plasma immersion ion implantation and deposition, *Applied Surface Science*, 2013, vol. 280, no. p. 474-481.
[62] Liu, D.; Benstetter, G.; Liu, Y.; Zhang, J.; Ren, C.; Ma, T., Surface roughness, scratch resistance and tribological properties of hydrogenated amorphous carbon coatings prepared by low-pressure dielectric barrier discharge, *Surface and Coatings Technology*, 2003, vol. 174, p. 310-315.
[63] Hasebe, T.; Nagashima, S.; Yoshimoto, Y.; Hotta, A.; Suzuki, T., Tailoring surface topographies of polymers by using ion beam: Recent advances and the potential applications in biomedical and tissue engineering, *Nuclear Instruments and Methods in Physics Research Section B: Beam Interactions with Materials and Atoms*, 2012, vol. 282, no. p. 134-136.
[64] Guan, L.; Peng, K.; Yang, Y.; Qiu, X.; Wang, C., The nanofabrication of polydimethylsiloxane using a focused ion beam, *Nanotechnology*, 2009, vol. 20, no. 14, p. 145301.
[65] Moon, M.W.; Han, J.H.; Vaziri, A.; Her, E.K.; Oh, K.H.; Lee, K.R.; Hutchinson, J.W., Nanoscale ripples on polymers created by a focused ion beam, *Nanotechnology*, 2009, vol. 20, no. 11, p. 115301.
[66] Netcheva, S.; Bertrand, P., Ion-beam-induced morphology on the surface of thin polymer films at low current density and high ion fluence, *Journal of Polymer Science Part B: Polymer Physics*, 2001, vol. 39, no. 3, p. 314-325.
[67] Asakawa, R.; Nagashima, S.; Nakamura, Y.; Hasebe, T.; Suzuki, T.; Hotta, A., Combining polymers with diamond-like carbon (DLC) for highly functionalized materials, *Surface and Coatings Technology*, 2011, vol. 206, no. 4, p. 676-685.
[68] Hotta, A.; Hasebe, T., Diamond-like carbon coated on polymers for biomedical applications, in: Thin Films and Coatings in Biology, Springer, 2013, pp. 171-228.
[69] Shirakura, A.; Nakaya, M.; Koga, Y.; Kodama, H.; Hasebe, T.; Suzuki, T., Diamond-like carbon films for PET bottles and medical applications, *Thin Solid Films*, 2006, vol. 494, no. 1, p. 84-91.
[70] Anttila, A.; Tiainen, V.M.; Kiuru, M.; Alakoski, E.; Arstila, K., Preparation of diamond-like carbon polymer hybrid films using filtered pulsed arc discharge method, *Surface Engineering*, 2003, vol. 19, no. 6, p. 425-428.
[71] Nagashima, S.; Hasebe, T.; Tsuya, D.; Horikoshi, T.; Ochiai, M.; Tanigawa, S.; Koide, Y.; Hotta, A.; Suzuki, T., Controlled formation of wrinkled diamond-like carbon (DLC) film on grooved poly (dimethylsiloxane) substrate, *Diamond and Related Materials*, 2012, vol. 22, no. p. 48-51.
[72] Haaf, F.; Sanner, A.; Straub, F., Polymers of N-vinylpyrrolidone: synthesis, characterization and uses, *Polymer Journal*, 1985, vol. 17, no. 1, p. 143-152.

[73] Guowei, D.; Adriane, K.; Chen, X.; Jie, C.; Yinfeng, L., PVP magnetic nanospheres: Biocompatibility, in vitro and in vivo bleomycin release, *International Journal of Pharmaceutics*, 2007, vol. 328, no. 1, p. 78-85.
[74] Montezuma, S.R.; Loewenstein, J.; Scholz, C.; Rizzo, J.F., Biocompatibility of materials implanted into the subretinal space of Yucatan pigs, *Investigative Ophthalmology & Visual Science*, 2006, vol. 47, no. 8, p. 3514-3522.
[75] Takeda, S., Oxygen and silver diffusion into float glass, *Journal of Non-crystalline Solids*, 2006, vol. 352, no. 36, p. 3910-3913.
[76] Fernández Oro, J.; Argüelles Díaz, K.; Santolaria Morros, C.; Cobo Hedilla, A.; Lemaille, M., Multiphase modelling of pouring glass over the spout lip of an industrial float in the flat glass forming process, *International Journal for Numerical Methods in Fluids*, 2008, vol. 58, no. 10, p. 1147-1177.
[77] Zhang, Q.; Chen, Z.; Li, Z., Simulation of tin penetration in the float glass process (float glass tin penetration), *Applied Thermal Engineering*, 2011, vol. 31, no. 6, p. 1272-1278.
[78] Kolluru, P.V.; Green, D.J.; Pantano, C.G.; Muhlstein, C.L., Effects of surface chemistry on the nanomechanical properties of commercial float glass, *Journal of the American Ceramic Society*, 2010, vol. 93, no. 3, p. 838-847.
[79] Goodman, O.; Derby, B., The mechanical properties of float glass surfaces measured by nanoindentation and acoustic microscopy, *Acta Materialia*, 2011, vol. 59, no. 4, p. 1790-1799.
[80] Seward III, T.P., High Temperature Glass Melt Property Database For Process Modeling, Author: Thomas P. Seward III, Terese Vascott, 2005.
[81] Pulker, H.;Pulker, H., Coatings on Glass, Elsevier, 1999.
[82] Awadelkarim, O.; Wang, Y., The impact of RCA treatment of glass substrates on the properties of polycrystalline silicon thin film transistors, *Microelectronic engineering*, 1999, vol. 45, no. 4, p. 299-310.
[83] Müller-Buschbaum, P., Influence of surface cleaning on dewetting of thin polystyrene films, *The European Physical Journal E*, 2003, vol. 12, no. 3, p. 443-448.
[84] Guha, A.; Barron, R.M.; Balachandar, R., An experimental and numerical study of water jet cleaning process, *Journal of Materials Processing Technology*, 2011, vol. 211, no. 4, p. 610-618.
[85] Bhattacharya, S.; Datta, A.; Berg, J.M.; Gangopadhyay, S., Studies on surface wettability of poly (dimethyl) siloxane (PDMS) and glass under oxygen-plasma treatment and correlation with bond strength, *Microelectromechanical Systems, Journal of*, 2005, vol. 14, no. 3, p. 590-597.
[86] Fridman, A., Plasma Chemistry, Cambridge University Press, 2008.
[87] Mattox, D.M., Handbook of Physical Vapor Deposition (PVD) Processing, William Andrew, 2010.
[88] Wu, X.; Lai, F.; Lin, L.; Lv, J.; Zhuang, B.; Yan, Q.; Huang, Z., Optical inhomogeneity of ZnS films deposited by thermal evaporation, *Applied Surface Science*, 2008, vol. 254, no. 20, p. 6455-6460.
[89] George, J., Preparation of Thin Films, CRC Press, 1992.
[90] Lakhtakia, A.; Martin-Palma, R.J., Engineered Biomimicry, Newnes, 2013.
[91] Reddy, K.V.S.; Subramanyam, T.; Uthanna, S., Nitrogen partial pressure influence on physical properties of DC magnetron sputtered copper nitride films, *Optoelectronics and Advanced Materials*, 2007, vol. 1, no. p. 31-35.
[92] Kelly, P.; Arnell, R., Magnetron sputtering: a review of recent developments and applications, *Vacuum*, 2000, vol. 56, no. 3, p. 159-172.
[93] Ohring, M., Materials Science of Thin Films, Academic press, 2001.

[94] Kimock, F.; Finke, S.; Brown, D.; Thear, E., The evolution of ion-beam diamond-like-carbon technology into data storage: space propulsion, sunglasses, slides, and new disks, *DataTech Magazine*, 1999, p. 69-77.
[95] Kaufman, H.R., Broad-beam ion sources, *Review of Scientific Instruments*, 1990, vol. 61, no. 1, p. 230.
[96] Zhurin, V., Industrial Ion Sources: Broad Beam Gridless Ion Source Technology, Wiley-VCH Verlag GmbH & Co. KGaA, 2012.
[97] Tamulevičienė, A.; Meškinis, Š.; Kopustinskas, V.; Tamulevičius, S., Multilayer amorphous hydrogenated carbon (aC:H) and SiO_x doped aC:H films for optical applications, *Thin Solid Films*, 2011, vol. 519, no. 12, p. 4004-4007.
[98] Donnet, C.; Erdemir, A., Tribology of Diamond-like Carbon films: Fundamentals and Applications, Springer New York, 2008.
[99] Noh, B.; Jo, J.; Jung, S., Effect of atmospheric-pressure plasma treatment on the adhesion characteristics of a flexible copper clad laminate, *Journal of the Korean Physical Society*, 2009, vol. 54, no. 3, p. 1217-1222.
[100] Lee, H.; Park, S.H.; Park, Y.K.; Kim, B.H.; Kim, S.J.; Jung, S.C., Rapid destruction of the rhodamine B using TiO_2 photocatalyst in the liquid phase plasma, *Chemistry Central Journal*, 2013, vol. 7, no. 1, p. 156.
[101] Mayer, T.; Barker, R.; Whitman, L., Investigation of plasma etching mechanisms using beams of reactive gas ions, *Journal of Vacuum Science and Technology*, 1981, vol. 18, no. 2, p. 349-352.
[102] Herminghaus, S., Wetting: introductory note, *Journal of Physics: Condensed Matter*, 2005, vol. 17, no. 9, p. S261.
[103] Young, T., An essay on the cohesion of fluids, *Philosophical Transactions of the Royal Society of London*, 1805, vol. 95, no. p. 65-87.
[104] Cras, J.; Rowe-Taitt, C.; Nivens, D.; Ligler, F., Comparison of chemical cleaning methods of glass in preparation for silanization, *Biosensors and Bioelectronics*, 1999, vol. 14, no. 8, p. 683-688.
[105] Stalder, A.; Kulik, G.; Sage, D.; Barbieri, L.; Hoffmann, P., A snake-based approach to accurate determination of both contact points and contact angles, *Colloids and Surfaces A: Physicochemical and Engineering Aspects*, 2006, vol. 286, no. 1, p. 92-103.
[106] Butt, H.J.; Cappella, B.; Kappl, M., Force measurements with the atomic force microscope: Technique, interpretation and applications, *Surface Science Reports*, 2005, vol. 59, no. 1, p. 1-152.
[107] Suslov, A.A., Shasholko, D.I., Atomic Force Microscope NT-206: Operating Manual, Gomel: Microtestmachines Co., 2004.
[108] Jalili, N.; Laxminarayana, K., A review of atomic force microscopy imaging systems: application to molecular metrology and biological sciences, *Mechatronics*, 2004, vol. 14, no. 8, p. 907-945.
[109] Sebastian, A.; Salapaka, M.; Chen, D.; Cleveland, J., Harmonic analysis based modeling of tapping-mode AFM, in: Proceedings of the American Control Conference, 1999, pp. 232-236.
[110] Pimpang, P.; Zoolfakar, A.S.; Wongratanaphisan, D.; Gardchareon, A.; Nguyen, E.P.; Zhuiykov, S.; Choopun, S.; Kalantar-zadeh, K., Atomic force microscopy adhesion mapping: Revealing assembly process in inorganic systems, *The Journal of Physical Chemistry C*, 2013, vol. 117, no. 39, p. 19984-19990.
[111] Sedlaček, M.; Silva Vilhena, L.M.; Podgornik, B.; Vižintin, J., Surface topography modelling for reduced friction, *Strojniški vestnik-Journal of Mechanical Engineering*, 2011, vol. 57, no. 9, p. 674-680.
[112] Ramesh, K.T., Nanomaterials, Springer, 2009.

[113] Everhart, T.; Thornley, R., Wide-band detector for micro-microampere low-energy electron currents, *Journal of Scientific Instruments*, 1960, vol. 37, no. 7, p. 246.
[114] Ngo, P.D., Energy dispersive spectroscopy, in: Failure Analysis of Integrated Circuits, Springer, 1999, pp. 205-215.
[115] Marshall, J.M.; Dimova-Malinovska, D., Photovoltaic and Photoactive Materials-properties, Technology and Applications, Springer, 2002.
[116] Totten, G.E.; Liang, H., Surface Modification and Mechanisms: Friction, Stress, and Reaction Engineering, CRC Press, 2004.
[117] Blasco, T.; Camblor, M.; Fierro, J.; Perez-Pariente, J., X-Ray photoelectron spectroscopy of Ti-Beta zeolite, *Microporous Materials*, 1994, vol. 3, no. 3, p. 259-263.
[118] Ade, H.; Kirz, J.; Hulbert, S.L.; Johnson, E.D.; Anderson, E.; Kern, D., X-ray spectromicroscopy with a zone plate generated microprobe, *Applied physics letters*, 1990, vol. 56, no. 19, p. 1841-1843.
[119] Leon, A., Hydrogen Technology: Mobile and Portable Applications, Springer, 2008.
[120] Yoshizawa, T., Handbook of Optical Metrology: Principles and Applications, CRC Press, 2009.
[121] Griffiths, P.; De Haseth, J.A., Fourier Transform Infrared Spectrometry, John Wiley & Sons, 2007.
[122] Stuart, B.H., Analytical Techniques in Materials Conservation, John Wiley & Sons, 2007.
[123] Hunger, M.; Weitkamp, J., In situ IR, NMR, EPR, and UV/Vis spectroscopy: Tools for new insight into the mechanisms of heterogeneous catalysis, *Angewandte Chemie International Edition*, 2001, vol. 40, no. 16, p. 2954-2971.
[124] Amendola, V.; Meneghetti, M., Size evaluation of gold nanoparticles by UV-vis spectroscopy, *The Journal of Physical Chemistry C*, 2009, vol. 113, no. 11, p. 4277-4285.
[125] Rother, M.; Albus, D.; Piecha, S., UV/Vis/NIR Spectrometry for the Film Thickness Determination of Transparent Films and Layers, analytica-world, 2012.
[126] Bain, G.; Allen, M.; Keppy, N., Application Note: 51860, Thermo Fisher Scientific, Madison, WI, USA, in, 2009.
[127] Consiglio, R.; Randall, N.; Bellaton, B.; Von Stebut, J., The nano-scratch tester (NST) as a new tool for assessing the strength of ultrathin hard coatings and the mar resistance of polymer films, *Thin Solid Films*, 1998, vol. 332, no. 1, p. 151-156.
[128] Randall, N.; Favaro, G.; Frankel, C., The effect of intrinsic parameters on the critical load as measured with the scratch test method, *Surface and Coatings Technology*, 2001, vol. 137, no. 2, p. 146-151.
[129] Muller, B.; Poth, U., Coatings Formulation, Vincentz, Hannover, 2006.
[130] Ebner, E., NST Technical Features, CSM instruments, 2014.
[131] Buijnsters, J.G.; Shankar, P.; van Enckevort, W.; Schermer, J.; ter Meulen, J., Adhesion analysis of polycrystalline diamond films on molybdenum by means of scratch, indentation and sand abrasion testing, *Thin Solid Films*, 2005, vol. 474, no. 1, p. 186-196.
[132] Ponelytė, S.; Prosyčevas, I.; Guobienė, A.; Balčiūnas, R.;Puišo, J., Formation of MEMS nanocomposit layers and investigation of their mechanical properties, *Mechanika*, 2009, vol. 2, no. 76, p. 77-82.
[133] Nair, R.P.; Griffin, D.; Randall, N.X., The use of the pin-on-disk tribology test method to study three unique industrial applications, *Wear*, 2009, vol. 267, no. 5, p. 823-827.
[134] Safonov, V.; Zykova, A.; Smolik, J.; Rogovska, R.; Donkov, N.; Georgieva, V., The surface parameters modifications at nano scale for biomedical applications, in: Journal of Physics: Conference Series, IOP Publishing, 2010, pp. 012068.

[135] Chi, F.; Jiang, K.; Li, B.; Jiang, B., Properties of electroless Ni–P deposition of glass substrates using a mercapto organosilanes for functional groups to graft palladium, *Applied Surface Science*, 2008, vol. 255, no. 5, p. 2740-2745.
[136] Xianhua, C.; Tao, B.; Ju, W.; Liang, W., Characterization and tribological investigation of self-assembled lanthanum-based thin films on glass substrates, *Wear*, 2006, vol. 260, no. 7, p. 745-750.
[137] Eske, L.D.; Galipeau, D.W., Characterization of SiO_2 surface treatments using AFM, contact angles and a novel dewpoint technique, *Colloids and Surfaces A: Physicochemical and Engineering Aspects*, 1999, vol. 154, no. 1–2, p. 33-51.
[138] Lim, K.B.; Lee, D.C., Surface modification of glass and glass fibres by plasma surface treatment, *Surface and Interface Analysis*, 2004, vol. 36, no. 3, p. 254-258.
[139] Takeda, S.; Yamamoto, K.; Hayasaka, Y.; Matsumoto, K., Surface OH group governing wettability of commercial glasses, *Journal of Non-crystalline Solids*, 1999, vol. 249, no. 1, p. 41-46.
[140] Chopinet, M.H.; Gouillart, E.; Papin, S.; Toplis, M.J., Influence of limestone grain size on glass homogeneity, *Glass Technology-European Journal of Glass Science and Technology Part A*, 2010, vol. 51, no. 3, p. 116-122.
[141] Impoco, G.; Carrato, S.; Caccamo, M.; Tuminello, L.; Licitra, G., Image analysis methods for industrial application, in: Samuele, B. (Ed.) Proceedings of SIMAI, Italy, 2006, pp. 22-26.
[142] Tayebi, N.; Polycarpou, A., Adhesion and contact modeling and experiments in microelectromechanical systems including roughness effects, *Microsystem technologies*, 2006, vol. 12, no. 9, p. 854-869.
[143] Stegemann, B.; Backhaus, H.; Kloss, H.; Santner, E., Spherical AFM probes for adhesion force measurements on metal single crystals, *Modern Research and Educational Topics in Microscopy, Series*, 2007, vol. 3, no. p. 820-827.
[144] Biesinger, M.; Brown, C.; Mycroft, J.; Davidson, R.; McIntyre, N., X-ray photoelectron spectroscopy studies of chromium compounds, *Surface and Interface Analysis*, 2004, vol. 36, no. 12, p. 1550-1563.
[145] Andrulevičius, M.; Tamulevičius, S.; Gnatyuk, Y.; Vityuk, N.; Smirnova, N.; Eremenko, A., XPS investigation of $TiO_2/ZrO_2/SiO_2$ films modified with Ag/Au nanoparticles, *Materials Science= Medžiagotyra/Kaunas University of Technology*, 2008, vol. 14, no. 1, p. 8-14
[146] Bertóti, I.; Mohai, M.; Kereszturi, K.; Tóth, A.; Kálmán, E., Carbon based Si-and Cr-containing thin films: Chemical and nanomechanical properties, *Solid State Sciences*, 2009, vol. 11, no. 10, p. 1788-1792.
[147] Edigaryan, A.; Safonov, V.; Lubnin, E.; Vykhodtseva, L.; Chusova, G.; Polukarov, Y.M., Properties and preparation of amorphous chromium carbide electroplates, *Electrochimica acta*, 2002, vol. 47, no. 17, p. 2775-2786.
[148] Wagner, C.; Powell, C. J.; Allison, J.; Rumble, J., NIST X-ray Photoelectron Spectroscopy Database (Version 2.0), Retrieved from NIST Standard Reference Data Program website: http://www.nist.gov/srd, 1997.
[149] Uchida, E.; Iwata, H.; Ikada, Y., Surface structure of poly (ethylene terephthalate) film grafted with poly (methacrylic acid), *Polymer*, 2000, vol. 41, no. 10, p. 3609-3614.
[150] Meskinis, S.; Andrulevicius, M.; Kopustinskas, V.; Tamulevicius, S., XPS study of the ultrathin aC:H films deposited onto ion beam nitrided AISI 316 steel, *Applied Surface Science*, 2005, vol. 249, no. 1, p. 295-302.
[151] Feng, Z.; Rohatgi, A.; Tin, C.; Hu, R.; Wee, A.; Se, K., Structural, optical, and surface science studies of 4H-SiC epilayers grown by low pressure chemical vapor deposition, *Journal of Electronic Materials*, 1996, vol. 25, no. 5, p. 917-923.

[152] Jordan, J.; Sanda, P.; Morar, J.; Kovac, C.; Himpsel, F.; Pollak, R., Synchrotron radiation excited carbon 1s photoemission study of Cr/organic polymer interfaces, *Journal of Vacuum Science & Technology A: Vacuum, Surfaces, and Films*, 1986, vol. 4, no. 3, p. 1046-1048.
[153] Pang, X.; Gao, K.; Volinsky, A.A., Microstructure and mechanical properties of chromium oxide coatings, *Journal of Materials Research*, 2007, vol. 22, no. 12, p. 3531.
[154] Thurner, G.; Abermann, R., A study of O_2 and CO adsorption on thin evaporated chromium films, *Journal of Vacuum Science & Technology A: Vacuum, Surfaces, and Films*, 1987, vol. 5, no. 4, p. 1635-1639.
[155] Watari, F., Detection of protective oxide layers on Cr formed by exposure to air by STEM-ELS method, *Surface Science*, 1981, vol. 110, no. 1, p. 111-119.
[156] Mulloni, V.; Bartali, R.; Colpo, S.; Giacomozzi, F.; Laidani, N.; Margesin, B., Electrical and mechanical properties of layered gold–chromium thin films for ohmic contacts in RF-MEMS switches, *Materials Science and Engineering: B*, 2009, vol. 163, no. 3, p. 199-203.
[157] Al-Kuhaili, M.; Durrani, S., Optical properties of chromium oxide thin films deposited by electron-beam evaporation, *Optical Materials*, 2007, vol. 29, no. 6, p. 709-713.
[158] Barshilia, H.C.; Rajam, K., Growth and characterization of chromium oxide coatings prepared by pulsed-direct current reactive unbalanced magnetron sputtering, *Applied Surface Science*, 2008, vol. 255, no. 5, p. 2925-2931.
[159] Hong, S.; Kim, E.; Kim, D.W.; Sung, T.H.; No, K., On measurement of optical band gap of chromium oxide films containing both amorphous and crystalline phases, *Journal of Non-crystalline Solids*, 1997, vol. 221, no. 2, p. 245-254.
[160] Huang, M.; Ladwig, P.F.; Austin C.Y., Phase transformations in sputter deposited NiMn thin films, *Thin Solid Films*, 2005, vol. 478, no. 1, p. 137-140.
[161] Biesinger, M.C.; Payne, B.P.; Grosvenor, A.P.; Lau, L.W.; Gerson, A.R.; Smart, R.S.C., Resolving surface chemical states in XPS analysis of first row transition metals, oxides and hydroxides: Cr, Mn, Fe, Co and Ni, *Applied Surface Science*, 2011, vol. 257, no. 7, p. 2717-2730.
[162] Miyagawa, Y.; Miyagawa, S., Dynamic Monte Carlo simulation of surface composition change during sputter depth profiling, *Nuclear Instruments and Methods in Physics Research Section B: Beam Interactions with Materials and Atoms*, 2002, vol. 190, no. 1, p. 256-260.
[163] Facchini, D.; Mahalanobis, N.; Gonzalez, F.; Palumbo, G., Electrodeposition of nanocrystalline cobalt alloy coatings as a hard chrome alternative, in: DoD Corrosion Conference, 2009, pp. 1-13.
[164] Moline, A.; Yager, M.; Juliana, G.S.; Mahalanobis, N.; Facchini, D.; Gonzalez, F.; Tomantschger, K., Industrial implementation of nanostructured cobalt-phosphorus coatings at Enduro Industries LLC, *Proc. SUR/FIN 2011, Rosemont IL, June 13-15*, 2011.
[165] Polcar, T.; Parreira, N.; Novák, R., Friction and wear behaviour of CrN coating at temperatures up to 500 C, *Surface and Coatings Technology*, 2007, vol. 201, no. 9, p. 5228-5235.
[166] Viáfara, C.; Sinatora, A., Unlubricated sliding friction and wear of steels: An evaluation of the mechanism responsible for the T1 wear regime transition, *Wear*, 2011, vol. 271, no. 9, p. 1689-1700.
[167] Polcar, T.; Vitu, T.; Cvrcek, L.; Vyskocil, J.; Cavaleiro, A., Effects of carbon content on the high temperature friction and wear of chromium carbonitride coatings, *Tribology International*, 2010, vol. 43, no. 7, p. 1228-1233.

[168] Spaltmann, D.; Löhr, M.; Binkowski, S.; Woydt, M., Einfluss der Topographie von DLC-Schichten auf deren Verhalten unter geschmierter Wälzbeanspruchung, *Tribologie und Schmierungstechnik*, 2004, vol. 51, no. 6, p. 18-26.
[169] Gammon, W.; Hoatson, G.; Holloway, B.; Vold, R.; Reilly, A., Bonding in hard and elastic amorphous carbon nitride films investigated using 15 N, 13 C, and 1 H NMR spectroscopy, *Physical Review B*, 2003, vol. 68, no. 19, p. 195401.
[170] Vaughn, G.D.; Frushour, B.G.; Dale, W.C., Scratch indentation, a simple adhesion test method for thin films on polymeric supports, *Journal of Adhesion Science and Technology*, 1994, vol. 8, no. 6, p. 635-650.
[171] Holmberg, K.; Ronkainen, H.; Laukkanen, A.; Wallin, K., Friction and wear of coated surfaces—scales, modelling and simulation of tribomechanisms, *Surface and Coatings Technology*, 2007, vol. 202, no. 4, p. 1034-1049.
[172] Huang, L.Y.; Zhao, J.W.; Xu, K.W.; Lu, J., A new method for evaluating the scratch resistance of diamond-like carbon films by the nano-scratch technique, *Diamond and Related Materials*, 2002, vol. 11, no. 7, p. 1454-1459.
[173] Randeniya, L.; Bendavid, A.; Martin, P.; Amin, M.S.; Preston, E., Molecular structure of SiO_x-incorporated diamond-like carbon films; evidence for phase segregation, *Diamond and Related Materials*, 2009, vol. 18, no. 9, p. 1167-1173.
[174] Yan, X.; Xu, T.; Chen, G.; Yang, S.; Liu, H., Study of structure, tribological properties and growth mechanism of DLC and nitrogen-doped DLC films deposited by electrochemical technique, *Applied Surface Science*, 2004, vol. 236, no. 1, p. 328-335.
[175] Li, H.; Xu, T.; Wang, C.; Chen, J.; Zhou, H.; Liu, H., Friction behaviors of hydrogenated diamond-like carbon film in different environment sliding against steel ball, *Applied Surface Science*, 2005, vol. 249, no. 1, p. 257-265.
[176] Li, H.; Xu, T.; Wang, C.; Chen, J.; Zhou, H.; Liu, H., Friction-induced physical and chemical interactions among diamond-like carbon film, steel ball and water and/or oxygen molecules, *Diamond and Related Materials*, 2006, vol. 15, no. 9, p. 1228-1234.
[177] Bhushan, B., Adhesion and stiction: mechanisms, measurement techniques, and methods for reduction, *Journal of Vacuum Science & Technology B: Microelectronics and Nanometer Structures*, 2003, vol. 21, no. 6, p. 2262-2296.
[178] Thundat, T.; Zheng, X.Y.; Chen, G.; Sharp, S.; Warmack, R.; Schowalter, L., Characterization of atomic force microscope tips by adhesion force measurements, *Applied Physics Letters*, 1993, vol. 63, no. 15, p. 2150-2152.
[179] Fuchs, H.; Bhushan, B., Applied Scanning Probe Methods II: Scanning Probe Microscopy Techniques, Springer-Verlag, 2006.
[180] Thundat, T.; Zheng, X.Y.; Chen, G.; Warmack, R., Role of relative humidity in atomic force microscopy imaging, *Surface Science*, 1993, vol. 294, no. 1, p. L939-L943.
[181] Liu, G.; Yan, G.; Zou, W.; Li, Z., Investigation of complexation of linear poly(N-vinyl-2-pyrrolidone) with poly(methacrylic acid-co-methyl methacrylate) gel, *E-Journal of Chemistry*, 2011, vol. 8, no. 1, p. S481-S487.
[182] Janarthanan, V.; Thyagarajan, G., Miscibility studies in blends of poly (N-vinyl pyrrolidone) and poly (methyl methacrylate) with epoxy resin: a comparison, *Polymer*, 1992, vol. 33, no. 17, p. 3593-3597.
[183] Giri, N.; Natarajan, R.; Gunasekaran, S.; Shreemathi, S., 13 C NMR and FTIR spectroscopic study of blend behavior of PVP and nano silver particles, *Archives of Applied Science Research*, 2011, vol. 3, no. 5, p. 624-630.
[184] Laot, C.M.; Marand, E.; Oyama, H.T., Spectroscopic characterization of molecular interdiffusion at a poly (vinyl pyrrolidone)/vinyl ester interface, *Polymer*, 1999, vol. 40, no. 5, p. 1095-1108.

[185] Tamulevičienė, A.; Meškinis, Š.; Kopustinskas, V.;Tamulevičius, S., Carrier gas and ion beam parameter effects on the structure and properties of aC:H/SiO_x films deposited employing closed drift ion beam source, *Nuclear Instruments and Methods in Physics Research Section B: Beam Interactions with Materials and Atoms*, 2012, vol. 282, p. 116-120.
[186] Ferrari, A.; Rodil, S.; Robertson, J., Interpretation of infrared and Raman spectra of amorphous carbon nitrides, *Physical Review B*, 2003, vol. 67, no. 15, p. 155306.
[187] Enomoto, K.; Hasebe, T.; Asakawa, R.; Kamijo, A.; Yoshimoto, Y.; Suzuki, T.; Takahashi, K.; Hotta, A., Controlling the drug release rate from biocompatible polymers with micro-patterned diamond-like carbon (DLC) coating, *Diamond and Related Materials*, 2010, vol. 19, no. 7, p. 806-813.